Analysing the electric field vector of air shower radio emission

Zur Erlangung des akademischen Grades eines
DOKTORS DER NATURWISSENSCHAFTEN
von der Fakultät für Physik
des Karlsruher Instituts für Technologie (KIT)

genehmigte
DISSERTATION

von Diplom-Physiker Daniel Huber
aus Karlsruhe (Baden)

Tag der mündlichen Prüfung: 23.05.2014
Referent: Prof. J. Blümer
Korreferent: Prof. U. Husemann
Betreuer: Dr. T. Huege

Analysing the Electric Field Vector of Air Shower Radio Emission

When entering the Atmosphere cosmic rays induce extensive air showers. For primary energies $\geq 10^{15}$ eV these consist of billions of particles, among them electrons and positrons which get deflected in the Earth's magnetic field, creating time-varying transverse currents. The air shower emits coherent electromagnetic radiation in the MHz frequency range which can be recorded by antenna arrays on ground. Nowadays the radio detection technique is evolving from prototype setups such as the **LO**FAR **P**rototyp**E** **S**tation (LOPES) to large-scale detector arrays like the **A**uger **E**ngineering **R**adio **A**rray (AERA). The detection techniques as well as the simulations improved considerably over the last decade. Nevertheless, the contribution of the vertical component to the total radio signal emitted by air showers was not studied experimentally so far. It is expected that the vertical component gets more and more important for horizontal air shower detection.
Within this work improved methods to analyse data recorded with LOPES 3D were developed. These methods are generally applicable for radio detection and thus the results obtained have direct impact on present and future experiments.
Most cosmic-ray radio experiments measure with only one or two horizontally aligned antennas at the same location. To study the benefits of additional measurements with vertically aligned antennas we have equipped LOPES with tripole antennas. LOPES 3D necessitated a new calibration which significantly improved the **detector understanding:**
We have done a detailed calibration of the new tripole antenna and developed a new frequency-dependent time calibration procedure. Furthermore, we have demonstrated that LOPES 3D is sensitive enough to detect radio emission from the galactic plane. Using measurements with the new antenna type it is possible to reconstruct the electric field vector. Thus we made several **improvements of the analysis procedure for LOPES:**
We have implemented the correct treatment of the antenna gain, including phases. Thus, for the first time in LOPES the electric field vector can be measured and reconstructed. Now, analyses using the orientation of the electric field vector have become feasible, e. g. by using the complete electric field vector for determining a lateral distribution function. We have also developed a vectorial cross-correlation beamforming which can be applied to the complete electric field vector. A well-defined standard criterion to select reconstructed events has been established.
The measurements with vertically aligned antennas are unique which leads to an **increase of understanding the radio detection technique:**
We have developed several approaches exploiting the measurements with vertically aligned antennas. Unfortunately, these measurements do not have the expected benefits. We investigated that this is mainly due to the high background level at LOPES 3D. However, the experience gained within this work impacts present and also future radio experiments.

Analyse des elektrischen Feldvektors der Radioemission aus Luftschauern

Hochenergetische kosmische Teilchen lösen beim Eintritt in die Atmosphäre Luftschauer aus. Aufgrund der Ablenkung der geladenen Teilchen im Erdmagnetfeld wird eine im MHz-Frequenzbereich kohärente elektromagnetische Strahlung emittiert. Diese wird von Antennenfeldern zur Analyse von Luftschauern gemessen. Derzeit entwickelt sich die Radiomethode von Prototyp-Experimenten wie LOPES hin zu großskaligen Experimenten wie dem **A**uger **E**ngineering **R**adio **A**rray (AERA). In diesem Rahmen werden Detektionstechniken wie auch Simulationen mit großem Interesse weiterentwickelt. Dessen ungeachtet ist der Beitrag der vertikalen Komponente des elektrischen Feldes zum Luftschauer-Radiosignal experimentell noch nicht hinreichend genau bestimmt.
LOPES wurde mit Tripol-Antennen ausgestattet, um den zusätzlichen Informationsgehalt und Nutzen von Messungen mit vertikalen Antennen zu untersuchen. Im Rahmen der vorliegenden Arbeit wurden Detektionsmethoden für LOPES 3D entwickelt. Diese Methoden sind allgemein auf die Radiomessung von kosmischer Strahlung anwendbar. Zudem war eine Neukalibrierung von LOPES 3D erforderlich, was zu einer erheblichen **Verbesserung des Detektorverständnisses** führte:
Es wurde eine detaillierte Kalibrierung der Tripol-Antennen vorgenommen und ein frequenzabhängiges Zeitkalibrationsverfahren entwickelt. Desweiteren konnte nachgewiesen werden, dass LOPES 3D sensitiv genug ist, um die Radioemission aus der Galaktischen Ebene zu detektieren. Durch Messungen mit mindestens zwei der drei Arme einer Tripol-Antennen kann der elektrische Feldvektor rekonstruiert werden. Dies ermöglichte signifikante **Verbesserungen der LOPES 3D Datenanalyse**:
Die korrekte Anwendung der Antennencharakteristik inklusive Phasen wurde implementiert. Damit konnte erstmals der elektrische Feldvektor aus mit LOPES aufgezeichneten Daten rekonstruiert werden. Dies ermöglicht Analysen basierend auf dem kompletten elektrischen Feldvektor, beispielsweise die Rekonstruktion einer Radio-Lateral-verteilung. Es wurde ein Kreuzkorrelationsverfahren entwickelt, das auf komplette elektrische Feldvektoren angewendet werden kann. Außerdem wurde ein definiertes Kriterium entwickelt, um rekonstruierte Radio-Ereignisse automatisiert zu selektieren. Mit LOPES 3D wurde zum ersten Mal mit zusätzlichen vertikalen Antennen gemessen, was zu einer **Verbesserung des Verständnisses der Radiodetektionstechik** beitrug:
Es wurden verschiedene Methoden entwickelt, um den optimalen Nutzen aus der zusätzlichen Messung mit vertikalen Antennen zu ziehen. Allerdings wurden die Erwartungen nicht erfüllt, was auf den sehr hohen Radio-Untergrund bei LOPES zurückzuführen ist. In einer detaillierten Studie konnte gezeigt werden, dass der Untergrund in der vertikalen Komponente stark mit dem Zenitwinkel zunimmt und somit die Rekonstruktionsqualität entscheidend beeinträchtigt. Die gewonnenen Erkenntnisse werden allerdings aktuelle und zukünftige Radioexperimente maßgeblich beeinflussen.

Contents

CHAPTER 1

Introduction

Cosmic rays have been studied for more than 100 years. Although the detection techniques developed very fast and promisingly, the key questions are still not answered satisfactorily. The process of acceleration, the origin and propagation of cosmic rays through outer space are not yet completely understood. To answer these questions, the cosmic rays reaching Earth have to be studied with high precision at the highest energies (Haungs et al., 2003). This requires ground-based observatories that cover huge areas since the flux of cosmic rays at these energies is too low to measure them directly in space. Therefore extensive air showers (Auger et al., 1939) that are caused by high energy cosmic rays are observed. One important parameter when observing cosmic rays indirectly is the atmospheric depth at which an air shower contains the maximum number of charged particles, X_{max}, which can be used to statistically analyse the composition of primary cosmic rays. So far fluorescence telescopes reach the best X_{max} resolution ($\approx 20\frac{\mathrm{g}}{\mathrm{cm}^2}$), but the uptime is limited to clear and moonless nights which results in a net uptime of $\leq 15\%$ (Abraham et al., 2010). Radio detection can provide a very high uptime ($\geq 95\%$) (Haungs, 2009) and recent simulation studies have shown that indeed the radio signal has an intrinsic X_{max} resolution of better than $30\frac{\mathrm{g}}{\mathrm{cm}^2}$ (Schröder, 2011) which is also experimentally confirmed (Buitink, S. et al., 2013). Therefore the interest in developing the radio detection technique is large and several approaches have been made to advance and exploit this technique to the optimum. Earlier approaches on the radio detection of cosmic rays as done in the 1960s and 1970s (Jelley et al., 1965) suffered from the lack of fast digital electronics available at that time. These first efforts were reviewed by Allan in 1971 (Allan, 1971). Only with the development of digital electronics air shower radio measurements with competitive precision have become feasible.

The radio detection technique is preferably used in hybrid mode with a particle detector air shower array. Nevertheless, stand-alone radio experiments are in principle possible. To gain maximum information on the radio signal produced by an extensive air shower, it is necessary to record and reconstruct the complete electric field vector. This contributes to improving the understanding of the radio emission mechanism during the present development and optimization phase of this detection technique.
The aim of this work was to study the benefits of 3D measurements in radio. In 2010 the LOPES experiment at KIT was reconfigured and equipped with tripole antennas. Before that it was only possible to measure with one or two antennas at the same place. When measuring with only one antenna a simplification of the antenna gain has to be applied to reconstruct the electric field. When measuring with two antennas at the same place it is in principle possible to reconstruct the complete electric field vector. However, so far this was not done with LOPES. Thus, with former setups of LOPES a reconstruction of the complete electric field vector was not available. Consequently all studies based on electric field vectors were not feasible. LOPES is located at a radio loud area. Thus, advanced analysis methods are needed in order to be able to detect air shower radio emission. In LOPES the cross-correlation beamforming (CC-beamforming) was used to significantly improve the signal-to-noise-ratio of measured signals. The CC-beamforming is sensitive to correlations in amplitude and phase of the measured signals. This beamforming was done separately on the data measured with east-west aligned antennas and north-south aligned antennas.
Within this thesis we improved the application of the antenna gain from an approximation to the correct application. With this a complete reconstruction of the electric field vector is available, for the first time in LOPES. Thus, studies based on the orientation of the electric field vector have become feasible. With the complete reconstructed electric field vector it was possible to enhance the CC-beamforming, which can now be done on the complete electric field vector. With this, the CC-beamforming is also sensitive to a correlation in the orientation of the measured electric field vector. With three antennas at the same place the electric field vector can be reconstructed three times, since in principle only two antennas at the same place are needed in order to reconstruct the electric field vector. Thus, we developed several methods to take advantage of this redundancy.
This thesis is structured in the following way:
An introduction to cosmic rays with a focus on radio detection of air showers is given in chapter 2. Then the experimental setup and the calibration procedure of LOPES 3D are described in chapter 3. After this the preselection of events for the radio reconstruction and consistency checks on the radio data are shown in chapter 4. In chapter 5 the correct antenna gain application is described and it is shown how we reconstruct the electric field vector from measurements. This

electric field vector can be used in a vectorial beamforming procedure which is discussed in chapter 6. In chapter 7 we conduct an analysis based on the orientation of the electric field vector with focus on the predictions from two emission models. Then the benefits of additional measurements with vertically aligned antennas and methods to make use of this measurements are discussed in chapter 8.

CHAPTER 2

Cosmic Rays

2.1. History

Until 1912 it was assumed that with rising altitude the ionisation rate of the atmosphere will decrease, since the radiation was suspected to come from the Earth itself. With a balloon flight, Victor Hess detected in 1912 that at above an altitude of $1000\,\mathrm{m}$ the ionisation rate of the atmosphere rises with increasing altitude (Hess, 1912; Fick and Hoffmann, 2014). From this he concluded that this ionising radiation has to come at least partly from outside the atmosphere. He confirmed his detection with several more flights. These cosmic rays have been the only possibility to study high energy particles for a long time. Even today, man-made particle accelerators like the Large Hadron Collider (LHC) (Evans and Bryant, 2008) cannot reach the energy of the highest energy cosmic rays. Ultra high energy cosmic rays (energies above $10^{18}\,\mathrm{eV}$) are the most energetic particles known to mankind. If the predicted magnetic field strengths from the galactic and extragalactic models are correct, they can even point back to their sources. Thus, it is of high interest to detect these particles. Other possibilities to identify sources of cosmic rays are neutrinos or gamma rays that are not influenced by galactic or extragalactic magnetic fields.

2.2. Origin of Cosmic Rays

The dominant source of particles with energies lower than 10^9 eV is the sun. The solar wind mainly consists of electrons, protons and helium nuclei. During a solar flare the flux and the energy of these particles can temporarily increase. However, the sun is not only a source of low energy cosmic rays, with its magnetic field it can also shield the Earth. Particles have to cross the heliosphere with magnetic fields that can reach values up to 10 nT and which are anti correlated with the solar activity (Stanev, 2004).
The acceleration of high energy cosmic rays with energies at least up to 10^{16} eV most probably takes place in supernovae shock waves. This acceleration mechanism takes place in magnetised plasma clouds and was postulated in 1949 by Enrico Fermi (Fermi, 1949). Possible accelerators are supernova remnants of types[1] II, Ib, and Ic. Indications for supernovae being sources are:

- The observed rate of supernovae can explain the cosmic ray energy flux assuming shock-wave acceleration.
- The elementary composition of supernovae matches the composition of cosmic rays.
- The assumption still holds for a realistic acceleration efficiency.
- The π^0-decay gamma signal is observed (Ackermann et al., 2013).

At even higher energies , E$\geq 10^{18}$ eV, the magnetic field of the milky way is too weak to keep particles in our galaxy. Since no sources with these energies were found in our galaxy, the milky way, only extragalactic sources can be considered as the origin of cosmic rays with such high energies. Possible sources are supermassive black holes, active galactic nuclei (AGNs), gamma ray bursts (GRBs) and pulsars. The acceleration by these suggested sources is no entirely convincing scenario.

2.3. Cosmic Ray Spectrum

The spectrum of cosmic rays, cf. figure 2.1, can be described by a falling power law up to energies of $\approx 10^{15}$ eV with a spectral index $\gamma \approx 2.7$. At $5 \cdot 10^{15}$ eV the

[1] The supernova remnants are classified according to their spectrum. For supernovae type II hydrogen can be observed in the early spectrum. For supernovae type Ib Ic the early spectrum does shown evidence for hydrogen and their spectrum generally does not contain silicon.

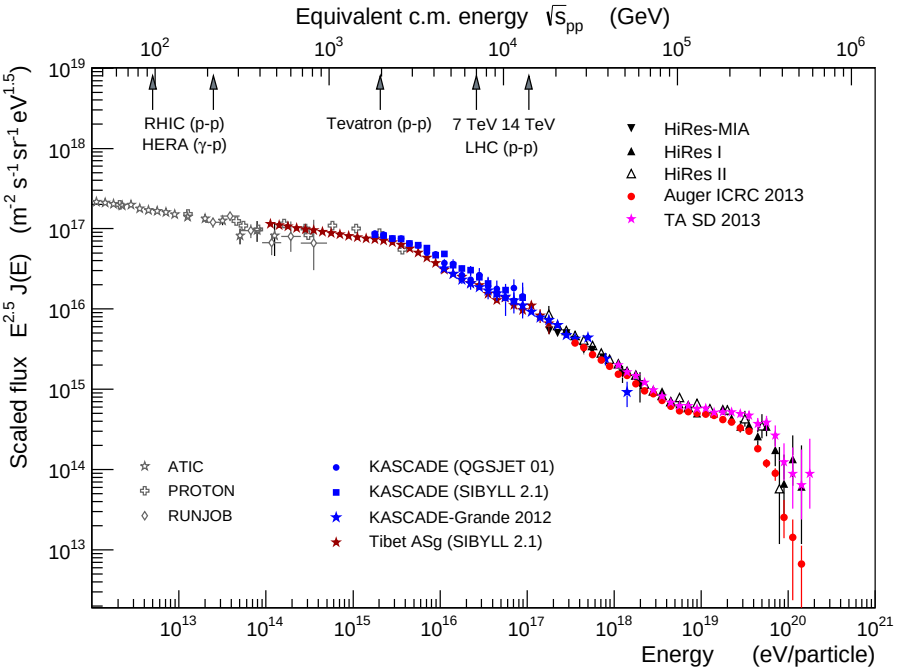

Figure 2.1.: Updated measured spectrum (Engel et al., 2011) of the cosmic rays. To better see the features the spectrum is scaled with $E^{2.5}$.

spectral index changes to $\gamma \approx 3$. This feature is called the knee (Antoni et al., 2003). At energies larger than 10^{18} eV the spectral index changes back to ≈ 2.7. This feature is called the ankle. The knee originates from the end of the spectrum for light nuclei, i.e. protons or helium nuclei, thus the acceleration mechanism can be assumed to be charge and/or mass dependent. In the recent past, a second knee of heavy particles could be observed at an energy of $10^{16.9}$ eV by KASCADE-Grande (Apel et al., 2011b). This heavy knee is weaker, but in agreement with a drop in the iron flux. This can be explained by assuming a charge-dependent acceleration process.

The ankle might originate from the energy loss of protons by undergoing pair production. The transition from a galactic to an extragalactic origin of cosmic rays is expected in the energy range between 10^{17} and 10^{19} eV. Recent measurements of the KASCADE-Grande experiment have shown an ankle-like feature in the spectrum of light cosmic rays already at $\approx 10^{17.08\pm0.08}$ eV (Apel et al., 2013) which could be interpreted as an onset of a new extragalactic component on the galactic. At energies above $5 \cdot 10^{19}$ eV the spectrum cuts off. Explanations for this could be that the sources run out of power, fission of iron nuclei which would result in a measured pure light spectrum, or the GZK cut-off. Greisen, Zatsepin and Kuzmin postulated in 1966 that at this energy a proton p can interact with a

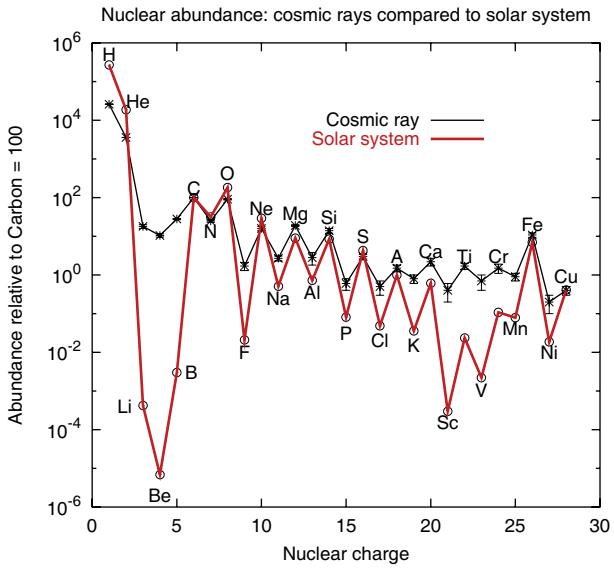

Figure 2.2.: Relative nuclear abundances in the solar system and in the cosmic rays. (Gaisser and Stanev, 2006).

photon γ_{CMB} of the cosmic microwave background and form a π^0 meson via the Δ^+-resonance according to:

$$p + \gamma_{CMB} \rightarrow \Delta^+ \rightarrow p + \pi^0 \tag{2.1}$$

The mean free path of such an energetic proton is of the order of $50\,\text{Mpc}$. Thus only protons from sources within $\approx 50\,\text{Mpc}$, i.e. the close extragalactic environment, can reach the Earth at these high energies.

2.4. Cosmic Ray Mass Spectrum

The mass spectrum of cosmic rays is only known exactly for low energies ($\leq 10^{15}\,\text{eV}$), see figure 2.2, since at these energies the flux is high enough to measure cosmic rays directly with small detector volumes before they start to develop an air shower. In this energy range, most cosmic rays are atomic nuclei, only 2% are gamma rays and electrons. For energies $\leq 10^{15}\,\text{eV}$ the elementary composition of cosmic rays nearly matches the one of the solar system. The excess of lithium, beryllium and boron, as well as the abundance of elements below iron can be explained by spallation processes during the transport through the galactic magnetic field and the interstellar medium.

For higher energy cosmic rays no direct measurement is possible due to the low flux. The only possibility to measure these cosmic rays is to measure secondary particles or corresponding electromagnetic radiation that are created during an air shower and reach the Earth. From air shower parameters like height of the first interaction, curvature of the shower front, atmospheric depth of the maximum particle number or distributions of different secondary particle types on the ground, the primary particle parameters can be inferred by comparing the measured quantities with Monte Carlo simulations. The results of the simulations strongly depend on the interaction model applied, which makes the exact reconstruction of the primary particle very challenging (Apel W. D. et al. (KASCADE Collaboration), 2007). With this method the composition of the cosmic rays can only be accessed on a statistical basis.

2.5. Extensive Air Showers

Air showers start when high energy cosmic rays interact with nuclei of molecules from the Earth's atmosphere. The first interactions are hadronic interactions with atomic nuclei of atmospheric molecules. A particle cascade mainly consisting of photons, electrons and positrons evolves. These electrons, positrons and photons form the electromagnetic component of the shower. Another component is the muonic component. The muons mainly originate from decays of charged mesons in the shower. Because of their low interaction cross-section muons penetrate deeper in the atmosphere than the electromagnetic component. An overview of the different shower components is shown in figure 2.3. The shower age[2] is one estimator for the composition of the primary cosmic rays (Giller et al., 2005) and can be estimated by comparing the electromagnetic with the muonic component. Hadrons constitute the smallest part of an air shower in numbers. They are generated during the early stage of an air shower and are very important for the shower development since they carry very high momenta close to the shower axis and thus can start several cascades and thus, constantly supply the air shower. With this, the hadronic cascade feeds the other components of the air shower.

[2]The age parameter describes the shape of the particle distribution and is related to the status of the longitudinal development and thus to the mass of the primary particle.

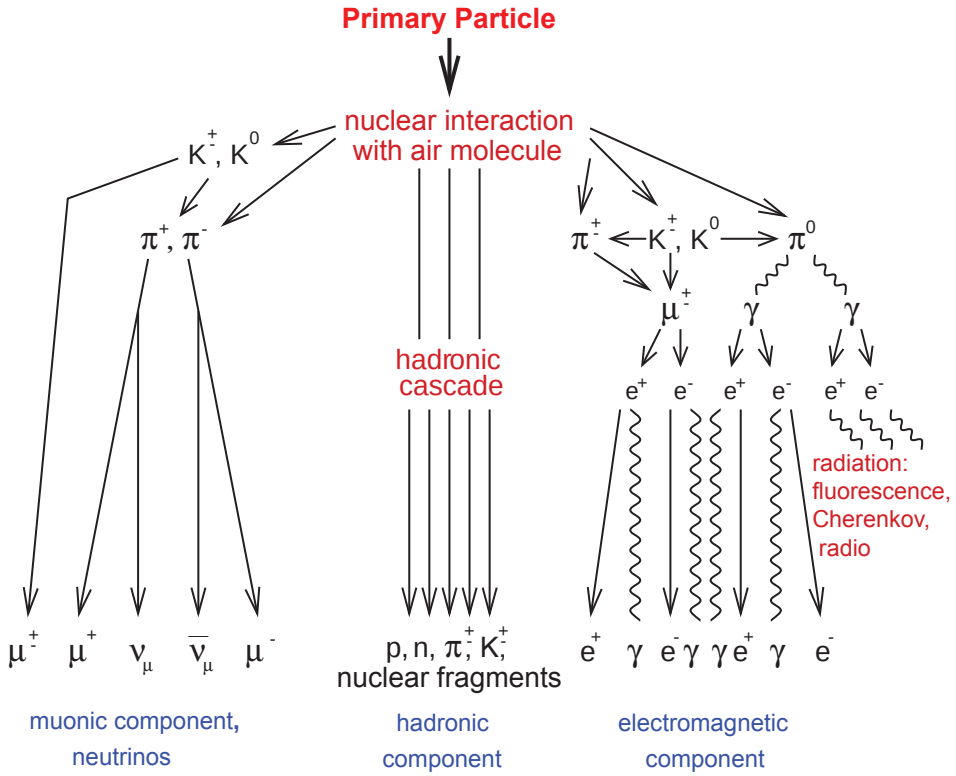

Figure 2.3.: Scheme of the different air shower components like the muonic (left hand side) the hadronic (center) and the electromagnetic (right hand side) component (Haungs et al., 2003).

2.6. Detection Techniques for Air Showers

For the detection of cosmic-ray-induced air showers many detection techniques are available. The best results are obtained by combining several techniques complementary to each other in their shower observation. This way, the disadvantages of single techniques can be compensated and the advantages can be exploited to maximum extent. In the case of the Pierre Auger Observatory (Abraham J. et al., 2004) a surface air shower detector, realized using water Cherenkov tanks, operates in hybrid mode with four fluorescence telescopes. An overview sketch of the most common air shower detection techniques is shown in figure 2.4. In the following, several detection techniques will be discussed regarding their advantages and their draw-backs.

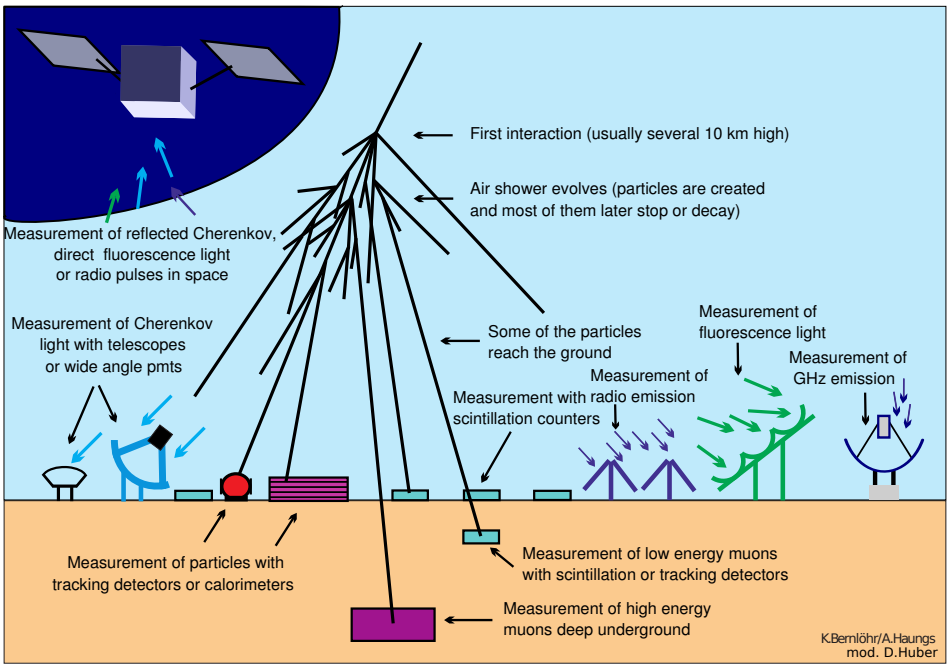

Figure 2.4.: Overview sketch of the different air shower detection techniques (Haungs et al., 2003).

2.6.1. Particle Detectors

The detection of charged particles of an air shower such as the electrons, positrons and muons at ground level is the oldest detection technique for air showers (Auger et al., 1939). Possible detectors are water Cherenkov tanks, like used at the Pierre Auger Observatory (Abraham J. et al., 2010) or the Haverah Park experiment (Lawrence et al., 1991) scintillators, like used for example in KASCADE-Grande (Apel et al., 2010) or AGASA (Takeda et al., 1998), proportional counters like used in GRAPES (Tanaka et al., 2012) calorimeters or tracking gas detectors like used in KASCADE. With these ground based detectors a footprint of the shower can be recorded. From this, the direction of the primary particle is reconstructed by triangulation. Furthermore, the energy of the primary particle can be estimated from the lateral distribution of the secondary particles. To analyse the data taken with these particle detectors interaction models are used which have to be extrapolated beyond the energy range accessible with current particle accelerators.

2.6.2. Imaging Atmospheric Cherenkov Telescopes

Another possibility for measuring air showers are so-called imaging atmospheric Cherenkov telescopes. These telescopes consist of large spherical mirrors and photomultiplier cameras. They are used to detect the Cherenkov radiation generated by high energetic gamma rays. They have a small field of view and therefore have to point in the direction of the air shower. The threshold for the detection technique is $\approx 10^{10}$ eV (Aharonian and Akerlof, 1997). These telescopes can only work during clear nights with very little moonlight. The main advantage of the detection of gamma rays is that these particles are not charged and therefore not influenced by galactic magnetic fields which means that they point back to their sources. This makes this technique ideal for the search for sources with energies up to TeV. Experiments using this technique are for example HESS (HESS, 2014) or MAGIC (MAGIC, 2014).

2.6.3. Non-Imaging-Cherenkov Detectors

The Cherenkov effect can also be used in so-called non-imaging-Cherenkov detectors. Arrays of these detectors work in principle like the particle detector arrays, but instead of recording the footprint of the particle cascade they record the Cherenkov emission on the ground. A detector station typically consists of one or more photomultipliers looking up in the night sky. Like the Cherenkov telescopes these detectors can only measure during clear nights with very little moonlight. Examples for experiments using this technique are Tunka 133 (Gress et al., 1999) and Yakutsk (Knurenko et al., 2008).

2.6.4. Fluorescence Detectors

The fluorescence detectors are built in a similar way as the Cherenkov-telescopes, but they have a larger field of view and therefore cover a larger area. They also consist of large spherical mirrors and photomultiplier cameras. When a relativistic particle of an air shower interacts with a nitrogen molecule of the atmosphere, this molecule gets into an excited state. When going back to the ground state these excited molecules isotropically emit ultra-violet light. This light can be measured by large telescopes. With this method the air shower is observed from the side. Thus, the air shower development can be analysed very well with this technique. Like the Cherenkov telescopes the fluorescence detectors work only during clear nights with very little moonlight. The threshold for this detection technique is 10^{17} eV (Haungs et al., 2003). Experiments using this technique are for example the Pierre Auger Observatory and Fly's Eye (HiRes) (Sokolsky, 2011).

2.6.5. Radio Detection

Another possibility to observe air showers on the ground is the detection of the radio signal emitted during the evolution of an air shower. The radio detection has several advantages: The detectors are simple antennas that can be easily produced in large amounts in short time and at low costs. This detection method has an uptime of nearly 100%. The radio technique is sensitive to the shower development (Apel et al., 2012b) and not depending on weather conditions, except for thunderstorms and high atmospheric electric field strengths (Apel et al., 2011a), see also appendix A. This method is very sensitive to inclined showers (Holt, 2013). The main disadvantages of this technique are the high background in industrialized areas and since this is a relatively new detection technique most of the analysis methods still have to be developed and improved. The exact contributions of emission mechanisms to the radio signal are still under investigation which is a crucial point to reconstruct primary particle characteristics from the measured signal. With increasing knowledge on the exact emission mechanism the reconstruction accuracy will gradually improve. Based on radio data the arrival direction, the energy and the elemental composition of the primary cosmic rays can be reconstructed (Apel et al., submitted 2014a).

2.7. Properties of Air Shower Radio Emission

During the air shower development charged particles, mostly electrons and positrons, get deflected in the Earth's magnetic field. For wavelengths smaller than the thickness of the particle shower front, a few meter, the radio emission is coherent ($\widehat{=}$ radio frequencies $\lesssim 100\,\mathrm{MHz}$). Thus, at these frequencies the radio pulse generated by an air shower is easier to detect. This is the main reason why most of the radio experiments operate below $100\,\mathrm{MHz}$. Other reasons are man-made noise, i.e broadcasting stations which emit at frequencies between 87 to $100\,\mathrm{MHz}$ and the high costs of fast electronics, at least at the time LOPES was built. At frequencies below $30\,\mathrm{MHz}$ the atmospheric noise is too high. The emitted pulse can be very short ($\approx 1\,\mathrm{ns}$) depending on geometry but the limited band width leads to a minimum radio pulse length in the order of $10\,\mathrm{ns}$, also depending on shower geometry. In the coherent frequency range the radio pulse amplitude scales with the number of charged particles in the air shower and thus with the energy of the primary particle (Huege et al., 2012). The pulse amplitude also depends on the geomagnetic angle[3] and the distance between observer position

[3]The geomagnetic angle is the angle between air shower axis and Earth's magnetic field.

and shower axis. These dependencies have been studied and confirmed by several analyses (Ardouin et al., 2009). However, a detailed quantification requires good understanding of the emission mechanisms that contribute to the radio pulse.

2.7.1. Emission Mechanisms

The emission of electromagnetic radiation in the MHz regime is dominantly caused by two processes, first, the induced transverse current. The air shower traverses the Earth's magnetic field which, in combination with interactions in the atmosphere, leads to a deflection of the charged particles. A time dependent transverse current is created.
The second process is the charge excess: When travelling through the atmosphere the amount of particles of an air shower changes differently for electrons and positrons with time due to ionization of the atmosphere, pair production and absorption.
Discussing the mechanisms which contribute to a radio pulse goes along with discussing simulations of the radio emission using different approaches. There are computer codes available that differ significantly in their approach. Some codes use parametrized showers and do an analytical calculation, others use a Monte Carlo method to simulate the radio pulse. Nearly all codes deliver results that agree with each other in their qualitative predictions see reference (Huege, 2012) for more details. This is great improvement since in 2011 they still differed by an order of magnitude or more. A Monte Carlo based approach is followed with the CoREAS code. In this simulation the radio pulse is calculated in the time domain using an end-point formalism (Ludwig and Huege, 2011; James et al., 2010) and summing up the radiation contributions from single particles. The particle distributions are simulated by the air shower particle simulation code CORSIKA (Heck et al., 1998). Today CoREAS is one of the most advanced code available with no free physical parameters. A result of CorEAS simulation is shown in figure 2.5. An analytical approach, summing up the emission from dominant mechanisms, is followed in the MGMR (Macroscopic model of GeoMagnetic Radiation) (Scholten et al., 2008) model. The agreement of MGMR with CoREAS within a factor of $2-3$ is a hint that superposing different mechanisms is a fair approximation. In spite of small differences between the models, one thing is common: The radio emission has a dominant geomagnetic origin. This was already observed by the historical measurements like Haverah Park (Lawrence et al., 1991) and is confirmed by several current radio experiments like CODALEMA (Ardouin et al., 2009), AERA (Aab et al., 2014) and LOPES (Apel et al., 2012a). A selection of experiments measuring the radio emission from cosmic rays is given in section 2.7.2. In the following, different mechanisms that contribute to the radio signal

are listed. However, the different mechanisms have mutual interactions, therefore it is impossible to disentangle them completely.

Emission Originating from Geomagnetic Deflection

Transverse Currents The charged particles of an air shower, mainly electrons and positrons, get deflected in the Earth's magnetic field due to the Lorentz force and interactions with nuclei in the atmosphere. In the moving shower plane[4] electrons get deflected in the opposite direction of positrons which induces transverse currents, see also figure 2.6. These currents lead to radio emission. This emission is polarized perpendicular to the shower axis and the geomagnetic field. Due to the dependence of this emission on the Earth's magnetic field ($\vec{B}$) and the Lorentz force it can be approximated by a $\vec{v}\times\vec{B}$-dependence, where $\vec{v}$ is the velocity of the primary particle. This is assumed to be the main emission mechanism in extensive air showers (Huege et al., 2010; Kahn and Lerche, 1966).

Varying Dipole The separation of electrons and positrons leads to a dipole like structure which moves along the shower axis. This dipole varies in strength with time which leads to radio emission. After being passed by the shower, the atmosphere is charged due to ionisation processes which gives an additional but weaker emission (Werner and Scholten, 2008; Scholten et al., 2010).

Geosynchrotron Emission Because of their deflection, the electrons and positrons of an air shower are travelling on curved tracks. Thus, they emit synchrotron-like radiation in the radio frequency band. This emission is called geosynchrotron emission (Huege and Falcke, 2003). At the moment the strength of the contribution of the geosynchrotron emission to the total signal is unclear but probably very small at low frequencies. Nevertheless geosynchrotron emission might matter at GHz frequencies (Huege and James, 2013).

Mechanisms Originating from Time Varying Charge Excess

Askaryan Effect (Varying Net Charge Excess) During the air shower evolution electrons and positrons are generated in different amount. Due to matter antimatter annihilation and ionization processes there is a predominance of electrons. This charge excess varies with time as the amount of particles in the air shower changes. This leads to radio emission which is radially oriented around the shower axis (Huege et al., 2010; Scholten et al., 2008; Askaryan, 1962).

[4]The shower plane is the plane perpendicular to the shower axis.

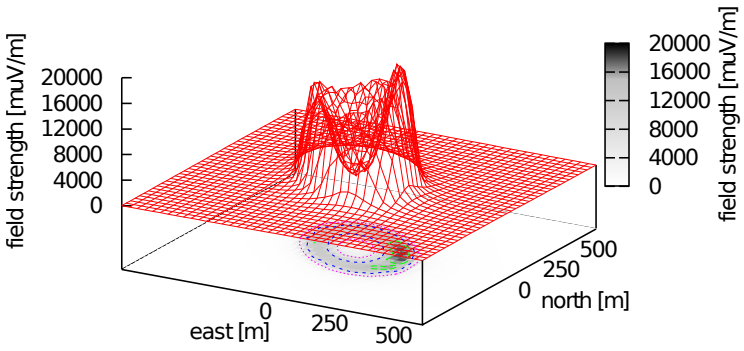

(a) 3D view of the absolute field strength.

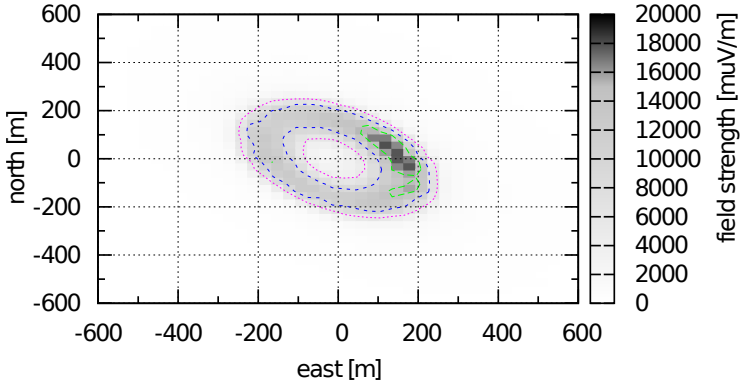

(b) Top view of the absolute field strength from a simulated air shower. The Cherenkov-ring-like structure can be seen.

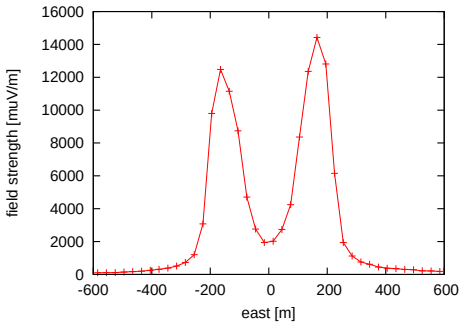

(c) Lateral distribution of the absolute field strength at $0\,\mathrm{m}$ north.

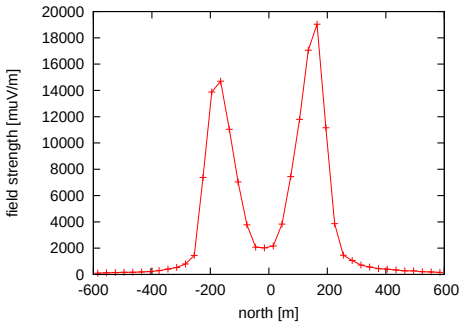

(d) Lateral distribution of the absolute field strength at $0\,\mathrm{m}$ east.

Figure 2.5.: Absolute field strength (unlimited bandwidth) at ground level of an air shower simulated with COREAS (Huege, T. and Ludwig, M. and James, C.W., 2013) for a proton primary arriving with an azimuthal angle of $50°$, a zenith angle of $45°$ and an energy of $1 \times 10^{18}\,\mathrm{eV}$

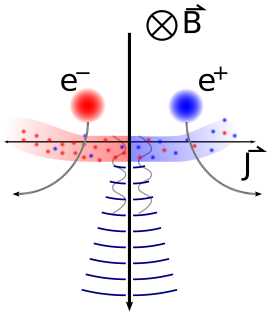

(a) Scheme of the emission process due to time dependent current density $\vec{j}$ caused by the deflection of electrons and positrons in the Earth's magnetic field $\vec{B}$.

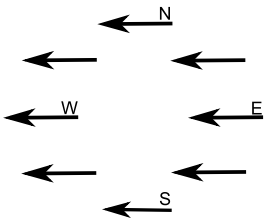

(b) Orientation of the electric field vectors for pure geomagnetic emission.

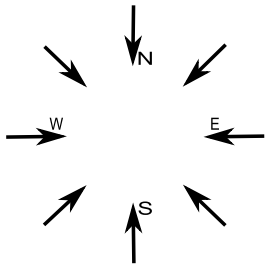

(c) Radial orientation of the electric field vectors as it is the case for pure net charge variation.

Figure 2.6.: Sketches of radio emission processes and polarization patterns in the shower plane.

Mechanisms Originating from the Refractive Index of Air

Cherenkov Emission Since the refractive index of air is slightly larger than unity, $n > 1$, and most relativistic air shower particles move with superluminal speed $v \geq \frac{c}{n}$, Cherenkov emission occurs. This Cherenkov emission is often confused with the Askaryan effect because they are both dominant in dense media. However, the Askaryan effect would also lead to emission in media with a refractive index of unity if there is a time varying charge, whereas Cherenkov emission requires $n > 1$ (Askaryan, 1965). Nevertheless this effect is not important for air showers but showers in dense media.

Cherenkov-Like Time Compression The Cherenkov-like time compression is not an emission mechanism, but a compression effect changing the coherence conditions and thus the characteristics of the emission.The particle shower front travels with a velocity larger than the speed of light in the atmosphere. The emitted electromagnetic radiation travels with the speed of light in the atmosphere. Thus radio pulses emitted at different air shower stages can arrive on the ground at the same time and superimpose. This is of course depending on frequency and on the shower geometry and leads to radio Cherenkov rings or ellipses on ground, cf. figure 2.5.

Atmospheric Electric Fields

Atmospheric electric fields can accelerate and decelerate the charged particles of an air shower which also causes radio emission. During extreme weather conditions, like thunderstorms, the atmospheric electric fields can reach values up to $E_{\mathrm{atm}} = 10000\,\mathrm{V/m}$. This causes a very high acceleration and deceleration of the charged particles which then leads to a radio emission even stronger than the geomagnetic emission, see reference (Buitink S. et al., 2007) and also appendix A, where the influence of cosmic rays on lightning initiation is discussed and the influence of strong electric fields on the radio signal is studied. So far the data taken during thunderstorms cannot be used to properly reconstruct air shower parameters. It was found that strong atmospheric electric fields that point in the direction of the incoming air shower have an influence on the Askaryan emission, whereas atmospheric electric fields that are oriented perpendicular to the arrival direction of the shower have an influence on the transverse currents (Gelb, 2012). However, there are no significant effects during fair or rainy weather ($\geq 95\%$ of the time).

2.7.2. Experiments for Measuring the Radio Emission from Air Showers

The radio detection of cosmic ray induced air showers was revived a decade ago. This went along with improvements of powerful digital signal processing. Since then several experiments to detect radio emission have been deployed and operated. In the following those recent experiments are introduced briefly.

AERA The Auger Engineering Radio Array (AERA)(Fuchs, 2012a) is an extension to the surface detectors and the fluorescence detectors of the Pierre Auger Observatory in Mendoza, Argentina. AERA currently consists of 124 antenna stations on an area of $6\,\mathrm{km}^2$ deployed with east-west and north-south aligned antennas. These antennas are taking data in the frequency range from 30 to $80\,\mathrm{MHz}$. AERA is externally and self-triggered and measures the radio emission of cosmic ray induced air showers at energies $E \geq 10^{17}\,\mathrm{eV}$. By polarization measurements the contribution of the charge excess to the radio signal measured with AERA could be quantified to 14% on average (Abreu et al., 2012).

ANITA ANITA stands for Antarctic Impulsive Transient Antenna (Nichol, 2011) and is a balloon borne radio interferometer, built to detect ultra high energy neutrinos. These neutrinos cause air showers that generate radio emission in the ice according to the Askaryan effect. ANITA uses horn antennas that measure radio pulses in the vertical and horizontal polarization. The balloon typically flies

approximately 37 km above the Antarctic ice. ANITA claims to have detected several radio pulses of air showers with primary energies $E \geq 10^{19}$ eV (Grashorn, 2012). This is the first broadband measurement of cosmic ray radio emission in the frequency range of 300 to 1000 MHz.

CODALEMA CODALEMA stands for COsmic ray Detection Array with Logarithmic ElectroMagnetic Antennas (Ravel, O. et. al, 2012). It is located at the Nançay radio observatory in France. Along with LOPES, CODALEMA was the first experiment for digital radio air shower measurements. CODALEMA is triggered by a relatively simple scintillator array and measures in the frequency range from 24 to 82 MHz. The main advantage of CODALEMA is the radio quiet environment. With CODALEMA, the charge excess was shown to contribute to air shower radio emission as a second order effect (Marin and et al., 2011). Like LOPES, CODALEMA was reconfigured several times.

LOFAR LOFAR stands for LOw Frequency ARray (Horneffer et al., 2010). It is a digital radio interferometer which is mainly built in the Netherlands for radio astronomy. It has a diameter of 350 km and operates in the frequency range from 20 to 80 MHz for the low frequency antennas and 110 to 240 MHz for the high frequency antennas. In total LOFAR consists of 77 stations. Each of these stations consists of 100 low and 100 densely packed high frequency antennas. The core of LOFAR is able to measure also radio emission from cosmic rays triggered by the particle detector array LORA (LOfar Radboud Air shower array) (Thoudam et al., 2011), built from former KASCADE scintillators. This is a particle detector array that triggers the core antenna array of LOFAR. In total there are up to 400 antennas available which gives the opportunity to study the lateral distribution function of air showers with by far the highest precision.

LOPES LOPES stands for LOfar PrototypE Station and was one of the first digital radio arrays to detect air shower radio emission and gave the proof of principle for cosmic ray detection via digital radio interferometry (Falcke et al., 2005). It was co-located with the particle detector array KASCADE-Grande at KIT which provided the external trigger and high quality air shower data. This is one reason for the success of LOPES. The prototype station evolved to an independent experiment, playing a leading role in the development of the radio detection technique. In the last setup LOPES consisted of 10 tripole antennas (Apel et al., 2012a) probing the benefits of additional direct measurements with vertically aligned antennas. With these, LOPES once more fullfilled its pioneering role in the development of the radio technique. The analysis of the data taken with the last setup is the content of this work.

TREND TREND stands for TIANSHAN Radio Experiment for Neutrino Detection (Martineau-Huynh et al., 2012). The experiment is located at the site of the 21 cm array radio telescope in XinJiang, China. The first prototype antennas for this experiment have been used to detect cosmic ray radio emission. The main science goal however, is to detect horizontal air showers induced by tau neutrinos interacting in the mountains surrounding the array.

Tunka-Rex Tunka-Rex is the Radio extension of the Tunka Cherenkov array (Berezhnev et al., 2012) located at the Tunka valley in Siberia. It consists of 25 antenna stations each equipped with two Short Aperiodic Loaded Loop Antennas (SALLA) that are perpendicular to each other. The antenna stations have a typical spacing of approximately 200 m. Tunka-Rex is triggered by the photomultiplier array of Tunka. This array is a non-imaging air-Cherenkov array measuring in the energy range from about 10^{16} eV to 10^{18} eV. The goals of Tunka-Rex are a cross-calibration between the Cherenkov and the radio technique and to determine the radio precision for shower observables like X_{max}[5] and energy.

Yakutsk At the Yakutsk air shower array the radio activities had a renaissance since 2008 (Knurenko et al., 2010). In total 12 antennas were deployed operating in the effective bandwidth of 28 to 40 MHz co-located with the Yakutsk particle detector array. The highest energy radio events by now have been measured by Yakutsk but compared to current arrays the quality of data seems to be limited.

CROME CROME stands for Cosmic Ray Observation via Microwave emission and was an experiment at the KIT Campus North. In addition to some low frequency antennas CROME consisted of dish antennas working in the extended C ($\approx 3.4 - 4.2$ GHz) and K (≈ 10 GHz) band and was one of the first generation experiments to detect air shower GHz emission via molecular Bremsstrahlung. During the operation time of CROME in total 31 events could be detected (Werner, 2013) in coincidence with KASCADE-Grande which was also providing a trigger for CROME. The detected events are in agreement with mainly a $\vec{v} \times \vec{B}$ dependency and a second order contribution of the Askaryan effect (varying net charge excess) when taking into account the compression of the signal due to Cherenkov like time compression.

MIDAS MIDAS stands for MIcrowave Detection of Air Showers. This experiment was developed and first run in Chicago. In September 2012 it started its operation at the Pierre Auger Observatory (Alvarez-Muniz et al., 2013). It consists of one huge ($10\,\mathrm{m}^2$) parabolic dish used as reflector to focus GHz emission

[5] X_{max} is the atmospheric depth at which the air shower has its maximum amount of particles.

on a 53 pixel feed array operating in the C band, very similar to a fluorescence telescope reflecting the photons on a photomultiplier array. MIDAS is designed and operates in self trigger mode.

AMBER AMBER stands for Air shower Microwave Bremsstrahlung Experimental Radiometer and was built at the University of Hawaii (Gorham et al., 2008). An upgraded version of AMBER was built at the Pierre Auger Observatory in order to detect GHz emission in coincidence since June 2011. AMBER consists of a large dish reflecting the GHz radiation on a feed array with mixed antenna feeds, working in the C and K band.

EASIER (GHZ) EASIER stands for Extensive Air Shower Identification with Electron Radiometer and follows a different approach to detect microwave emission from extensive air showers (Luis, P. Facal San, 2013; Gaïor, 2013). Within the EASIER approach in 2012 in total 61 surface detector stations of the Pierre Auger Observatory were deployed with low gain feed horns operating in the C band looking upwards with a very large field of view. EASIER and ANITA are the only air shower detectors other than CROME that have reported evidence for an air shower detection in the GHz regime.

CHAPTER 3

LOPES 3D Experimental Setup and Calibration

The aim of the **LO**FAR **P**rototyp**E** **S**tation LOPES was to demonstrate that air showers can be detected with prototype hardware developed for LOFAR. This was done via digital radio interferometry and proven in 2004. Since then LOPES was reconfigured several times to further develop the radio technique. LOPES strongly benefits from its ideal position within the well understood and calibrated particle detector array KASCADE-Grande which provides a trigger and high-quality air shower parameters. These parameters are used as input for the radio reconstruction of air showers. LOPES started in April 2003 with 10 inverted v-shape antennas that had been aligned in the east-west direction. In February 2005, LOPES was extended to 30 east-west aligned antennas. From December 2006 to December 2009 LOPES measured the radio emission from air showers at 25 positions. In this setup at 10 positions the antennas had been east-west aligned, at another 10 positions they had been north-south aligned and at 5 positions LOPES was measuring with east-west and north-south aligned antennas. In the latest and last setup LOPES was equipped with a new antenna type, the so-named tripole antenna. With these antennas the positions were reduced to 10 since every station used 3 of the 30 available electronic channels. The tripole antenna consists of three dipoles that are east-west, north-south and vertically aligned. This was done to study the benefits of additional measurements with vertically aligned antennas, which is the main topic of this thesis. The change of the antenna type and antenna positions demanded a recalibration of the complete array. In this chapter the hardware and the calibration of LOPES 3D are presented. LOPES was dismantled in the beginning of 2013. Parts of this chapter have been already published by the author in reference (Apel et al., 2012a).

3.1. KASCADE and KASCADE-Grande

KASCADE stands for KArlsruhe Shower Core and Array DEtector and was a particle detector array which was built on the Campus North of KIT in order to measure the spectrum of cosmic rays in the energy range from 10^{14} to 10^{17} eV. KASCADE consisted in total of 252 scintillator detector stations distributed in a regular grid of the dimension 200 m times 200 m. The detector stations were grouped in clusters of four times four stations. The outer KASCADE detector stations were additionally equipped with muon detectors in order to be sensitive to the electron/muon ratio which is an energy and X_{max} sensitive quantity. The layout of the KASCADE detectors is shown in figure 3.1.
In order to be sensitive to primary particle energies up to 10^{18} eV KASCADE was upgraded in 2003 with 37 additional detector stations, the so-called KASCADE-Grande extension. These stations were formerly used in the EAS-top (Aglietta et al., 1989) experiment and are aligned in a hexagonal grid with an average distance between the detector stations of 130 m. The KASCADE-Grande detectors are sensitive to muons, electrons, positrons and hadrons. The layout of the KASCADE-Grande extension is shown in figure 3.2.

3.1.1. Trigger Conditions for LOPES

At an industrial like environment, like at KIT, the radio background is very high. Therefore, a radio self trigger is difficult. In order to detect the radio emission from cosmic ray air showers LOPES needs to be triggered externally, which is done either by KASCADE, or KASCADE-Grande. The trigger is optimized to not lose any interesting events. This is possible since the infrastructure at KIT and the average trigger rate of 1-2 per minute allows to store every event. The interesting events are the ones that have their core in the fiducial area of the detector and have a primary energy larger than 10^{16} eV. To be able to record all these events, the following condition was found for KASCADE. LOPES stores the event if 10 out of the 16 KASCADE clusters have triggered (Horneffer, 2006). A cluster triggers if 10 out of the 16 detectors huts in this cluster have a signal over threshold. For KASCADE-Grande the stations are grouped in hexagons, see figure 3.2. A hexagon consists of 6 surrounding stations and a central station. To have a trigger, all 7 stations of a hexagon are required to have a coincident signal over threshold. If the hexagons with the central stations 9, 10 and 13, cf. figure 3.2, have a coincident trigger the event is stored with LOPES.

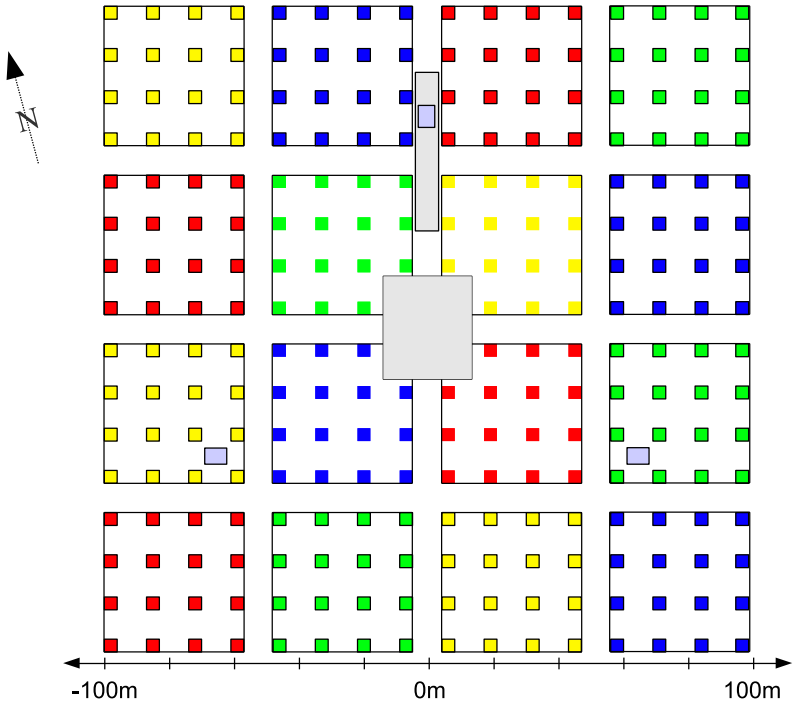

Figure 3.1.: Layout of the KASCADE detector array. Clusters are color coded. The inner four clusters (squares without black edging) do not have a muon detector. The extensions of KASCADE are shown in grey. For further information on the extensions see figure 3.10.

3.2. LOPES 3D

The last and final setup of LOPES is called LOPES 3D. In this configuration with 10 antenna stations LOPES measured from May 2010 to January 2013. The outstanding feature of this setup is the new antenna type applied. The new antenna is a tripole antenna and consists of three dipoles perpendicular to each other. With the measurements performed in this configuration the benefits of an additional measurement with vertical antennas are studied. In the following the experimental setup of LOPES will be described and the calibration procedure for this experiment will be discussed.

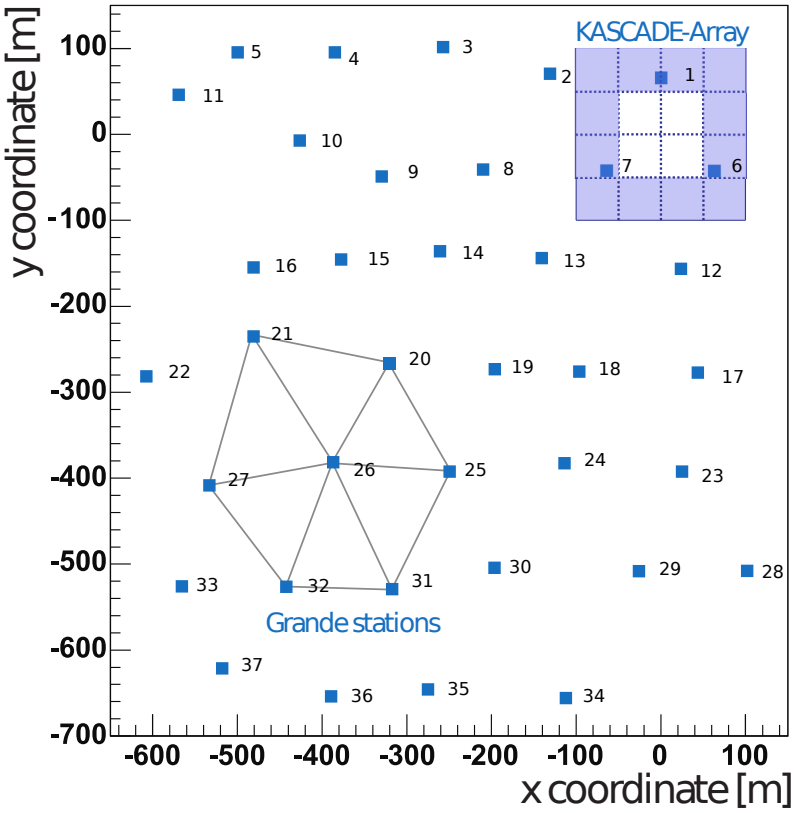

Figure 3.2.: Layout of the KASCADE-Grande detector array with one indicated trigger hexagon. In the upper right corner the KASCADE array is indicated including the muon detectors in the shaded area, see also figure 3.1.

3.3. Signal Chain and Data Acquisition

In figure 3.3 the signal chain of LOPES 3D, which was adopted from LOPES 30, is shown schematically. A signal that arrives at the antenna is converted to a voltage at the antenna foot-point. This voltage is then amplified in the low noise amplifier (LNA) to be transmitted to the receiver module of LOPES (RML). In the RML the data are amplified, filtered to the bandwidth of LOPES 3D ($40 - 80$ MHz) and digitized. After this the data are transmitted via optical fibres to the TIM-module (twin input memory module). In this module the data are saved in a ring buffer. If KASCADE-Grande sends a trigger, the ring buffers are read out and the data are send via ethernet from the frontend PC to the "lopesmaster" PC. In the lopesmaster PC the data from each frontend PC are combined to a binary file. The 30 electronic channels of LOPES 3D are organised in three clusters. The single components of the signal chain are explained in more detail in the following.

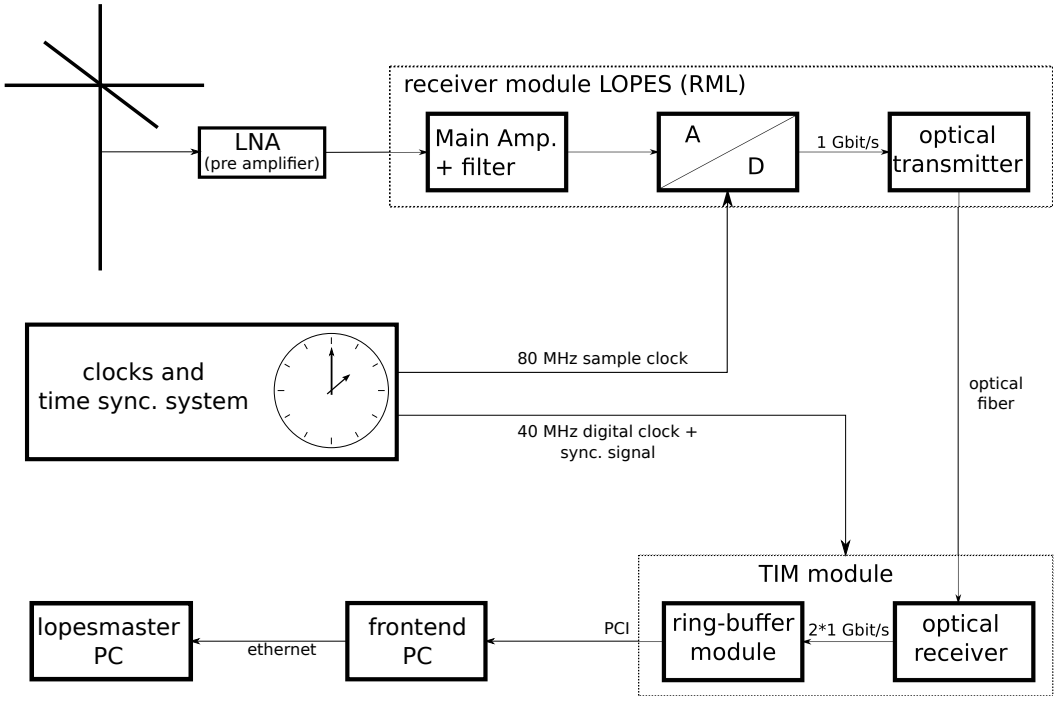

Figure 3.3.: Scheme of the LOPES hardware components adapted from LOPES 30.

Pre-amplifiers (LNAs) The deployed LNAs are two-channel LNAs with a double bias t-coupling to be fed via phantom feeding with a voltage from $7-24\,\mathrm{V}$. At the input of the LNAs there is an over-voltage suppressor and a second order high-pass filter to avoid saturation effects. These LNAs were originally designed for the Auger Engineering Radio Array AERA (Huege, T. et. al, 2010; Abreu et al., 2012). They are based on a MMIC (monolithic microwave integrated circuit) amplifier module which is unconditionally stable[1]

Main Amplifier The requirements for the main amplifier were $16\,\mathrm{dB}$ gain, a noise figure [2] of less than $10.3\,\mathrm{dB}$ (Horneffer, 2006) and an output intercept point (OIP2) of more than $+32\,\mathrm{dBm}$. This is achieved with the commercially available ZFL-500HLN amplifier, which has a noise figure of 3.8 dB, a gain of $19\,\mathrm{dB}$, and is therefore far better than the requirements.

Filter After the transmission through the coaxial cables, the signal is amplified and filtered to a bandwidth of 40 to $80\,\mathrm{MHz}$. This frequency range was chosen

[1] An amplifier is considered to be unconditionally stable when no connected source or load can cause instabilities.

[2] The noise figure characterizes the amount of noise which an additional part of the signal chain adds to the signal.

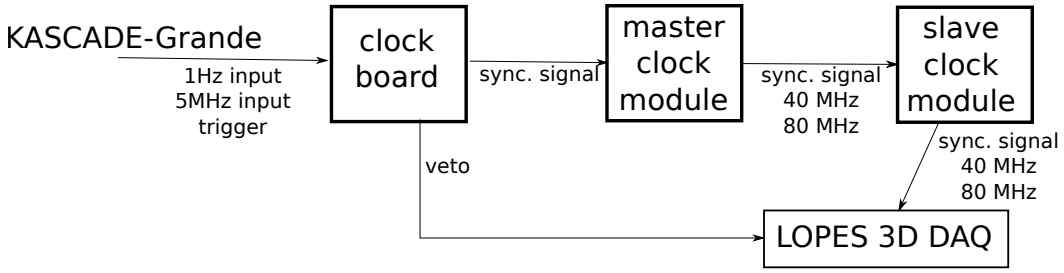

Figure 3.4.: Scheme of the LOPES 3D clocks and time synchronisation system.

since the LOFAR prototype hardware which is used for LOPES has a sampling frequency of 80 MHz. With this the recordable frequency window is limited to 40 to 80 MHz when measuring in the 2nd Nyquist domain (Nyquist, 1928). In addition, almost no broadcasting carriers are present in this frequency range and the radio emission of air showers is coherent in this frequency range. The steep flanks of the filters result in an effective bandwidth of 43-76 MHz for the first ten electronics channels, respectively 43-74 MHz for electronics channels $11 - 30$. The different effective bandwidths originate from the different filter modules used for the update from LOPES 10 to LOPES 30. Because of the different effective bandwidths, the data are filtered digitally to a bandwidth of 43-74 MHz in the analysis software.

Digitizer /ADC The analogue to digital converters (ADC) sample the signal with a rate of 80 MHz which is provided by a clock distribution board. When sampling a signal with a frequency which is twice the bandwidth, no information on the signal gets lost since one is operating in the 2nd Nyquist domain (Nyquist, 1928). The original signal can be reconstructed in the analysis by up-sampling. The ADCs have a maximum input voltage of ± 1 V and a resolution of 12 bit.

Memory Buffer /TIM module The digitized data are transferred via fibre optics to the memory buffer module. Each module is connected to a PC via PCI-connector and has two inputs. In the 2 GB ring buffer either 12.5 s of data can be handled when reading one input or 6.25 s when reading both inputs. After an external trigger from KASCADE(-Grande) the recorded data of 0.8 ms centred around the time of the trigger are read.

Clocks and Time Synchronisation System To achieve precise timing and a synchronization with KASCADE-Grande, several clock modules have to operate in a synchronized mode. In case of LOPES, the clocks are synchronized via cables. An overview of the system is shown in figure 3.4.

Clock Board The clock board receives a 1 Hz input, a 5 MHz input, and the trigger signal from KASCADE-Grande. This board then generates a sync signal, a time stamp, and a veto to block triggers for the time of the readout. The read time (= dead time) of LOPES 3D is approximately 1 s which is small compared to the trigger rate of approximately $\frac{2}{\text{min}}$. The sync signal is transferred to the Master clock module. The veto signal is transferred to LOPES DAQ, more precisely the TIM module.

Master Clock Module In this module the 40 MHz and 80 MHz digital clocks are generated and passed through along with the sync signal to the three slave clock modules.

Slave Clock Module In each of the three clusters of LOPES 3D a slave clock module distributes the 40 MHz digital clock and the sync signal to the memory buffer modules and the 80 MHz digital clock to the ADCs and the TIM module.

3.4. Beacon

The beacon is a reference source that continuously emits sine waves at three constant frequencies. With the phase differences of these sine waves the timing of the experiment is monitored, improved and corrected for missing sampling cycles (Schröder et al., 2010; Schröder, 2011). This technique provides an event-by-event calibration of the timing. Since the beacon is not visible in the new vertically aligned antennas of LOPES 3D it was modified to be compatible to the new setup. The beacon antenna type was changed from a dipole antenna to a SALLA. This was done to test whether the SALLA can be used as beacon antenna for AERA. By rotating the antenna by $45°$, it is assured that the signal of the beacon can be seen in all three directions of one station. In addition, the emitting power had to be increased for two reasons:

1. the emitting SALLA has a lower gain than the former beacon dipole antenna.

2. the rotation of the SALLA leads to a loss of power received in the different orientations.

A scheme of the SALLA as used for the beacon is shown in figure 3.5.

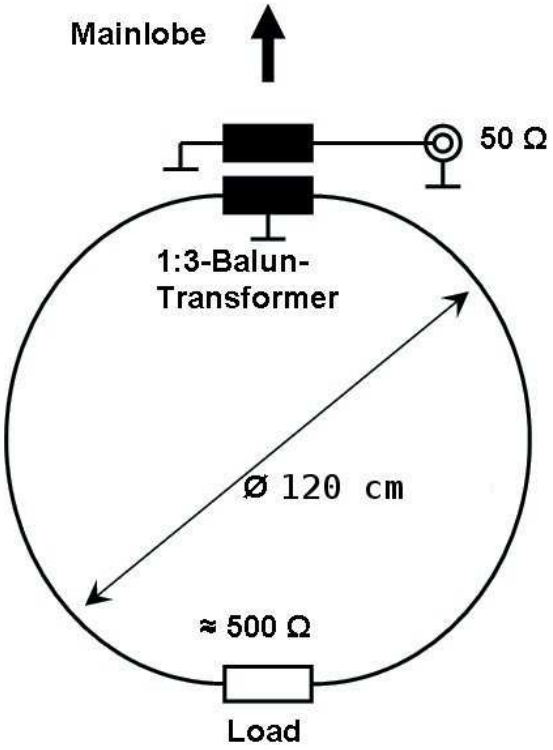

Figure 3.5.: Scheme of the SALLA beacon antenna.

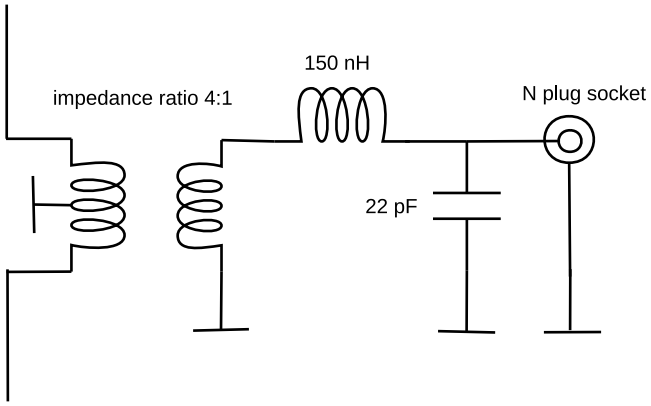

Figure 3.6.: Scheme of the matching of one dipole antenna of the tripole to a channel of the LOPES 3D experiment.

Figure 3.7.: Photography of a tripole antenna as used for LOPES 3D.

3.5. The Tripole Antenna for LOPES 3D

The antenna type used for LOPES 3D is a tripole which consists of three dipoles perpendicular to each other, see figure 3.7. One dipole has a length of $1.3\,\mathrm{m}$ which is $\frac{\lambda}{4}$ of the central wavelength of the frequency band of LOPES (40-$80\,\mathrm{MHz}$). Each dipole couples to a coaxial cable via a Ruthroff balun (balancer unbalancer) transformer (Ruthroff, 1959) including LC-matching, see figure 3.6. The impedance ratio of $4{:}1$ was chosen to match the characteristic impedance, $200\,\Omega$, of the antenna to the $50\,\Omega$ of the cable. To suppress noise from broadcasting stations the balun is connected with an LC-circuit (low-pass filter). The shielding of the coaxial cable is grounded at both endings. To determine the quality of an antenna the standing wave ratio (SWR) is measured. In this measurement a sine wave is transmitted to the antenna which creates a standing wave. The SWR is defined as the fraction of the signal coming back of the signal sent $\frac{\mathrm{sig_{in}}}{\mathrm{sig_{reflected}}}$. This gives a measure of the ability of the antenna to emit (and receive) at a certain frequency. Everything that is emitted by the antenna will not be reflected, which means that the lower the SWR the better the antenna emits. For cosmic ray measurements the detected pulse is broadband, therefore the antenna should be sensitive over a wide frequency band. The measured SWR is shown in figure 3.8. It can be seen that for the tripole antenna the SWR is low and rather constant over the desired bandwidth, i.e. 40-$80\,\mathrm{MHz}$. The SWR has a minimum at the centre frequency of the bandwidth but does not change strongly (standard deviation 0.78, relative

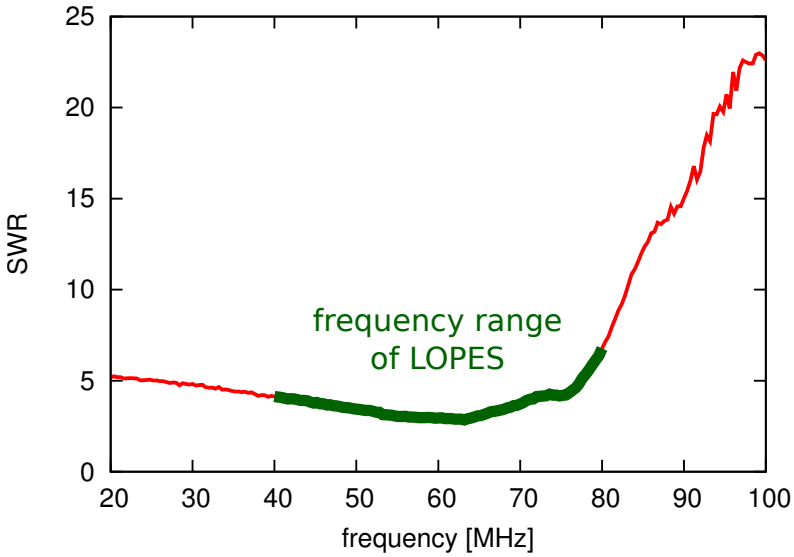

Figure 3.8.: Measured standing wave ratio (SWR) for one dipole of the tripole. Due to the filter electronics only the frequency range shown as bold line is of interest.

change 43% for the effective frequency range $43\,\mathrm{MHz}$ to $74\,\mathrm{MHz}$) over the bandwidth of LOPES. It is desirable to have homogeneous antenna characteristics over the whole frequency band. The measured normalized impedance Smith-chart for this antenna is shown in figure 3.9. Here the data are normalized to $50\,\Omega$. Both, the SWR and the Smith-chart were measured from 20 to $100\,\mathrm{MHz}$, where the interesting region for LOPES (40 to $80\,\mathrm{MHz}$) is highlighted in bold. From the Smith-chart all the characteristic quantities of an LCR circuit, in this case the dipole antenna, can be derived. For a certain point in the Smith-chart, the SWR can be determined by:

$$\mathrm{SWR} = \frac{1+|r|}{1-|r|} \tag{3.1}$$

where r is the distance between origin and the given point. The impedance and phase can directly be read off. The green lines of the grid mark the imaginary part and the blue lines mark the real part. The phase is the angle between the imaginary axis and the line connecting the origin with the point one wants to characterize. As seen in figure 3.9 the response of the antenna, in phase and amplitude, is homogeneous over the design frequency band. This is necessary to avoid biases from the antenna side when measuring a broadband signal, like cosmic ray air showers.

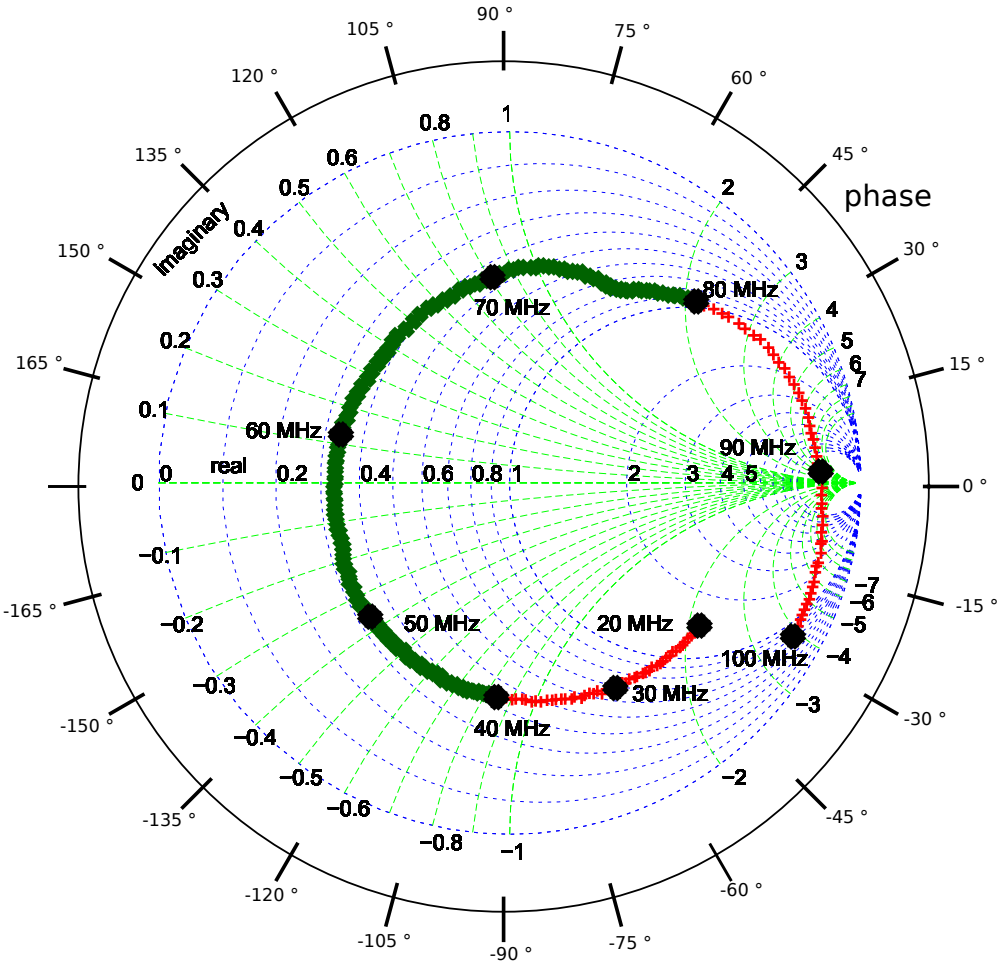

Figure 3.9.: Measured Smith-chart for one dipole of the tripole. The line highlighted in bold green corresponds to the frequency bandwidth of LOPES (40 to 80 MHz), the red crosses mark the measured range of 20 to 100 MHz.

3.6. Calibration

The changed setup of LOPES required a completely new calibration. The individual steps will be explained in the following. A more detailed description of the calibration procedures in general is available in references (Nehls et al., 2008; Schröder et al., 2010).

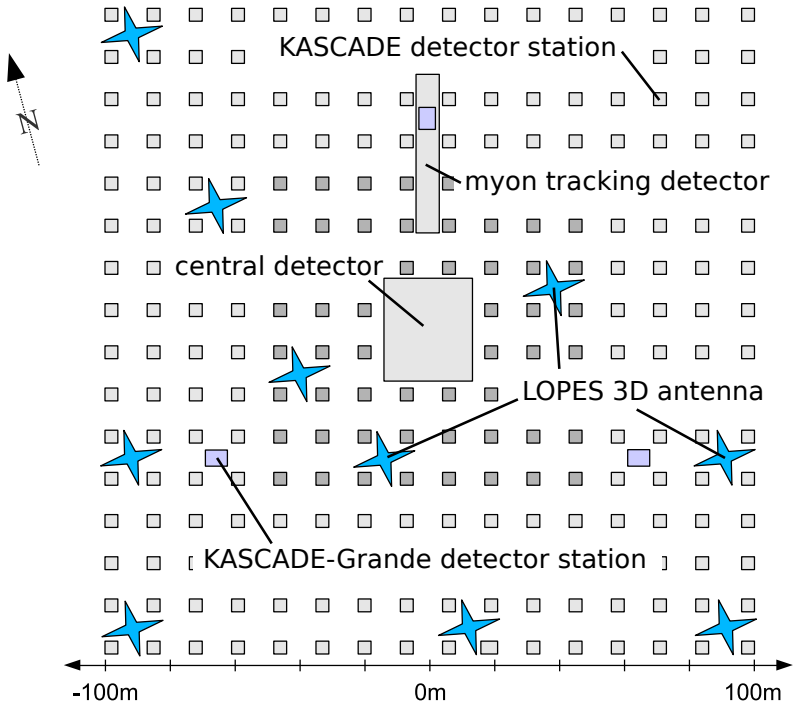

Figure 3.10.: The positions of the 10 LOPES 3D antenna stations within the KASCADE array. The grey squares mark the positions of the KASCADE detector huts and the blue stars the positions of the LOPES 3D antennas stations.

3.6.1. Dimensions of the Antenna Grid

For digital radio interferometry the required time accuracy is determined by the maximum measured frequency. To have a proper cross-correlation and beam-forming procedure (= interferometric analysis) the phase uncertainty has to be lower than $30°$. This translates in an allowed time uncertainty in the order of 1 ns. The maximum allowed uncertainty in the position is determined by dividing the maximum allowed uncertainty in time by the speed of light and is in the case of LOPES ≤ 30 cm. The positions of the LOPES 3D antennas have been measured with a differential GPS which has an accuracy in the position of ≈ 2 cm in x and y and ≈ 2.5 cm in z. In addition, a systematic uncertainty of 5 cm has to be taken into account since the position of the phase center of the antenna is not exactly known. With a total uncertainty in the position of ≤ 10 cm the requirement of less than 30 cm is clearly fulfilled.

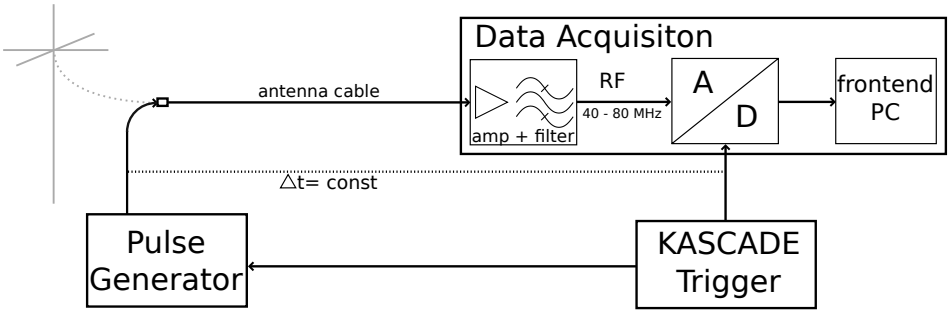

Figure 3.11.: Scheme of the electronic delay measurement using a pulse generator triggered by the regular KASCADE-Grande trigger. The antenna is displayed to show where it would be connected but, it is unplugged during the delay measurement.

3.6.2. Timing

For the LOPES experiment, the timing calibration is done in two steps. There is a measurement of the electronics delay as well as an event-by-event calibration done with a beacon. The measurement of the electronics delay is performed in the following way:
The antenna cable is connected to a pulse generator instead of the antenna. Both, the pulse generator and the readout are triggered by the regular KASCADE-Grande trigger. The delay between the readout trigger and the emission of the pulse by the pulse generator is always the same and does not need to be known since only the relative timing of the channels is of interest. The time when the pulse appears in the recorded trace is then used to calculate the time shifts between the different channels.
The beacon is a radio emitter which emits sine waves at 3 different frequencies, at 53.1, 63.5 and 68.1 MHz. These signals can be used to monitor and correct timing drifts in the electronics on an event-by-event basis. Since the phase differences of one sine signal in two different channels are constant if the timing is constant, a change of these phase differences can be used to correct the timing within one period of the sine (Schröder, 2011). Because the beacon emits three frequencies, 53.1, 65.5 and 68.1 MHz, the timing correction can be performed over more than just one period, and with a higher accuracy. The absolute value of the delay at these frequencies needs not to be known, because only the differential timing of the different channels is of interest. With the beacon, time drifts can be corrected with an accuracy of approximately 1 ns. In summary, with the measurement of the timing with a pulse generator and the monitoring of timing drifts with the beacon, an overall accuracy of about 1 ns is achieved, as required.

3.6.3. New Method for Time Calibration

Within the scope of this thesis, a new precise time calibration method was developed and tested. The method makes use of the phase differences at different frequencies. To determine these phase differences, sine waves with different frequencies are sent through the cables of the LOPES experiment to the DAQ. Then the phase of the sine is determined and compared to the phase of the same frequency in another channel. The phase difference is directly translated to a relative delay τ according to $\tau = \frac{\Delta\phi}{2\cdot\pi\cdot f}$. With the new method the frequency dependent delay of the electronics can be determined, see figure 3.12. In this example the relative delay between two channels of the LOPES 3D experiment is shown for frequencies between 55 and 65 MHz. The variation between different measurements is very small and much better than the required 1 ns accuracy. This method is mainly limited by the intrinsic detector noise and therefore gives the best achievable results.

3.6.4. Amplitude Calibration

In order to know which field strength at the antenna corresponds to which ADC value, the complete electronic signal chain needs to be calibrated. For that purpose, a reference source with a known emission power is arranged above each antenna station to calibrate the individual channels (Nehls et al., 2008). Requirements for a valid measurement are:

1. Having a distance between the antenna and the reference source of approximately 10 meters, since the reference source is calibrated for this distances.

2. Measuring the horizontal position and the height of the reference source by differential GPS with an accuracy of a few cm, which corresponds to an uncertainty in the received power $\leq 2\%$

3. Having an alignment of the reference source with the antenna within $\leq 7\,^{\circ}$ deviation which corresponds to 2% variation of the received power due to misalignment of the linear polarizations of the transmitting and receiving antenna.

4. Avoid metal parts near the reference source since metal parts can reflect the signal and thereby disturb the calibration measurement.

With the measured ADC values and the calculated field strength at the antenna the frequency dependent amplification factor of each channel can be computed and applied in the analysis.

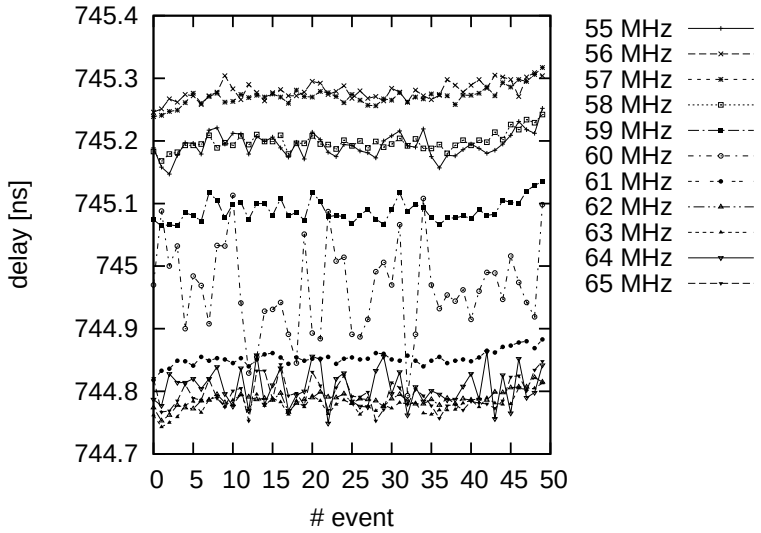

(a) 50 measurements for frequencies between 55 and $65\,\mathrm{MHz}$ in $1\,\mathrm{MHz}$ steps

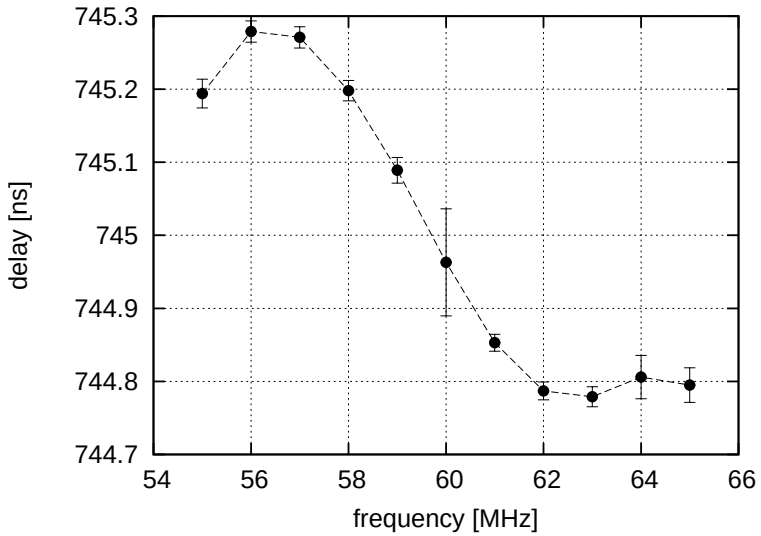

(b) frequency dependent delay (averaged values), the error bars are the standard deviation of the 50 measurements per frequency shown on top.

Figure 3.12.: Relative delay between channel 6 and channel 14 of the LOPES 3D experiment.

The calibration of channels connected to vertical antennas is difficult since these antennas are very insensitive to signals from the zenith. Thus a calibration with the reference source above the antenna will suffer large errors from horizontal noise. A calibration with the reference source next to the antenna not high above ground will suffer from reflections from the ground and the KASCADE

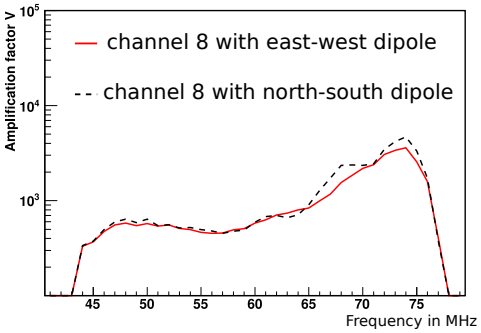

(a) The amplification factors for channel 8 from two measurements. For the first measurement the vertical channel was connected to the north-south oriented dipole, for the second measurement it was connected to the east-west oriented antenna. An overall agreement within 15.6% in power between both measurements can be observed.

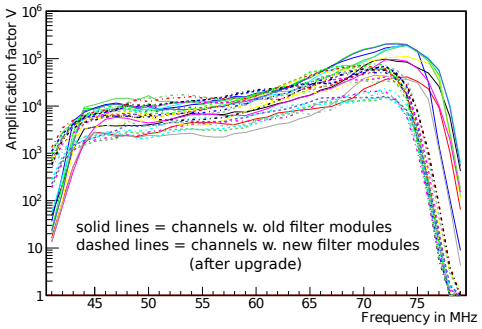

(b) The amplification factors of all 30 channels of the LOPES 3D experiment. The main sources for the different amplification factors are different cable lengths and different filter modules of the first LOPES upgrade.

Figure 3.13.: Amplification factors for the electronics channels of the LOPES 3D experiment.

huts and is therefore not feasible. However, the manufacturing standards of the dipole antennas are very high and the absolute amplitude calibration is performed only for the channel electronics and not the antenna. It is therefore possible to calibrate a channel that was originally connected to a vertically oriented antenna when temporarily connecting it to to a horizontally oriented antenna, see also figure 3.13(a). Hence the best way to calibrate channels connected to vertically orientated antennas is to connect a horizontally orientated antenna instead.
The amplification factors in power of the analogue chain (Filter, cable, LNA, main amplifier etc.) of all 30 channels are shown in figure 3.13(b). These factors describe the frequency dependent attenuation of the signal chain. Features that originate from the different electronics, like, e.g., steeper filter flanks from the different filters used for 20 of the 30 channels can be observed. The difference in the absolute values between the factors shown in figures 3.13(a) and 3.13(b) originates from the consideration of the distance between receiving antenna and calibration source. For the amplification factors (figure 3.13(b)) the distance between calibration source and receiving LOPES antenna is taken into account whereas for the demonstration of the method as shown in figure 3.13(a) the distance was constant and therefore is ignored in the analysis.

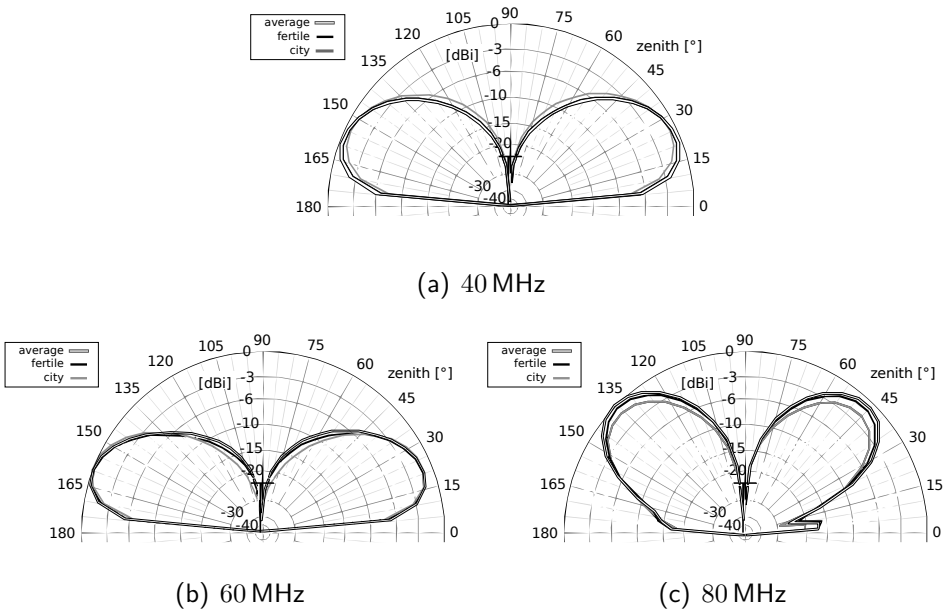

(a) $40\,\mathrm{MHz}$

(b) $60\,\mathrm{MHz}$

(c) $80\,\mathrm{MHz}$

Figure 3.14.: Simulated gain pattern of the vertical dipole of one tripole at different ground conditions and frequencies. The average ground is used for the LOPES antenna simulation. The different ground conditions are the standard conditions as provided in 4NEC2X (Voors, 2005) and are characterised by conductivity and dielectricity. The irregularity in the gain pattern for $80\,\mathrm{MHz}$ originates from the mounting steel pole but does not affect the measurement of cosmic ray air shower radio emission since it only affects the gain pattern at a very insensitive region.

Incorporation of the Antenna Gain Compared to LOPES 30

The change of the antenna type for LOPES 3D demanded a new simulation of the gain pattern. The gain pattern describes the frequency and direction dependent sensitivity of an antenna. More details on the antenna gain can be found in chapter 5. Measuring the gain pattern is complicated and requires relatively large facilities to have well defined conditions to ensure reproducibility of the results. These facilities were not available and we use simulated gain patterns instead. For simulating the gain pattern, the Numerical Electromagnetic Code (NEC2) (Voors, 2005) is used, see figure 3.14. An average ground was chosen since at the KASCADE site the ground conditions depend on the season, and with the average ground lowest deviations from the different possible conditions are achieved. With these simulations the maximum deviation in the total gain pattern between the different ground conditions is determined to be less than $0.75\,\mathrm{dB}$ ($\leq 19\%$ in amplitude), including frequency dependence. This of course is a worst case scenario and therefore can be used as maximal systematic uncertainty estimation in the simulated gain pattern. This uncertainty affects all antennas in

the same way which means that the different ground conditions only need to be included in the systematic uncertainty when the absolute value is of interest. At the LOPES site there is no monitoring for the ground conditions. Hence an event-by-event correction is not possible. The gain patterns of the east-west and norths-south horizontally orientated dipoles are in principle the same but rotated by 90°. The mounting steel pole has very little influence on the measurement since it only affects the gain pattern at very insensitive regions. In the analysis the gain pattern is treated in the following way: The pattern is simulated in 2 MHz frequency steps with a resolution of 5° in azimuth and elevation. This simulation is stored and used for an interpolation which then gives the value needed for the specific analysis. The treatment of the antenna gain in the analysis is discussed more deeply in chapter 5.

3.7. Monitoring

With the reconfiguration of LOPES, the monitoring was upgraded and improved. Before the upgrade, only the average noise level of each channel was calculated every 20 min and the vertical atmospheric electric field was displayed (Nehls, 2008).
During operation of LOPES 3D, in addition every 20 min the last recorded event is analysed in the following way:
First, an uncalibrated spectrum is derived by performing an FFT (fast Fourier transform) of the raw ADC counts, second the average noise level is calculated. The third and the most important step is the determination of the present phase differences of the sine signals from the beacon. The uncalibrated spectrum is calculated quickly and gives a good impression of the overall performance of the experiment. An example is shown in figure 3.15(a).
These spectra are not corrected for electronic effects such as attenuation in the cables, the gain pattern of the antenna etc. The main purpose of deriving such spectra is to monitor the condition of the experiment. A damaged cable or narrow-band noise sources can be identified very easily without detailed knowledge of the experimental hardware setup. In figure 3.16 the average noise level is shown for a period of 13 days. A periodic variation can clearly be seen. Such kind of plots are used to monitor the background noise development with time. Moreover, deterioration processes of the signal chain can be observed with such plots, e.g., the ageing of an individual LNA will lead to a smaller signal and smaller deviations between maximum and minimum or the stepwise breakdown of a filter module will be seen as a raise in the average noise. It is important to monitor long term

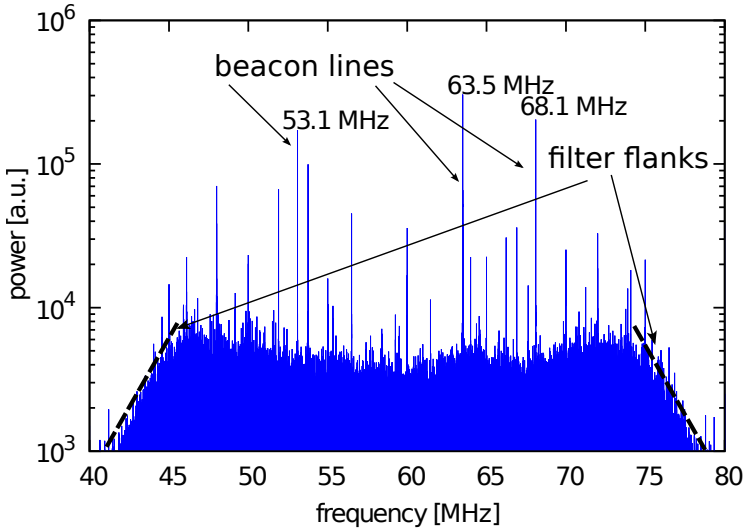

(a) Raw spectrum (FFT of the ADC-counts) taken from the LOPES monitoring. On the Y-axis the power is plotted in arbitrary units and on the X-axis the frequency in MHz. The three beacon frequencies 68.1, 63.5 and 53.1 MHz and many more radio frequency interference (RFI)-lines that are suppressed during the analysis can be observed.

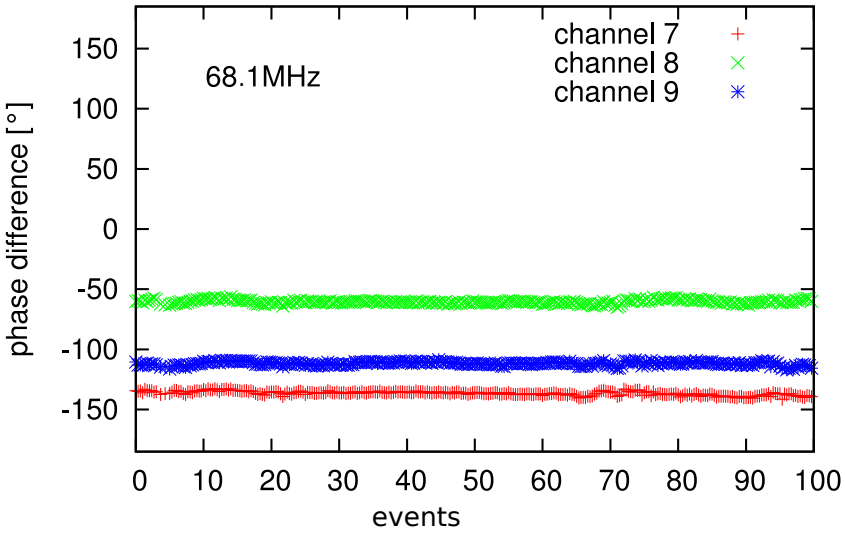

(b) The phase differences in degrees of the 68.1 MHz beacon signal of channels 7, 8, 9 is shown on the Y-axis and on the X-axis the number of events. The measurement of these 100 events corresponds to a time of 33 hours and 20 minutes, the low scatter of the phase differences indicates a stable timing of LOPES 3D.

Figure 3.15.: Plots from the LOPES online monitoring system.

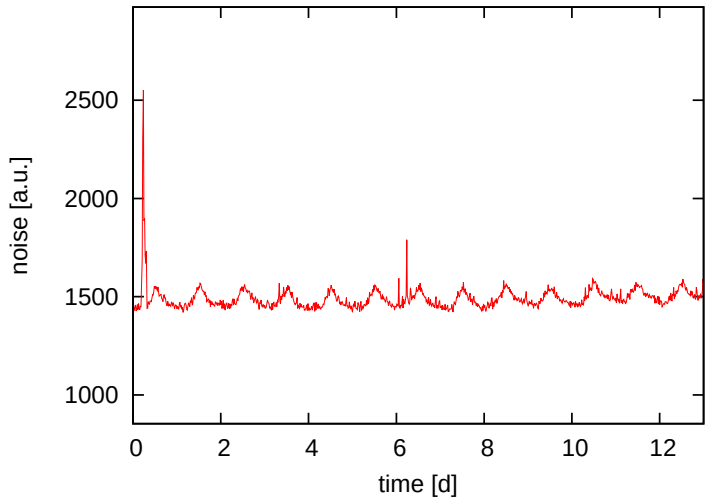

Figure 3.16.: Background noise measured with an east-west aligned antenna for a period of 13 days in uncalibrated power units. The occurring peaks most likely originate either from a nearby construction site or are connected to a solar flare.

changes since it is very hard to identify them in an event-by-event analysis. The background noise can be used to monitor the experiment, when comparing different channels. In figure 3.17 the background noise is shown with a 24 hour period. The drift of the maximum demonstrates that this variation originates from the galactic transit. For the galactic transit a period of 23 hours and 56 minutes is expected which corresponds to a drift of 2 hours per month. Thus a total shift of 12 hours is expected between both plots. At the LOPES site most of the galactic radio emission is buried in anthropogenic noise, therefore the amplitude of the variation is relatively small.
With the beacon, LOPES is provided with an event-by-event monitoring of the timing. It is desirable to monitor this event-by-event time calibration, because this is a very sensitive quantity. For the monitoring the phase differences of the sine waves emitted by the beacon are calculated for every channel and displayed, see figure 3.15(b).

3.7.1. Monitoring Examples for Non-Regular Operation

During a calibration measurement for LOPES the effect of a strong emitter (i.e the calibration source) on the derived monitoring spectrum could be studied. In figure 3.18 such a spectrum is shown. The high narrow band peaks indicated a strong noise source near the antenna. A noise source near the data acquisition

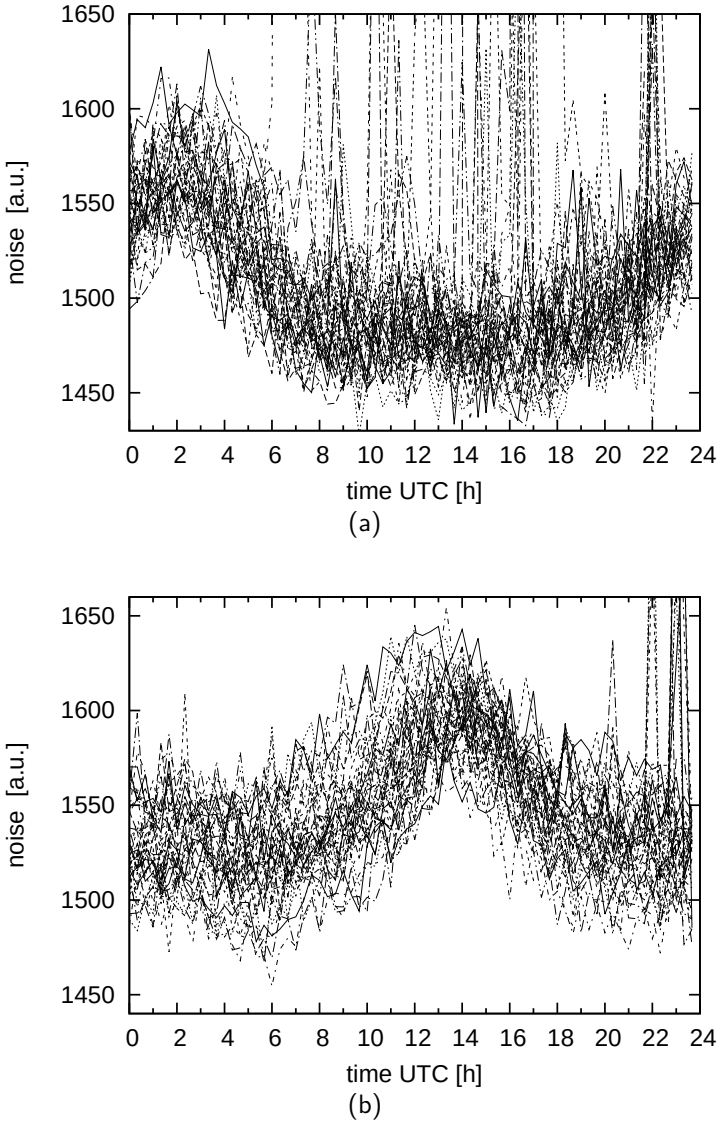

Figure 3.17.: Background noise measured with an east-west aligned antenna over a period of 39 days plotted with a 24 hour period for a measurement from May to June (a) and a measurement from November to December (b) 2011 to check if the noise originates from the galactic transit, each line is the measurement from one day.

could be excluded because the other channels in the same cluster were not affected.

In figure 3.19 the effect of a non-emitting beacon on the phase plots can be observed. This phase plot was generated during a test measurement with the AERA beacon hardware. The time when the AERA beacon was switched on can clearly be seen, by the stable phase differences.

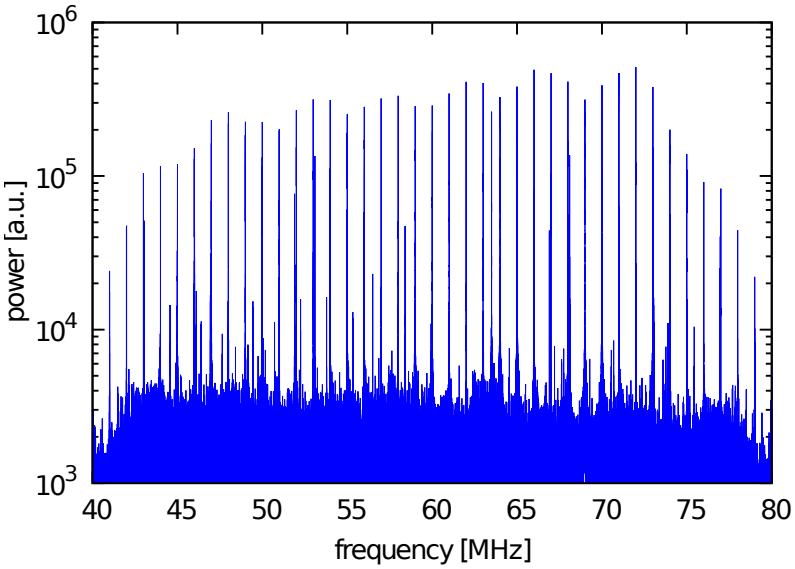

Figure 3.18.: Raw spectrum (FFT of the ADC-counts) like in the LOPES monitoring, recorded during a LOPES calibration campaign. On the Y-axis the power is plotted in arbitrary units and on the X-axis the frequency in MHz. The frequency comb of the calibration source is clearly visible.

In figure 3.20 the recorded phase differences during a test run of an AERA data acquisition software on the LOPES hardware are shown. The events up to approximately event 1450 were recorded with the LOPES standard software for comparison. The events after were recorded with the AERA software. It can be seen that the AERA software, in that developing state, had a bug where the time traces occasionally were randomly picked out of the ring buffer. This can be seen by the scatter of the phase differences after the switch of the DAQ software. Furthermore a preferred offset, indicated by the second accumulated phase difference in the plot, was found. These flaws in the AERA DAQ software originated from a wrongly initialized ring buffer and are fixed by now.

3.8. Conclusion

In this chapter the calibration of LOPES 3D was discussed and the monitoring system was introduced. Within the calibration for the first time a Smith-chart for the used antenna type was measured, furthermore a calibration procedure for the absolute calibration of channels connected to vertical dipoles was developed and tested. The accuracy of the calibration is the same as for LOPES 30 (Nehls et al., 2008) except for the gain pattern of the antennas. Due to the higher sensitivity

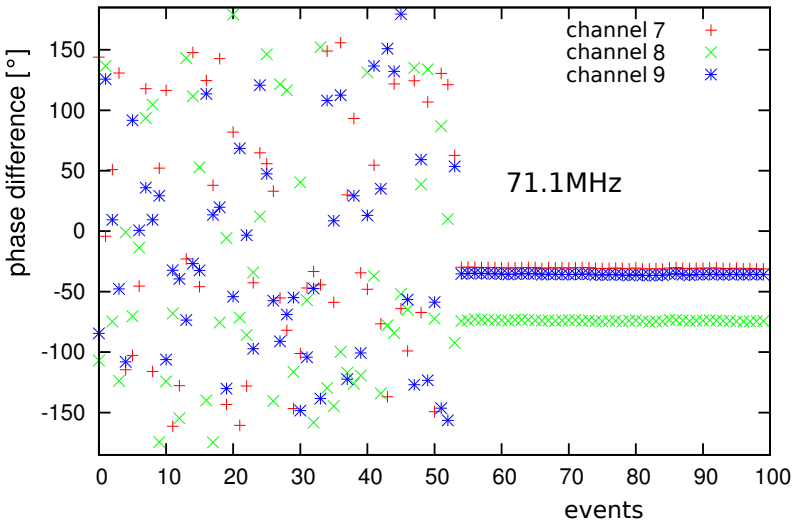

Figure 3.19.: The phase differences in degrees of the 71.1 MHz AERA beacon signal of channels 7, 8, 9 is shown on the Y-axis and on the X-axis the number of events. The beacon was switched on at event 53, which can be seen by the stabilizing of the reference phases.

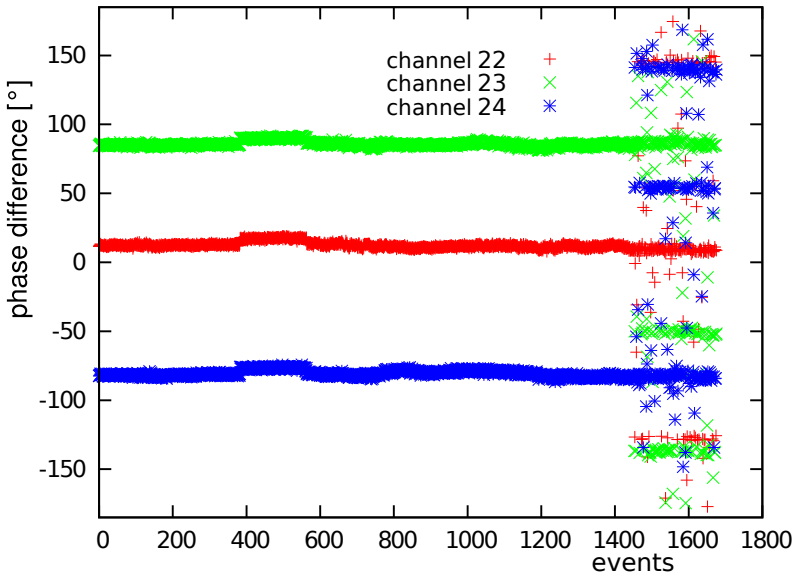

Figure 3.20.: The phase differences in degrees of the 71.1 MHz AERA beacon signal of channels 22, 23, 24 is shown on the Y-axis and on the X-axis the number of events.

to the ground the uncertainty in the antenna gain was estimated to 19%. A new method for the time calibration was introduced and the sensitivity of LOPES 3D to the Galactic plane was demonstrated.

CHAPTER 4

Data Selection and Consistency Check

In this chapter the preselection and categorization of the different datasets available for the analysis of the radio signal from cosmic ray air showers measured with LOPES 3D are described and motivated. These sets contain all data that were recorded when LOPES received a trigger from KASCADE or KASCADE-Grande which survived specific cuts on the KASCADE or KASCADE-Grande reconstruction, respectively. The main reason for dividing the data into different sets is the trigger source (i.e KASCADE or KASCADE-Grande) which goes along with a different reconstruction of the input parameters to the LOPES reconstruction. Another aspect is related to the geometry: the data sets are divided into a regular data set (i.e. showers with zenith angles smaller than $45°$), in the following referred to as "normal" and a data set containing showers with zenith angles larger than $45°$, in the following referred to as "inclined showers". An overview of the different data sets is presented in table 4.1. Furthermore, the data are tested for consistency with former observations. This way it is proven that LOPES 3D measures cosmic rays.

4.1. Preselection for the Standard Reconstruction

To reduce the computing time for the radio event analysis, only interesting events (reconstructed by either KASCADE or KASCADE-Grande) are preselected. The majority of events are triggered even though no radio signal can be measured. Typical cuts on the KASCADE, respectively KASCADE-Grande (in the following

Table 4.1.: Overview on the preselected data samples of the LOPES 3D recorded data.

trigger + reconstruction	main cuts	name as referred to in this work	number of events
KASCADE	$E \geq 10^{17}$eV $\theta \leq 45^{\circ}$	KASCADE-normal	614
KASCADE-Grande	$E \geq 10^{17}$eV $\theta \leq 45^{\circ}$	Grande-normal	2330
KASCADE	$E \geq 10^{17}$eV $\theta \geq 45^{\circ}$	KASCADE-inclined	978
KASCADE-Grande	$E \geq 10^{17}$eV $\theta \geq 45^{\circ}$	Grande-inclined	595

referred to as Grande) data, for the normal data set are:

- Successful reconstruction of the shower by KASCADE or KASCADE-Grande
- An energy of the primary particle of $\geq 10^{17}$ eV, since at these energies LOPES 3D starts to become effective
- The shower core has to lie inside the fiducial area of KASCADE and/or Grande
- Times with high particle collision rates from ANKA (ANKA, 2014) (like e.g. a beam dump) are excluded

With these criteria in total 614 events reconstructed by KASCADE and 2330 events reconstructed by KASCADE-Grande survive the preselection for events with a zenith angle θ of less than 45° during the run time of LOPES 3D (May 2010 to January 2013). For Grande when going to showers with zenith angles θ larger than 45° fewer events are preselected than for the normal data set, this is due to the loss of sensitivity for these geometries, see also figure 4.8 and section 4.2. For KASCADE the case is different, here more events are preselected. This is due to the sensitivity of KASCADE up to zenith angles of $\approx 80^{\circ}$ in combination with the overestimation in energy for very inclined showers, cf. section 4.2.1 of this chapter. The shower core distribution and the arrival directions are shown in figure 4.1. The energy distributions are shown in section 4.2.1.

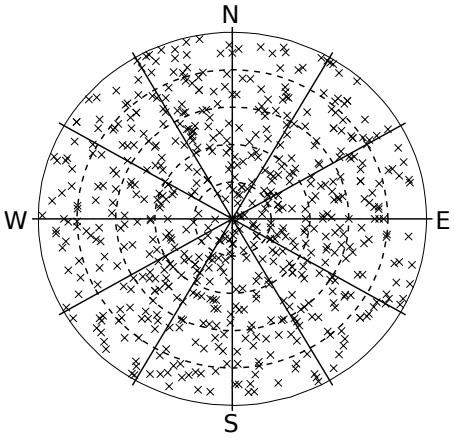

(a) Polar plot of the arrival directions of the input events that pass the KASCADE cuts. $\theta = 0°$ is in the center of the plot and at the edge $\theta = 45°$

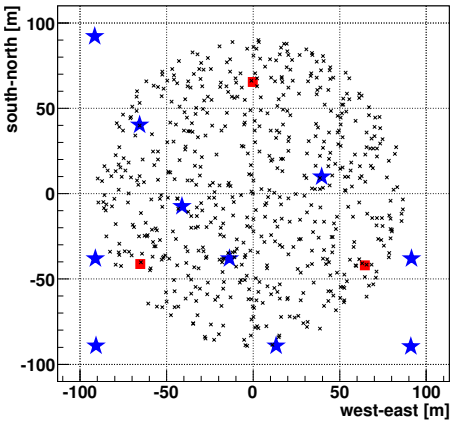

(b) Shower core distributions of events passing the KASCADE cuts.

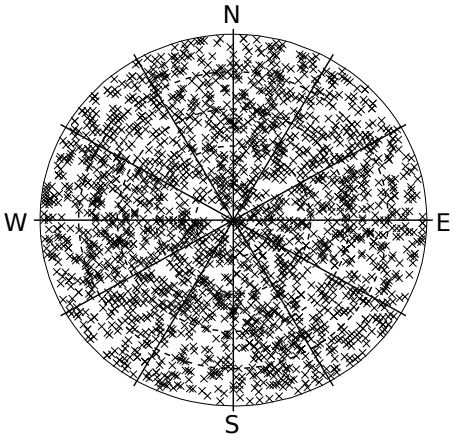

(c) Polar plot of the arrival directions of the input events that pass the Grande cuts. $\theta = 0°$ is in the center of the plot and at the edge $\theta = 45°$.

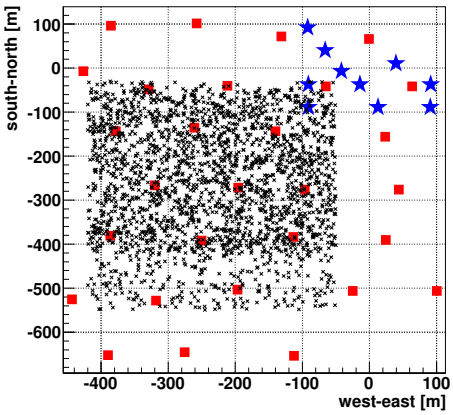

(d) Shower core distributions of events passing the Grande cuts. The absence of events in the lower part originates from the trigger conditions optimized for LOPES.

Figure 4.1.: Arrival directions and core distributions for showers with $\theta \leq 45°$. The blue stars mark the positions of the LOPES 3D antennas and the red squares mark the positions of the KASCADE-Grande detectors. The KASCADE huts have been left out in this representation for clearness. The different shapes of the core distributions originate from the different fiducial volumes of KASCADE and KASCADE-Grande, respectively.

4.1.1. Selection Criterion for the Radio Reconstruction

To select events with a successful reconstruction of the radio signal, the signal-to-noise ratio (SNR) of the cross-correlation-beam (CC-beam)[1] is used. So far in the LOPES analysis the cut on the CC-beam SNR was estimated by looking at the SNR distribution and defining a value by hand. The signal height is defined as the maximum height of a Gaussian fit to the CC-beam pulse at ≈ -1.8 µs cf. figure 4.2. $t_0 = 0$ µs ist the time when the trigger signal from KASCADE-Grande is received. The noise level is defined as the RMS of the CC-beam in the time window of 204.8 to 45.5 µs before the pulse (a noise calculation after the pulse would be also desirable but is not feasible since the KASCADE-Grande photomultiplier tubes introduce RFI (radio frequency interference) which harms a proper noise calculation). Within this thesis a formal criterion was developed to calculate the CC-beam SNR cut for the LOPES 3D analysis. Thus, for the first time in LOPES a formal description to calculate the SNR-threshold is available. To define a signal-to-noise ratio cut on the CC-beam, the amount of events that pass this cut is plotted as a function of the threshold for the cut. A drop in the number of events at an SNR value of ≈ 3 for KASCADE-reconstructed and ≈ 2 for KASCADE-Grande-reconstructed events can be seen, cf. figures 4.3 and 4.4. The events that have a small SNR value are considered as noise events. Events at higher SNR are assumed to contain a measured radio signal from the air shower. To determine the turning point, the absolute value of the derivative of this curve was calculated. To this derivative a Landau function was fitted. The Landau function is defined by the distribution function $\Phi(\lambda)$ with the density $\phi(\lambda)$ according to equations 4.1 and 4.2.

$$\phi(\lambda) = \frac{1}{2\pi i} \int_{c-i\infty}^{c+i\infty} e^{\lambda s + s \ln(s)} \mathrm{d}s, \tag{4.1}$$

$$\Phi(\lambda) = \int_{-\infty}^{\lambda} \phi(\lambda) \mathrm{d}\lambda, \tag{4.2}$$

For further details on the implementation of the Landau fit within the ROOT framework we refer to Kölbig and Schorr (1984). With the parameters of the Landau function (most probable value MPV and sigma σ) the event selection can be adopted for the desired purpose (high statistics vs. high purity). The variable σ is a measure of purity. The most probable value of the Landau function defines the turning point of events with only noise vs. events with signal. Thus, $MPV + x \cdot \sigma$ is a defined dynamic criterion for each analysis that can be adopted independently of the experimental setup for any signal over threshold based analysis, where x is

[1] The CC-beam is a measure of the coherent received power and is explained in more detail in chapter 6.

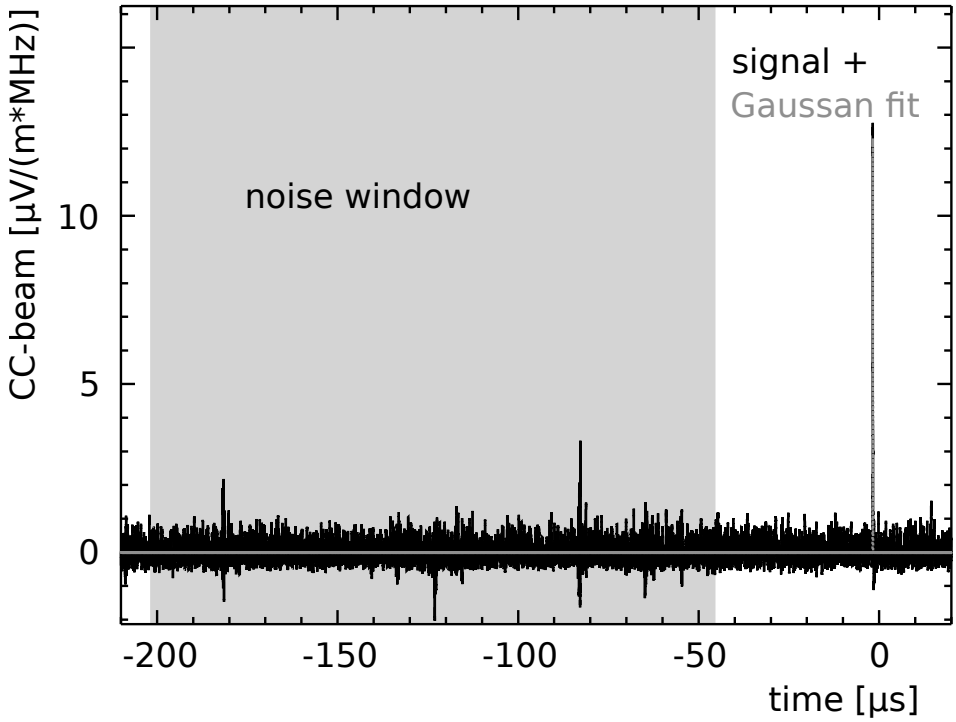

Figure 4.2.: Trace of a CC-beam in black and the Gaussian fit to the CC-beam in grey and the noise window (grey shaded area).

used as a parameter to control the purity in a sample. The different values for $x = 5.05$ for KASCADE and $y = 3.9$ KASCADE-Grande-triggered events can be explained by the average distance of the radio antennas to the shower axis of the triggered events. With a larger distance to the shower core, as it is the case for KASCADE-Grande-triggered events, it is more likely to have either a signal in all antennas or no signal in all antennas. In contrast to that, for KASCADE-triggered events, the probability of an event in which some antennas receive a signal and some do not receive a signal is higher. A reconstruction using data from antennas with and without signal will result in a larger MPV and a broader σ for the derived distributions as it is observed in figures 4.3 and 4.4.

4.1.2. Consistency Checks

To test the functioning of LOPES 3D, several checks were performed and evidence for a proper working singal chain was found e.g. for:

1. Galactic noise visible in data, cf. chapter 3, figure 3.17.

2. Solar flares seen in data.

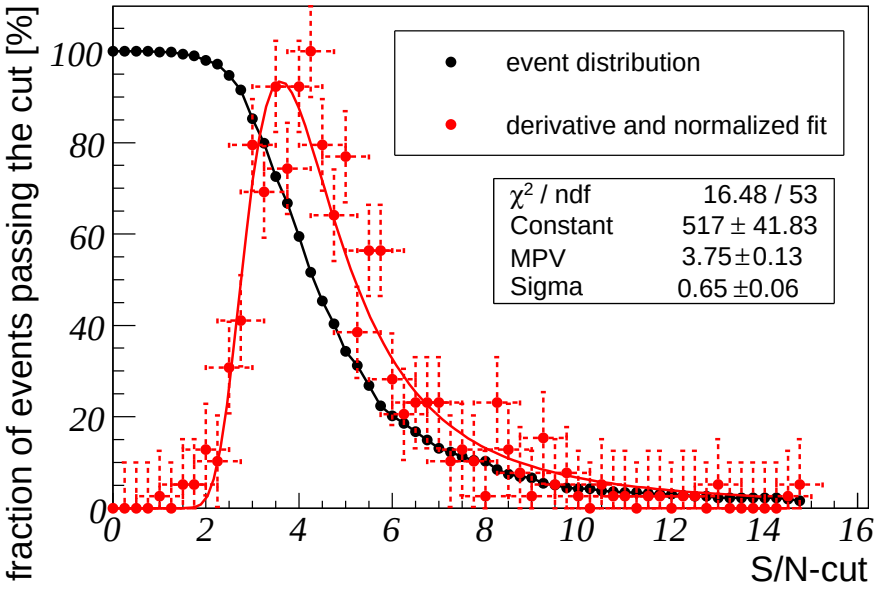

Figure 4.3.: Fraction of events passing a certain SNR-cut as a function of the cut value (black dots and line) for KASCADE triggered events, the absolute value of the derivative of this distribution normalized to 100 (red dots) and a Landau distribution (red line) fitted to it. X-error bars are two times the bin width, y-error bars assumed to be constant and 10% of the maximum fraction.

3. Average event rate is meets the expectations.

4. Measurements are in agreement with the $\vec{v} \times \vec{B}$-model, a model that described data in the past to first order.

Solar Flares

One possibility to check the performance of an antenna array is to look for solar flares that can be seen as a rise in the average amplitude of the radio signal. With LOPES 30, solar flares were observed and since then the sun was becoming even more active during the run time of LOPES 3D. Thus, solar flares should be detectable with LOPES 3D too, see figure 4.5. Here a solar flare detected with LOPES 3D is shown. In total 4 out 9 analysed solar flares were detected with LOPES. In LOPES there is no trigger for solar flares, but since these events last for several ten minutes one can search for them in the standard triggered data. This was done by looking at dynamic spectra during the time of a solar flare. For further details please consider Lehr (2011).

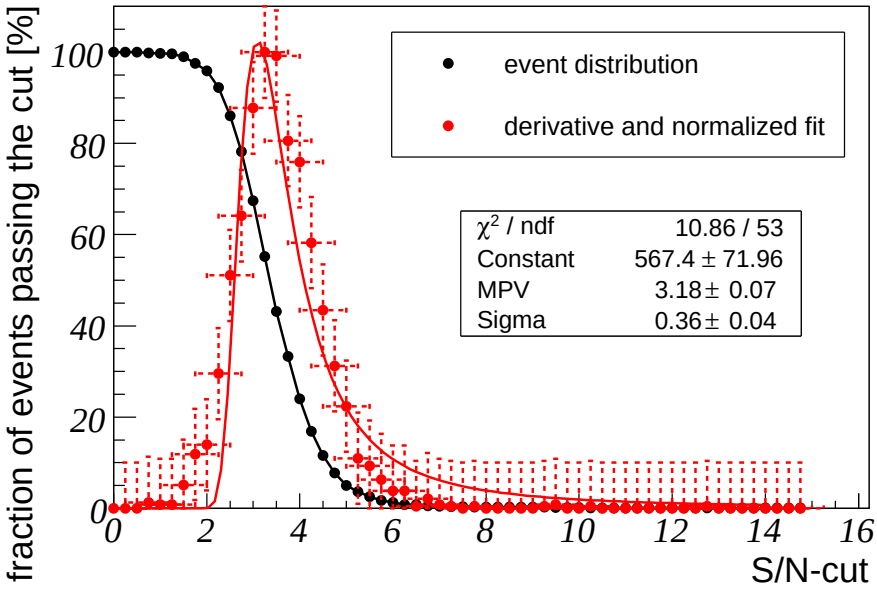

Figure 4.4.: Fraction of events passing a certain SNR-cut as a function of the cut value (black dots and line) for KASCADE-Grande triggered events, the absolute value of the derivative of this distribution normalized to 100 (red dots) and a Landau distribution (red line) fitted to it. X-error bars are two times the bin width, y-error bars assumed to be constant and 10% of the maximum fraction.

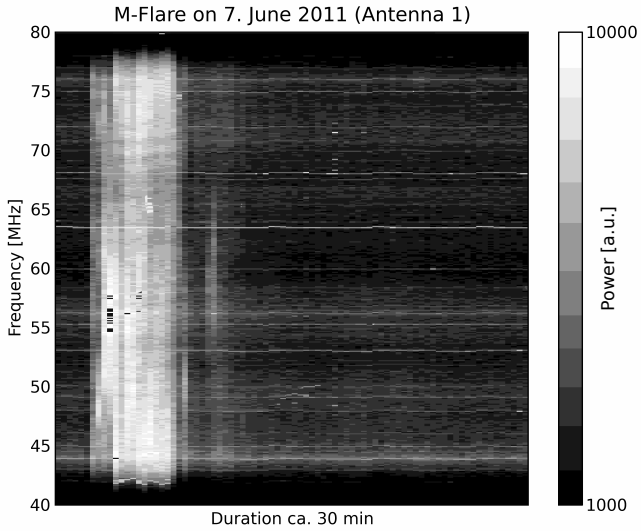

Figure 4.5.: Solar flare (M-flare) (Lehr, 2011) recorded with LOPES 3D. Power in arbitrary units.

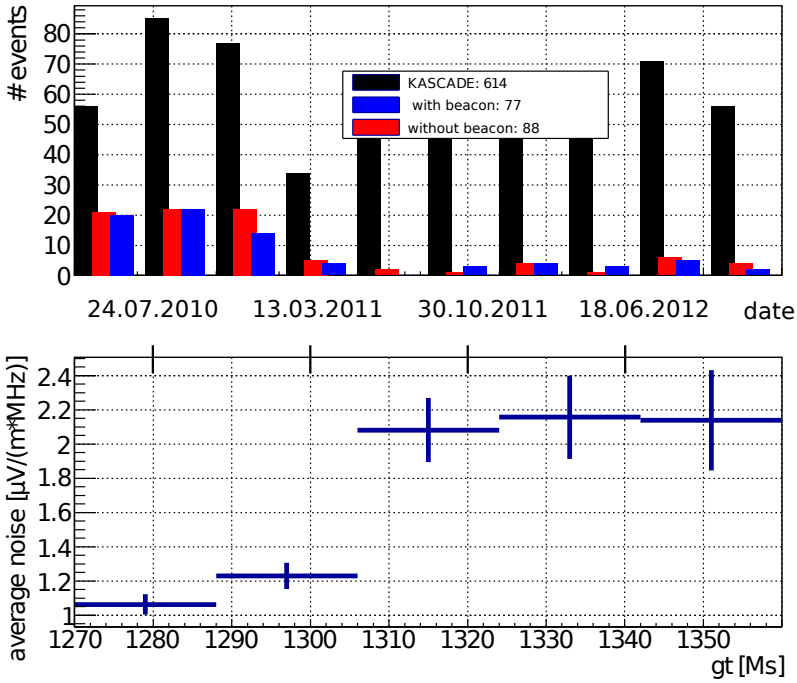

Figure 4.6.: Event rate of reconstructible events with (blue) and without (red) beacon correction (top) and background noise over the lifetime of LOPES 3D (bottom).

Average Detection Rate

The expected rate of cosmic rays detected with LOPES 3D is used as a criterion to judge the performance of the experiment. With LOPES 30 the average rate was approximately $3.5\,\frac{\text{events}}{\text{week}}$ (Nehls, 2008) depending on the quality cuts. When reducing the number of antennas, the expected event rate can be estimated by exploiting the dependence of the detection rate on the number of antennas stations. For this estimation we use two different approximations for the detection threshold of a radio interferometer. For the first the threshold is decreasing linearly when increasing the number of antennas which is a valid estimation if the measured pulse shape is different in each antenna. For the second approximation the threshold goes with $\sqrt{\text{number of antennas}}$, which is a valid assumption if the pulse shape is identical in each antenna (Huege, 2004). The pulse shape is, depending on geometry, not identical but correlated in each antenna which makes the combination of these two scenarios a good estimator for the limiting cases. When reducing the number of antenna positions by a factor of 3, the energy of the primary cosmic ray needs to be 3 ($\sqrt{3}$) times higher to be detected. With the spectral index $\lambda = 2$ of the integrated cosmic ray spectrum, $f(E) \approx E^{-\lambda}$, the event rate can be estimated to be $f = 3^{-2}$ ($f = (\sqrt{3})^{-2}$) times lower. Thus the expected event rate of LOPES 3D is estimated to be a factor of $\frac{1}{9}$ ($\frac{1}{3}$) lower

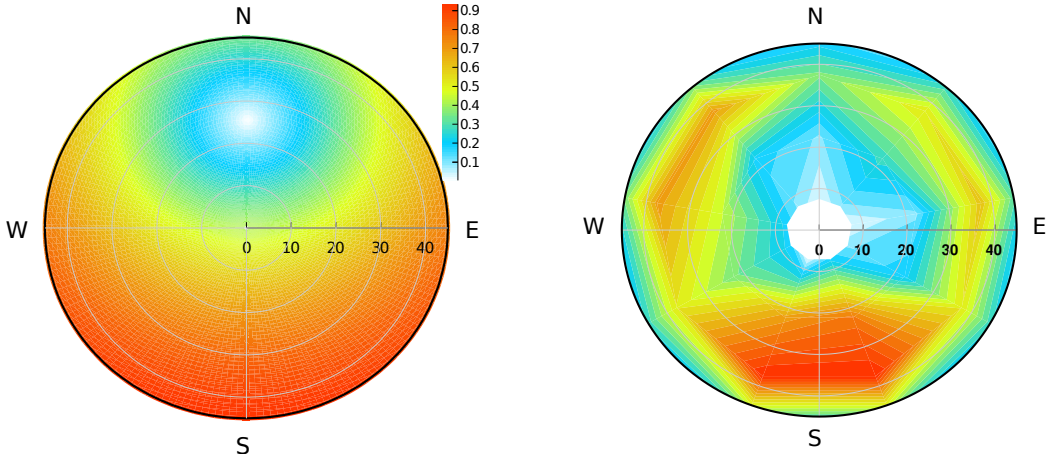

(a) Prediction of the relative strength of the radio signal for the dominant emission mechanism, the $\vec{v} \times \vec{B}$-model.

(b) Polar plot of the relative rate of air showers detected with LOPES 3D as a function of arrival directions.

Figure 4.7.: Prediction of the dominant emission mechanism according to the $\vec{v} \times \vec{B}$-model (left) and the arrival direction of the air showers detected with LOPES 3D (right).

than the one of LOPES 30. For this analysis all events that have a SNR higher than a threshold of $MPV + 2 \cdot \sigma$ are considered to contain a reconstructed radio air shower signal. For this check only a subset of the data recorded before the period of increased background noise (see figure 4.6) were taken into account and the simple gain approximation was applied to be comparable with former results. With 56 detected events in 6 months of data taking a detection rate of $1.75 \, \frac{\text{events}}{\text{week}}$ is achieved which is even better than the optimistic expectation for 10 antenna positions. This is because LOPES 3D is sensitive to all components of the electric field vector and therefore has a higher sensitivity than a setup with 10 antennas that are only sensitive to the east-west component of the electric field vector. Using only events that were observed in the east-west direction the event rate is $1.06 \, \frac{\text{events}}{\text{week}}$ and fits well the expectations (see also table 4.2).

Comparison with the $\vec{v} \times \vec{B}$-Model

The most straightforward and convincing approach to check the performance is to compare measured events with a model that makes good predictions for a polarization and amplitude estimate as a function of shower arrival direction. In figure 4.7, a comparison of LOPES 3D data with the $\vec{v} \times \vec{B}$-model is shown. The $\vec{v} \times \vec{B}$-model is a model that is able to describe the overall directional dependence

Table 4.2.: Event rates of LOPES 3D.

Average rate	[events/week]
LOPES 30 (EW)	3.5
LOPES 3D expected (EW):	
for a scaling with number of antennas	0.39
for a scaling with $\sqrt{\text{number of antennas}}$	1.17
LOPES 3D (only EW)	1.06
LOPES 3D (all)	1.75

of the radio detection efficiency well and was used by several other radio experiments such as CODALEMA (Ardouin et al., 2009) and the Auger Engineering Radio Array AERA (Kelley, 2011). According to this model, the electric field vector is described by a $\vec{v} \times \vec{B}$ dependence, where $\vec{v}$ is the arrival direction of the air shower and $\vec{B}$ is the geomagnetic field. Most of the events measured with LOPES 3D should be well described by this model. In this comparison the radio signal was reconstructed using the simple gain approximation (cf. chapter 5). For the comparison shown in figure 4.7, a normalized emission vector predicted by the $\vec{v} \times \vec{B}$-model is used and compared with arrival directions of the 56 reconstructed cosmic ray air showers also used in the analysis above. For this plot only the region of interest, i.e. showers with zenith angle $\theta \leq 45^\circ$ is shown. The region of interest is defined by the data sample used for this analysis which only contains showers with zenith angles $\theta \leq 45^\circ$. A comparison of the relative amplitude with the relative number of detected arrival directions can be done on a qualitative level, because the more signal is above a certain threshold the more likely this shower can be reconstructed.
In addition to that, also the rates of events detected in the different polarizations can be checked. For the east-west component 33 events survived the quality cut of a signal-to-noise ratio of the CC-beam SNR $\geq MPV + 2 \cdot \sigma$. For the north-south component 18 events survived and for the vertical component 11 events survived. This is expected since most of the radio emission from extensive air showers is emitted in the east-west component, second most in north-south, and the fewest in vertical.

Stability of the Event Rate

Another possibility to check the ability of an antenna array to measure cosmic rays is to check the the stability of the rate of reconstructible events as KASCADE-Grande is very stable. Note that for this analysis the selection criteria are stronger,

it is very important to differentiate between detecting an air shower and being able to reconstruct shower parameters from an air shower. The comparison described above was done only for detected air showers whereas in this consideration the more powerful quantity of reconstructible air showers is checked. To be able to detect air shower parameters from a measured radio signal the minimum amount of participating antennas was set to be larger than six and at least 50% of the received power has to be coherent. In figure 4.6 the rate of reconstructed events is shown. A drop at a global time stamp (gt)[2] of $\approx 13 \cdot 10^8$ s (i.e.$\approx$ March 2011) can be observed. This originates from the radio reconstruction only, since the triggered and reconstructed events by KASCADE do not decrease in their rate. Thus a trigger problem can be excluded. Another possibility could be a problem with the beacon, used to improve the timing. This is possible since the bioliq-group (bioliq, 2014) has started to build a large metal reactor right next to the antenna array in 2010, which in addition is directly in the line of sight between beacon and some antennas of LOPES 3D. This huge metal structure can influence the received phases and therefore the per-event timing calibration of the single channels. To check this hypothesis the beacon correction was switched off in the analysis, see also figure 4.6 top. If the drop in the event rate were caused by distorted beacon phases, the event rate of the reconstruction without the beacon correction would not contain this drop. The fact that this drop is also present in the reconstruction not using the beacon excludes problems connected with the beacon. Another possibility would be a rise in the background noise. This would be the worst case since there is no possibility to improve on the event rate. In figure 4.6 bottom the background noise for the runtime of LOPES 3D is shown. It can be seen that at a gt of $\approx 13 \cdot 10^8$ s the average background noise was increased by a factor of ≈ 2 which explains the drop in the event rate. With a factor of two higher noise, the signal in single antennas needs to be a factor of two higher to be detected. This means that to first order the energy needs to be a factor of two higher. With an index $\lambda = 2$ of the integrated cosmic ray spectrum, $f(E) \approx E^{-\lambda}$, this leads to a decrease of the event rate by $\frac{1}{4}$. The rate before the increase in the noise was ≈ 1.35 events/week the rate after was $\approx .23$ events/week, thus a decrease of $\approx \frac{1}{6}$ was observed. The agreement in time of the observed drop in the event rate shows that it is connected to the rise in the background noise. Nevertheless, the observed event rate after the increase of the background noise was lower than expected by the simple estimation given above. This is because in this consideration only the threshold effect for detecting the signal was considered. Nevertheless, noise can also have an influence on the coherence of the signal. Consequently, as observed, an even higher decrease of the event rate is expected. Without the increasing background noise the expected number of detected events for the live time of LOPES 3D can be estimated to ≈ 130.

[2]The global time are the seconds passed since January 1st 1970 00:00:00.

4.2. Event Preselection for Inclined Showers

Inclined showers have to be treated more carefully since the KASCADE and KASCADE-Grande reconstruction algorithms are not developed and optimized for these shower geometries. In this selection only events with a zenith angle larger than 45° have been considered which causes several challenges for the analysis. The KASCADE-Grande reconstruction has large uncertainties for these geometries which makes a direct comparison of shower parameters difficult. The ground conditions have a larger influence on the measured radio signals, which increases the systematic uncertainty. The shape of the wave front becomes more important due to the larger geometrical distance of the source to the array. This makes inclined showers in principle an ideal method to cross-check the different models for the radio wave front. However due to the small size of LOPES 3D this cannot be probed. So far a cone, a sphere and a hyperbola are implemented in the LOPES reconstruction software as a shape of the wave front (Apel et al., submitted 2014b).
The datasets analysed for this thesis are again divided into two subsets: triggered and reconstructed by KASCADE or KASCADE-Grande, respectively. For the preselection, the cuts on shower parameters were as in the standard selection. The cuts did not have to be modified since the amount of preselected events was adequate to be processed with the given infrastructure. In total 978 events for KASCADE and 595 events for KASCADE-Grande pass the cuts.

4.2.1. Selection Biases

LOPES is externally triggered. This means the triggered and preselected events on which the following analyses are based can be biased by the KASCADE and KASCADE-Grande efficiency. To check for selection biases the distributions of the arrival directions and the core distribution are checked. In figure 4.8 these quantities are shown. It can be seen that KASCADE is sensitive up to zenith angles of approximately 80° which is because of the lower energy threshold for the single detectors compared to Grande (sensitive up to approximately 54°) and the muon detectors.

Muons can penetrate much deeper in the atmosphere and are therefore also prominent in inclined showers, in contrast to electrons and positrons that are absorbed in the atmosphere. Inclined showers are on average observed at a later state of the shower development and at larger distances to LOPES 3D which makes them more challenging to detect. The core distribution of KASCADE has an excess of events in the lower left corner of the array. This is because in this corner

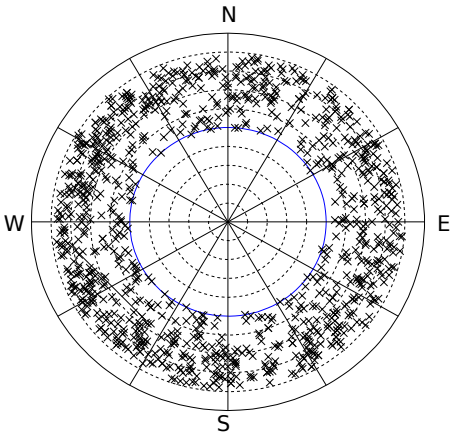

(a) Polar plot of the arrival directions of the input events that pass the KASCADE cuts. $\theta = 0°$ is in the center of the plot and at the edge $\theta = 90°$.

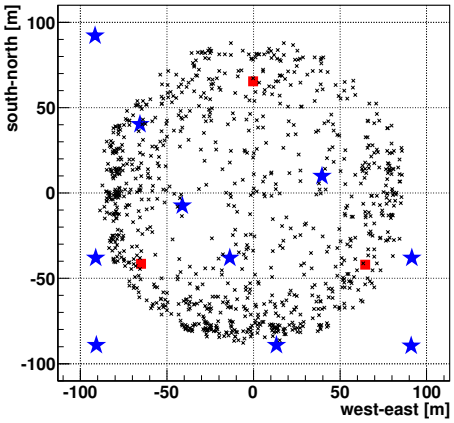

(b) Shower core distributions of events passing the KASCADE cuts. The excess of events on the bottom left originates from the Grande array lying in this direction. With this the sensitivity is slightly increased.

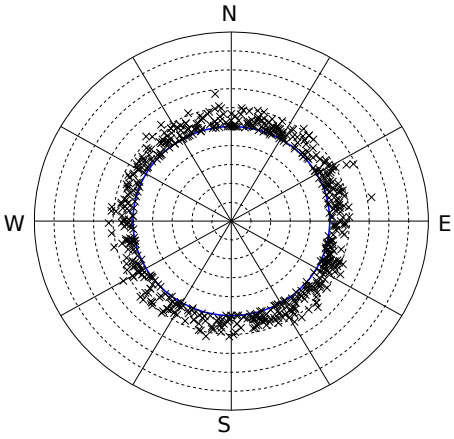

(c) Polar plot of the arrival directions of the input events that pass the Grande cuts. Due to the flat scintillators, the lack of muon detectors and the larger distance between the single detector stations the sensitivity drops very fast for increasing zenith angles.

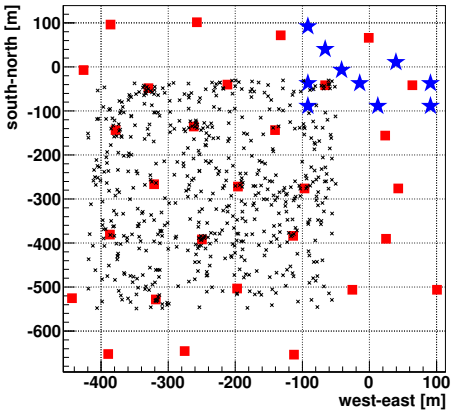

(d) Shower core distributions of events passing the Grande cuts.

Figure 4.8.: Arrival directions and core distributions for inclined showers with $\theta \geq 45°$ (blue line in polar plots). The blue stars mark the positions of the LOPES 3D antennas and the red squares mark the positions of the KASCADE-Grande detectors. The KASCADE huts have been left out in this representation for clearness.

the Grande extension is situated which enlarges the sensitivity[3]. Furthermore an accumulation of cores towards the edge of the fiducial area can be observed. This is due to a wrong reconstruction of the shower cores from events that have cores close to the edges of the fiducial area. A wrongly reconstructed core directly influences the radio lateral distribution. For the Grande-triggered events the cores are equally distributed and as expected the array is less sensitive to more inclined showers because of the missing muon detectors, the higher energy threshold and the wider spacing between the detectors. From the geometrical point of view the selections are unbiased in the sense that:

- there is no accumulation of events in a certain direction for both selections
- the cores of KASCADE-Grande-triggered events are equally distributed

The selections are biased in the sense that:

- the cores of KASCADE-reconstructed events might be wrongly reconstructed if they are close to the edge of the fiducial area
- KASCADE-Grande is only sensitive up to approximately $\theta = 54^\circ$

In figure 4.9 the energy distribution for the KASCADE- and KASCADE-Grande-triggered events, respectively, is shown. For KASCADE-Grande the energy distribution is as expected and in agreement with the events in the standard selection. This is because KASCADE-Grande is sensitive only up to zenith angles of approx 54° and therefore this selection is very close to geometries for which the standard reconstruction is valid. Furthermore fewer events are recorded since the fiducial area for inclined showers is much lower due to the the lower sensitivity to inclined showers. For KASCADE the case is different: here an excess in high energy events can be observed. This is connected to wrongly reconstructed energy. KASCADE is sensitive to zenith angles up to approximately 80° which is far away from geometries for which the standard reconstruction was developed. Indeed, the further inclined the higher the average energy is estimated (figure 4.10). Furthermore, an excess in preselected events can be observed, which originates from the overestimation of the energy for these geometries. Due to this overestimation, more events pass the cut on the energy to be higher than 10^{17} eV. Thus, when analysing these events, larger uncertainties on the energy, the shower cores and the arrival direction have to be assumed. The preselection for inclined events has a much lower purity since more low energy events with no radio signal are contained.

[3]The event classification is done regarding the reconstructed core position. Thus a event detected in KASCADE and Grande will be in the KASCADE selection if its core lies in the fiducial area of KASCADE.

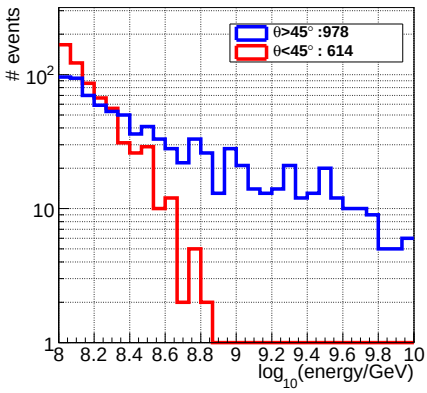

(a) Reconstructed energy distributions for KASCADE triggered events

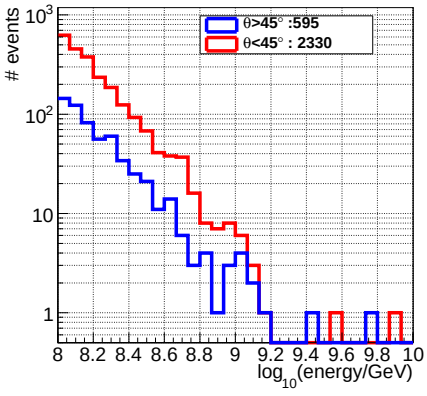

(b) Reconstructed energy distributions for KASCADE-Grande triggered events

Figure 4.9.: Reconstructed energy distribution from regular showers (red histogram) and showers with $\theta \geq 45^\circ$ (blue histogram).

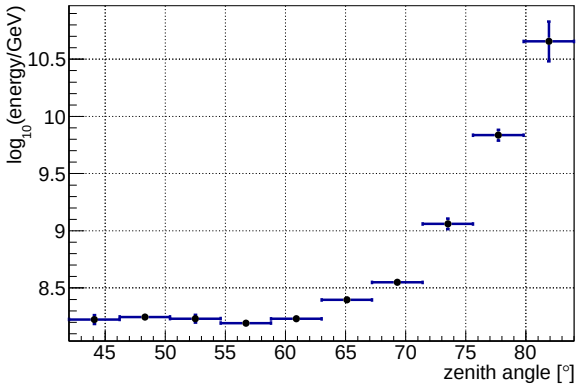

Figure 4.10.: Reconstructed energy distribution from showers with $\theta \geq 45^\circ$ plotted over the zenith angle for the KASCADE preselection.

4.3. Conclusion

In this chapter the preselected data samples have been discussed and the selection has been successfully checked for consistency. The functionality of LOPES 3D is clearly proven by several cross-checks like for example the event rates and comparing measured data with the $\vec{v} \times \vec{B}$-model. A dynamic criterion to define a signal-to-noise-ratio cut on the CC-beam was derived.
For the KASCADE-inclined data set an overestimation of the energy for large

zenith angles was found. The sensitivity for KASCADE was estimated up to zenith angles $\theta \approx 80^{\circ}$ whereas the Grande extension is sensitive up to $\theta \approx 54^{\circ}$. During the life time of LOPES 3D (May 2010 to January 2013) LOPES was running only 10 months with a high event rate because since March 2011 the background increased.

CHAPTER 5

Vectorial Treatment of the Antenna Gain

When analysing the radio emission from extensive air showers with high precision it is indispensable to understand every single component of the data acquisition in detail. One very crucial point is the gain pattern of a radio antenna. The gain pattern describes the sensitivity of the antenna and mainly depends on:

- the arrival direction of the signal,
- the frequency spectrum of the signal,
- the polarization of the signal.

Further changes in the gain pattern come along with changing ground or weather conditions. Metal parts near the antenna have an influence as well. Applying the vectorial gain and reconstructing the initial electric field vector will be explained in detail in the following.

5.1. Antenna Gain

The gain of a radio antenna is a complex vectorial quantity, incorporating the attenuation (real) and dispersion (imaginary) of the antenna, that translates the measured electric field strength to a voltage at the antenna foot-point according to equation 5.1.

$$S_{\text{ant}} = \vec{E} \cdot \vec{G}(f, \theta, \phi) \tag{5.1}$$

with S_{ant} being the voltage at the antenna foot-point, $\vec{E}$ the incoming electric field vector, and the vector $\vec{G}(f, \theta, \phi)$, the complex gain of the antenna as a function of frequency f, zenith θ and azimuth ϕ of the incoming signal. This implies that a measurement with only one antenna leads to a significant information loss, as the measured electric field vector is recorded as a scalar. Several different electric field vectors can result in the same measured scalar value.
The following considerations are done in the plane perpendicular to the incoming direction of the radio wave. In this plane the antenna gain and the electric field vector reduce to two components. This consideration is motivated in more detail in the following section (5.2) of this chapter. All vectors $\vec{E}_t$ that are described by the conditions given in equation 5.2 will result in the same measured scalar value c, with $\vec{G}$ being the constant gain.

$$\vec{E}_t \cdot \vec{G} = G_{ze} \cdot E_{t,1} + G_{az} \cdot E_{t,2} = c \Rightarrow E_{t,1} = \frac{c}{G_{ze}} - \frac{G_{az} \cdot E_{t,2}}{G_{ze}} \tag{5.2}$$

For this consideration the gain $\vec{G}$ has no direction dependence since all incoming electric field vectors are assumed to arrive from the same direction, therefore the gain is constant. Thus, with a measurement with only one antenna, the electric field vector cannot be reconstructed, furthermore not even one component can be reconstructed correctly. With the former configurations of LOPES, LOPES 10 and LOPES 30 only east-west aligned inverted v-shape dipole antennas were used. Thus, the only way to determine the east-west electric field vector component is to use a simplification of equation 5.1 which then leads to

$$S_{\text{ant}} = |\vec{E}|_{\text{ew}} \cdot |\vec{G}(f, \theta, \phi)| \tag{5.3}$$

which is used to approximate the east-west component $|\vec{E}|_{\text{ew}}$ according to

$$|\vec{E}|_{\text{ew}} = \frac{S_{\text{ant}}}{|\vec{G}(f, \theta, \phi)|} \tag{5.4}$$

This approximation is correct if the measured signal is purely east-west polarized. All LOPES analysis done so far have to use this approximation. The quality of this approximation in general is currently under investigation (Link, 2014) and not covered within the scope of this thesis.

5.2. Application of the Antenna Gain

Although the incoming electric field is a vector, when measuring with only one antenna, it is only possible to measure scalars, where the relation of the electric

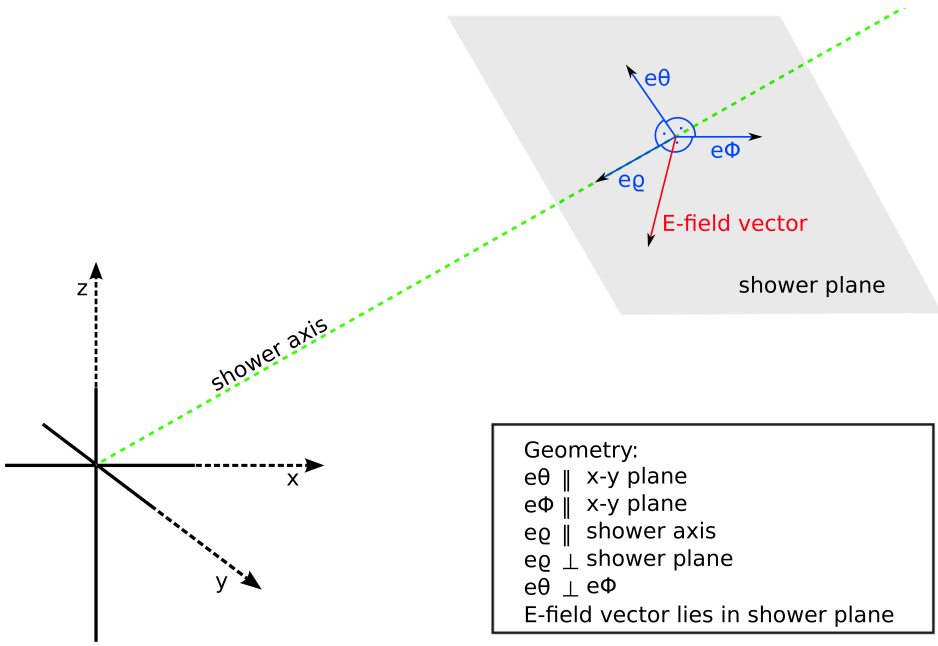

Figure 5.1.: Sketch of the electric field vector lying in the shower plane (plane perpendicular to the shower axis) in comparison to the fixed coordinate system of the antenna. e_Θ, e_ϕ and e_σ are unit vectors of the shower coordinate system.

field to the scalar depends on the antenna gain. This implies that in order to reconstruct the complete vector, three scalars need to be measured. However since the radio emission from cosmic ray induced air showers is a transverse electromagnetic wave, the electric field vector in the shower plane reduces to two components, see also figure 5.1. Also the antenna gain in shower coordinates reduces to two components, $G(f,\theta,\phi)^{\mathsf{az}}$ and $G(f,\theta,\phi)^{\mathsf{ze}}$ according to equation 5.5

$$\vec{G}(f,\theta,\phi) = G(f,\theta,\phi)^{\mathsf{az}} \cdot \hat{e}_\phi + G(f,\theta,\phi)^{\mathsf{ze}} \cdot \hat{e}_\theta \tag{5.5}$$

Thus the electric field vector can be calculated completely when measuring only two signals, if the arrival direction is known. From the two measured signals S_{ant1} and S_{ant2}

$$S_{\mathsf{ant1}} = \vec{E} \cdot \vec{G}(f,\theta,\phi)_{\mathsf{ant1}}, \tag{5.6}$$

$$S_{\mathsf{ant2}} = \vec{E} \cdot \vec{G}(f,\theta,\phi)_{\mathsf{ant2}} \tag{5.7}$$

the two components of the electric field vector in the shower plane E_θ and E_ϕ can be calculated:

$$E_\theta = \frac{S_{\mathsf{ant2}} \cdot G(f,\theta,\phi)^{\mathsf{az}}_{\mathsf{ant1}} - S_{\mathsf{ant1}} \cdot G(f,\theta,\phi)^{\mathsf{az}}_{\mathsf{ant2}}}{G(f,\theta,\phi)^{\mathsf{az}}_{\mathsf{ant1}} \cdot G(f,\theta,\phi)^{\mathsf{ze}}_{\mathsf{ant2}} - G(f,\theta,\phi)^{\mathsf{az}}_{\mathsf{ant2}} \cdot G(f,\theta,\phi)^{\mathsf{ze}}_{\mathsf{ant1}}}, \tag{5.8}$$

$$E_\phi = \frac{S_{\mathsf{ant1}} \cdot G(f,\theta,\phi)^{\mathsf{ze}}_{\mathsf{ant2}} - S_{\mathsf{ant2}} \cdot G(f,\theta,\phi)^{\mathsf{ze}}_{\mathsf{ant1}}}{G(f,\theta,\phi)^{\mathsf{az}}_{\mathsf{ant1}} \cdot G(f,\theta,\phi)^{\mathsf{ze}}_{\mathsf{ant2}} - G(f,\theta,\phi)^{\mathsf{az}}_{\mathsf{ant2}} \cdot G(f,\theta,\phi)^{\mathsf{ze}}_{\mathsf{ant1}}}. \tag{5.9}$$

This reconstructed electric field vector then can be rotated to a fixed coordinate system, such as North, West, Vertical up, to compare it with other measured vectors. The reconstruction algorithm was developed in cooperation, and thus in AERA the reconstruction of the electric field vector is performed in the same way (Fuchs, 2012b).

5.2.1. Vectorial Gain Application on LOPES 30 pol Data

LOPES 30 pol was the setup of LOPES that had the longest operation time. In this setup, LOPES consisted of 10 east-west aligned antennas, 10 north-south aligned antennas and five antenna stations that had both east-west and north-south aligned antennas. To the signal recorded in these five antenna stations the vectorial gain treatment can be applied. In order to study the benefits of the vectorial gain over the simplified gain treatment, the following analysis was conducted: First the gain was treated according to the simplification described in equations 5.3 and 5.4, and then the cross-correlation beam (CC-beam) height is checked and the event is considered as successfully reconstructed if the signal-to-noise ratio of the CC-beam is above a chosen threshold. Details on the threshold determination can be found in chapter 4 of this work. The ratio of reconstructed events from KASCADE and LOPES using this condition is shown in figure 5.2. Second, the reconstruction is repeated for the vectorial gain treatment according to equations 5.8 and 5.9. The reconstruction efficiency using the new gain treatment is improved, see figure 5.2. To have a fair comparison the reconstruction was performed for the north-south and east-west component separately in both cases. An event is considered as successfully reconstructed if the CC-beam in at least one components is above the chosen threshold of $MPV + 2 \cdot \sigma$. This ensures that only the new gain treatment affects the results presented in figure 5.2.

Vertical Component Reconstruction

Another advantage of the vectorial gain treatment is the possibility to reconstruct the full electric field vector, according to equations 5.8 and 5.9. For the subset of

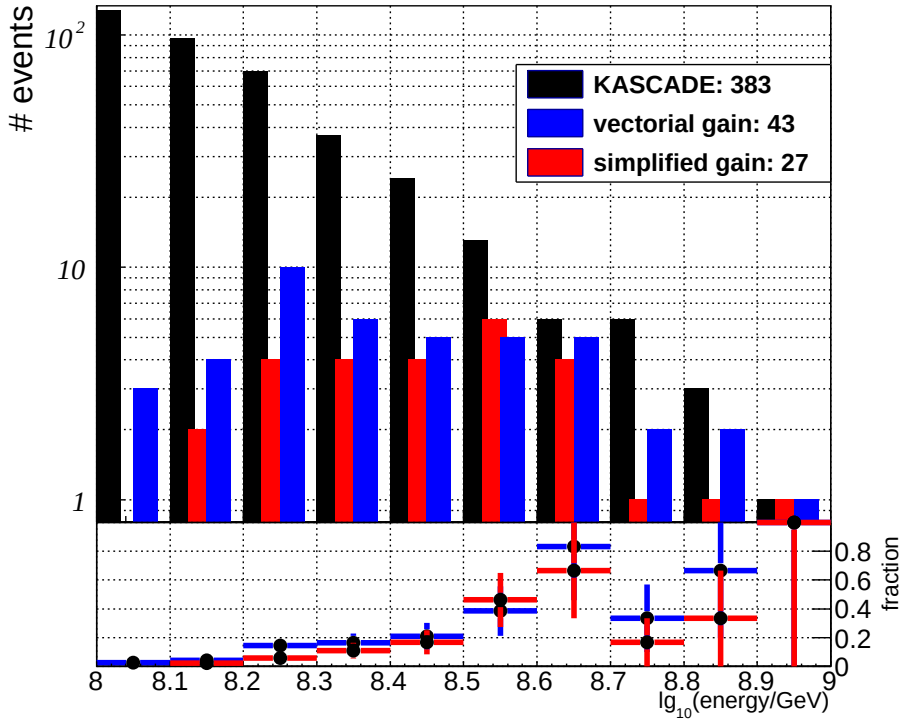

Figure 5.2.: Histogram of the events triggered and reconstructed by KASCADE (black). The events reconstructed with the 5 dual-polarized antennas of LOPES 30 pol using the simplified (red) and the vectorial gain (blue) treatment and the corresponding fractions of triggered and reconstructed events (blue and red points). The horizontal error bars are the bin width and the vertical error bars represent the uncertainties assuming a binomial distribution.

the five double-polarized antennas this reconstruction has been performed, and information not accessible before can now be accessed. In figure 5.3, reconstructed traces of the vertical component of the electric field vector are shown. These signals were reconstructed using the data measured with horizontally aligned antennas only. A coherent pulse at all stations can be observed at the expected time. The reconstruction of the vertical component with horizontal antennas can only be done as long as most of the signal is recorded by these horizontal antennas. The more signal is in the vertical component the worse it can be reconstructed using the horizontal antennas. On average this is the case the more inclined an air shower arrives.

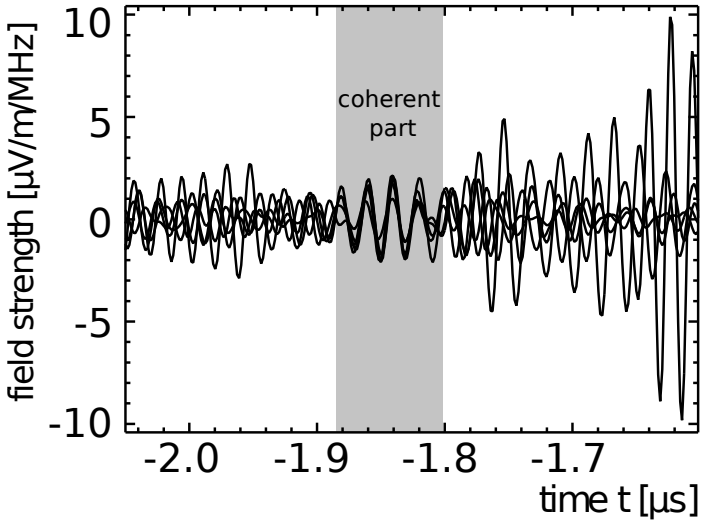

Figure 5.3.: Traces of the vertical component reconstructed from measurements with only horizontally aligned antennas.

5.3. Vectorial Gain Application on LOPES 3D Data

The correct gain application was also probed with the horizontally aligned antennas of LOPES 3D. A discussion of the benefits of an additional measurement with vertically aligned antennas is given in chapter 8. To check the benefits of the vectorial gain treatment the same analysis like for the LOPES 30 pol data was conducted. In figure 5.4 the measured event rates can be seen. As expected, also in the LOPES 3D data the reconstruction efficiency using the new gain treatment slightly improved. But not all events reconstructed using the total gain approximation are also reconstructed when analysing them using the vectorial gain. In fact, the more aligned the electric field vector is with an antenna, the better the simple gain approximation works. LOPES 3D was operated just at the beginning of the energy threshold for radio detection of extensive air showers. Thus an approximation like the simple gain approximation can result in a reconstructed event which is not reconstructible with the correct application of the gain.

5.4. Conclusion

In this chapter the correct application of the antenna gain was derived and was successfully demonstrated on a suitable selection of LOPES 30 pol and LOPES

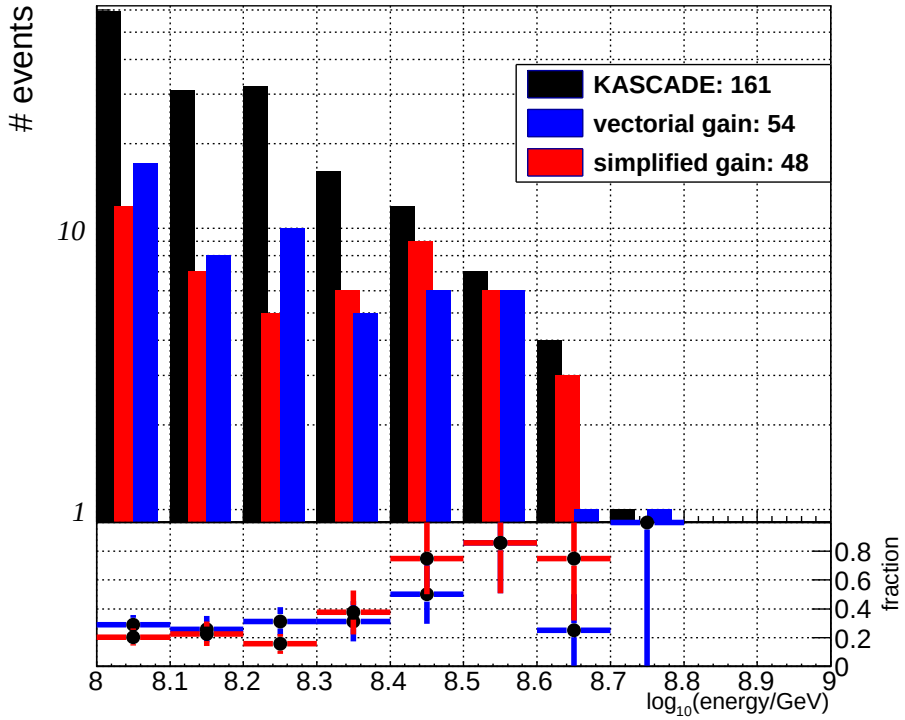

Figure 5.4.: Histogram of the events triggered and reconstructed by KASCADE (black). The events reconstructed by LOPES 3D using the simplified (red) and the vectorial gain (blue) treatment and the corresponding ratio of triggered and reconstructed events (blue and red points). The horizontal error bars are the bin width and the vertical error bars represent the uncertainties assuming a binomial distribution.

3D data. A correct reconstruction of the electric field vector is only possible if at least two antennas measure the signal in spatial and temporal coincidence. With this, for the first time, it is possible to reconstruct the electric field vector and thus perform for example polarization studies. Furthermore it was demonstrated that the correct antenna gain treatment increases the rate of reconstructible events.

CHAPTER 6

Vectorial Beamforming

Within this thesis the beamforming procedure was improved to work on the complete reconstructed electric field vector (see chapter 5 for the reconstruction of the electric field vector.). In the following vectorial beamforming is discussed and compared with the former beamforming procedure that uses only single components. The CC-beamforming procedure was tested on the subset of data which was recorded before the increase in background noise described in chapter 4. By calculating the CC-beam, LOPES is used as a digital radio interferometer, since the CC-beam is sensitive not only to the amplitude but also to the phase of the radio signal. The beamforming increases the signal-to-noise ratio of the measured radio pulse significantly. It is the first step of any analysis performed with LOPES. This advanced technique helps to significantly reduce the detection threshold and with this it is possible to detect the radio emission from cosmic ray induced air showers in a noisy environment as it is the case at the LOPES site.

6.1. Beamforming on Single Components

During beamforming the time traces of the single antennas are shifted with respect to each other. This is done to superimpose the pulses in the single traces in order to gain the highest sensitivity in the source direction. The radio pulses in single traces are in phase, thus in the CC-beam they correlate, whereas noise with uncorrelated phases cancels out. To form the power beam (P-beam) the squares of the traces are added up. The power beam is a measure of the received power

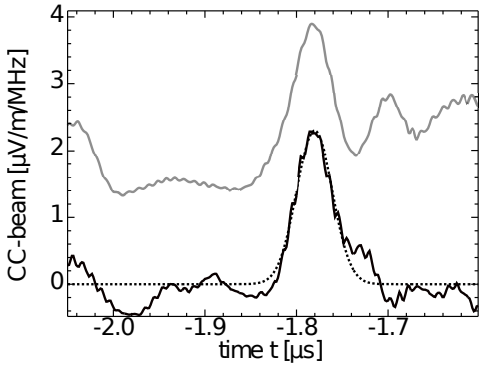

(a) CC-beam for the east-west orientation

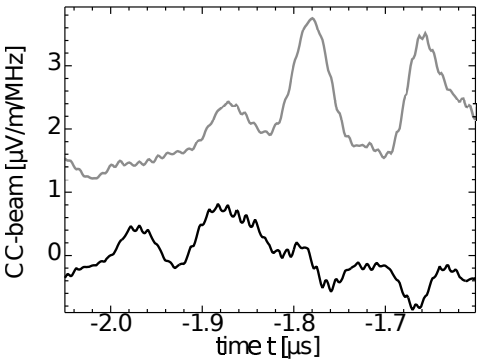

(b) CC-beam for the north-south orientation

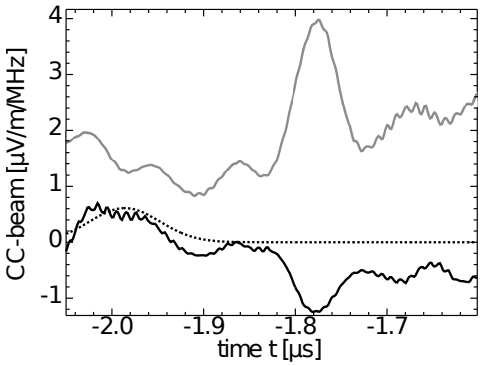

(c) CC-beam for the vertical orientation

Figure 6.1.: CC-beam calculated on an example event with the vectorial gain treatment including phases, but for each orientation separately. The CC-beam is shown as solid black line, the power-beam as grey line and the Gaussian fit to the CC-beam, if converged, is shown as dashed black line.

whereas the CC-beam is a measure of the coherent power. So far the beamforming was done separately for signals measured with the east-west aligned antennas and north-south aligned antennas, cf. equation 6.1 for the CC-beam calculation and equation 6.2 for the P-beam calculation (Horneffer et al., 2006).

$$f_{CC}(t) = \pm\sqrt{\left|\frac{1}{N}\sum_{i=1}^{N-1}\sum_{i>j}^{N}\hat{e}_i(t)\cdot\hat{e}_j(t)\right|} \tag{6.1}$$

$$f_P(t) = \sqrt{\left|\frac{1}{N}\sum_{i=1}^{N}\hat{e}_i^2(t)\right|} \tag{6.2}$$

with $\hat{e}$ being one component of the measured electric fieldvector, t the time and the number of recorded traces used for the beamforming N. In figure 6.1, the

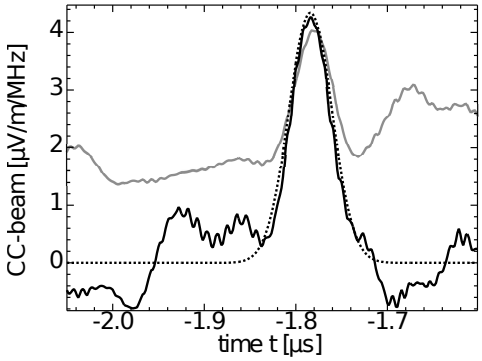

Figure 6.2.: CC-beam calculated vectorially combining information from all three orientations of the electric field with the vectorial gain treatment. The CC-beam is shown as solid black line, the power-beam as grey line and the Gaussian fit to the CC-beam as dashed black line.

CC-beams and Power-beams calculated for each component separately are shown.

Forming the CC-beam helps identifying even signals that are at the noise level in individual antennas (Huege et al., 2012). Thus, on the one hand, it is desirable to have as many signal traces as possible going in the CC-beam calculation. On the other hand, if a trace has no information on the signal and only contains noise, it will significantly harm the signal-to-noise ratio of the CC-beam.

6.2. Vectorial Beamforming

Within the scope of this thesis the CC-beam calculation has been improved to work on the complete electric field vector[1]. This is the first time that vectorial beamforming has been applied to identify air shower radio emission. Working on the full vector uses all the information available for the reconstruction. In former analysis only one component of the electric field vector was used. Depending on geometry and received signal in the single polarizations, this can increase the reconstruction efficiency of air showers. In figure 6.1, a CC-beam is shown which was calculated with the vectorial gain treatment including phases, but reconstructed for every component of the electric field vector separately. A clear signal is only visible in east-west, but in the power beams, for all three components of the electric field vector a peak can be seen. If there is a peak in the power but not in the CC-beam this means that the measured signal is uncorrelated in the different

[1]The vectorial beamforming was made available publicly as open-source code which can be found in http://usg.lofar.org/svn/code/branches/cr-tools-stable

antennas and likely not originating from the air shower. Thus, it is important to use the CC-beam to identify air showers, since the RFI (radio frequency interference) introduced by KASCADE has the same shape in the Power-beam as air shower signals, see figure 6.1 left (Power-beam for the north-south component), second peak. Radio emission from air showers is coherent which leads to a high CC-beam and a high Power-beam, whereas noise in most cases only causes a high Power-beam. However, for the beamforming results shown in figure 6.1 the present background noise destroyed the coherence of the signal in the north-south and vertical component.
The CC-beam shown in figure 6.2 is calculated vectorially combining information from all three components of the electric field according to equation 6.3:

$$F_{CC}(t) = \sqrt{\left| \frac{1}{N} \sum_{i=1}^{N-1} \sum_{i>j}^{N} \vec{E}_i(t) \cdot \vec{E}_j(t) \right|} \tag{6.3}$$

with the complete electric field vector $\vec{E}$, the time t and the number of vectors used for the calculation of the CC-beam N.The CC-beam has a higher peak value but approximately the same noise level as the CC-beams calculated in single polarizations as shown in figure 6.1. In addition, the CC-beam has the same height as the Power-beam which means that nearly all power received was correlated (coming from the air shower). The improvement in signal-to-noise ratio height is only due to the vectorial calculation and not because of the advanced gain treatment, since the advanced gain treatment was applied during both beamforming procedures, i.e. vectorial and classic. This demonstrates that the reconstruction can be improved with vectorial beamforming, as long as each single polarization measurement at least contains some information on the signal.

6.2.1. Drawbacks of Vectorial Beamforming

Calculating the CC-beam of the complete electric field vector can also have negative impact on the result. The CC-beamforming is very sensitive to signals correlated in phase and amplitude. Depending on shower geometry, the radio emission from air showers is not visible in all three polarizations, see also figure 6.3. Here, the threshold signal (i.e. amplitude of the electric field vector) received in the weakest component according to an analytical model[2] is shown in dependence of arrival direction. For the standard LOPES geometries (zenith angle $\theta \leq 45^\circ$), less than 10% of the signal is expected in the component of the electric

[2]For the model we assume a 93% $\vec{v} \times \vec{B} \sin(\alpha)$-dependence plus 7% charge excess, with $\alpha =$ angle between shower axis and Earth's magnetic field. The motivation for this choice is given in chapter 7.

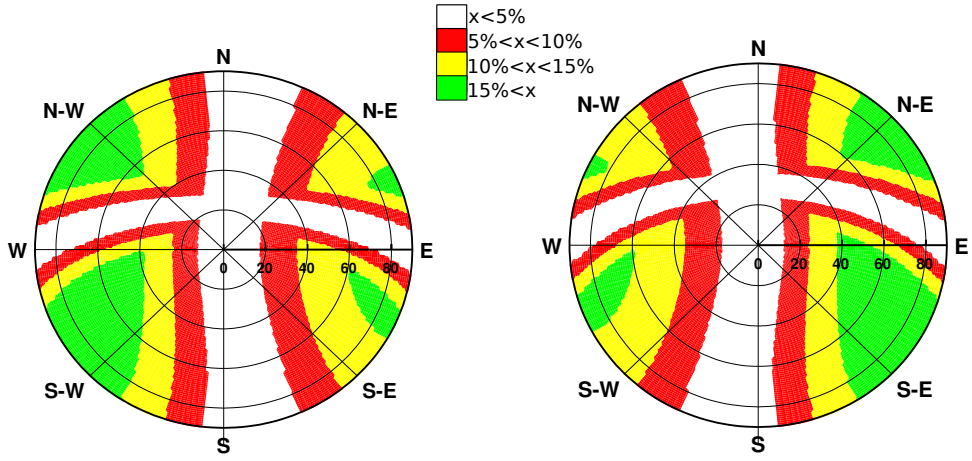

Figure 6.3.: Skymap of the predicted received relative power in the weakest component of the electric field vector. In the white region less than 5% are received in the red region between 5% and 10% are received in the yellow region between 10% and 15% are received and in the green region more than 15% are received. This map was calculated according to an analytical emission model, assuming a 93% $(\vec{v} \times \vec{B}\sin(\alpha))$-dependence + 7% charge excess for the two extreme cases, i.e. all antennas in the west of the shower core (left) and all antennas in the east of the shower core (right).

field vector with the lowest signal. Although noise in most cases cancels out when calculating the CC-beam, taking into account traces with no information should be avoided since the CC-beam is normalized to the number of traces. This means that even with the advanced technique of vectorial beamforming pure background traces harm the analysis.
It was found that for geometries where most of the signal is present in one component of the electric field vector, beamforming on single components separately is the best way to analyse these kind of air showers. In case of LOPES, most showers are not detected in all three components. The main reasons for this are the high background level at the LOPES site and the trigger of LOPES being sensitive to relatively low energies. Thus, the model calculation for the sensitive region shown in figure 6.3 gives a good estimation for which arrival directions vectorial or classic beamforming is preferable.

6.2.2. Optimal Conditions for Vectorial Beamforming

The vectorial beamforming has potential when it comes to higher energies and radio quiet areas. Under these conditions it is more likely to have measured

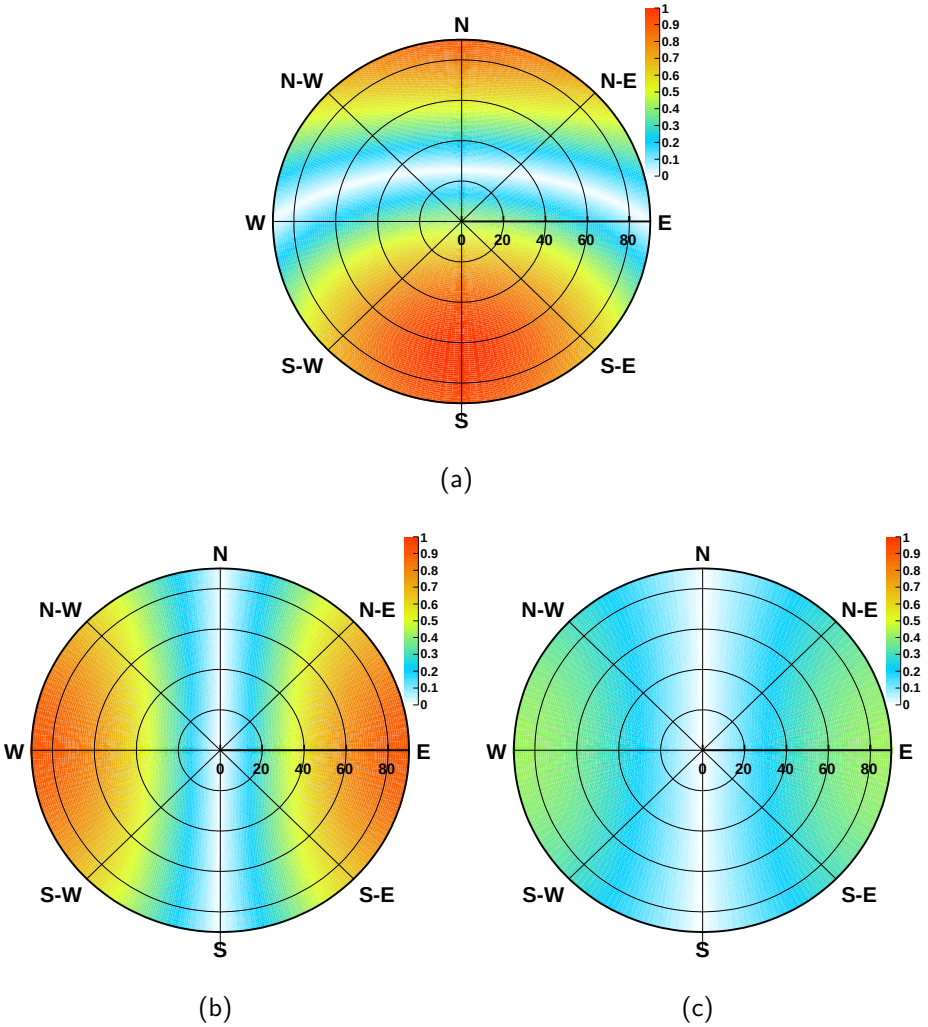

(a)

(b)

(c)

Figure 6.4.: Prediction of the relative signal strength for the dominant emission mechanism, the $\vec{v} \times \vec{B}$-model for the east-west (a), north-south (b) and vertical (c) component of the normalized emission vector at the location of LOPES with $B_{az} = 0°$ and $B_{ze} = 64.4°$ for the geomagnetic field in Karlsruhe (Barton, 1997).

coherent signal in each of the three recorded traces by one tripole antenna. If in this conditions vectorial or classic beamforming is still needed or brings benefits is still an open question. With LOPES, which is located in an industrial-like and radio-loud area, the power of vectorial beamforming was demonstrated exemplarily (cf. figures 6.1 and 6.2). In figures 6.4 and 6.5, the relative strength of the radio emission of the dominant mechanism ($\vec{v} \times \vec{B}$) and the main second order emission mechanism (charge excess) are shown. For the charge excess, the maximum

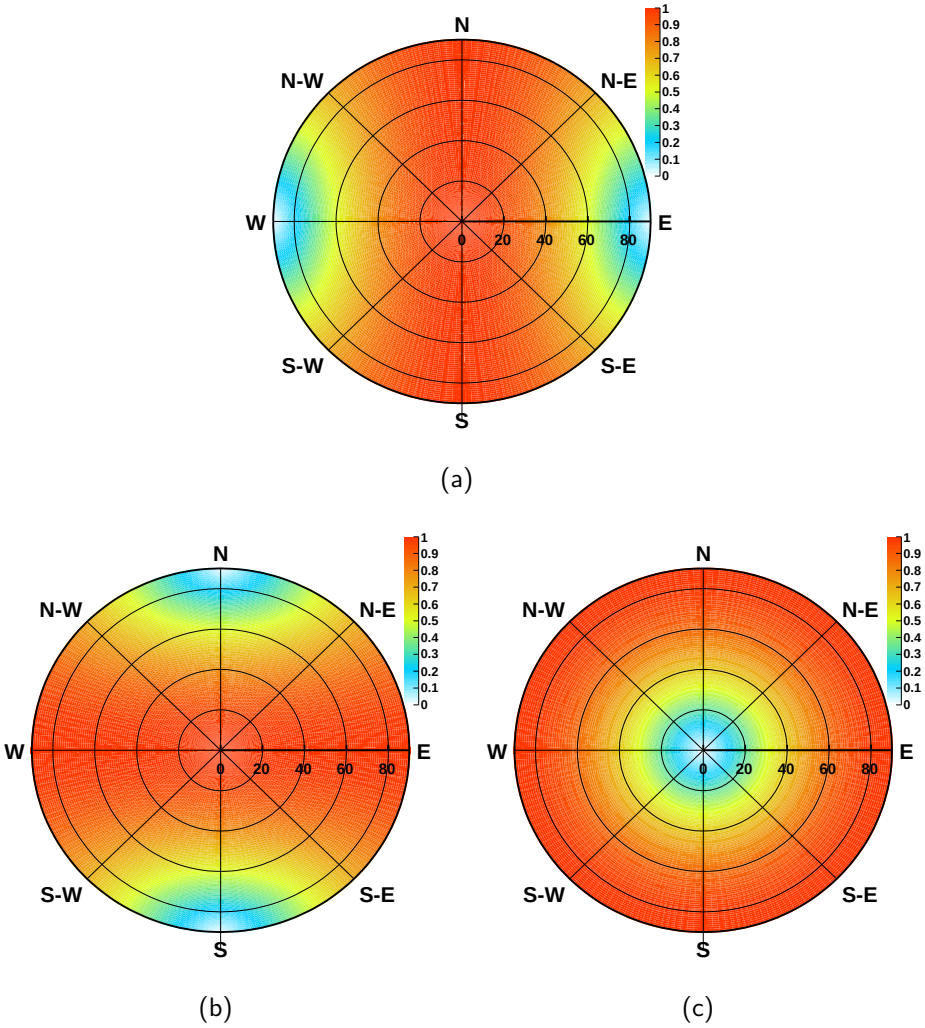

(a)

(b)

(c)

Figure 6.5.: Prediction of the relative signal strength for the second order mechanism charge excess for the east-west (a), north-south (b) and vertical (c) component of the normalized emission vector. Note that this emission represents on average 7% of the radio signal.

predicted relative field strength is shown. This field strength varies with the observer position relative to the shower core. However, since most of the events are contained, i.e have their shower core inside the array, at least one observer position with maximum predicted strength can be found. Nevertheless the regions shown in figure 6.3 where no signal is predicted are valid for all antennas in the array.

As soon as the energy of the air shower is high enough that even the second order effect generates detectable radio emission, the vectorial beamforming is applicable

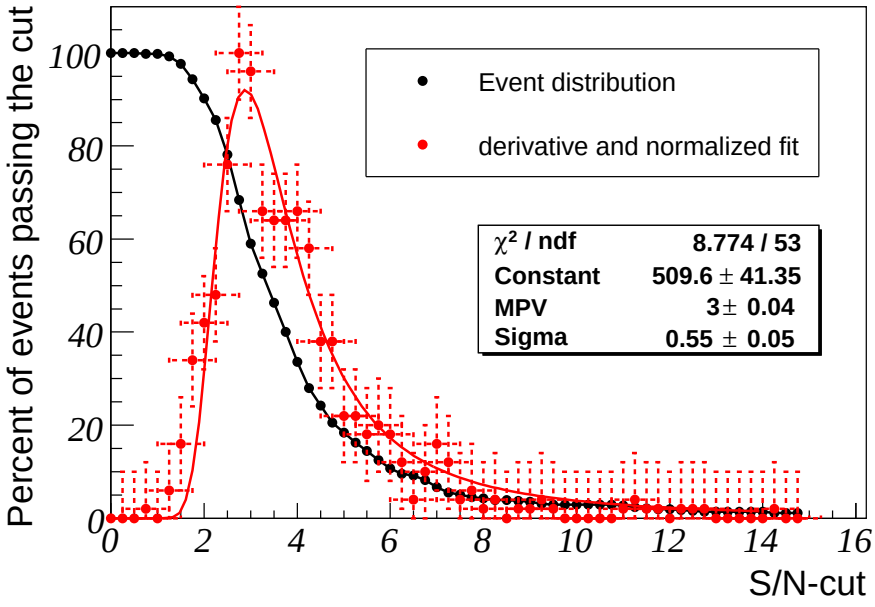

Figure 6.6.: Fraction of events passing a certain SNR-cut plotted as a function of the cut value (black dots and line) for KASCADE triggered events using the vectorial beamforming, the absolute value of the derivative of this distribution normalized to 100 (red dots) and a Landau distribution (red line) fitted to it. X-error bars are the two times the bin width, y-error bars assumed to be constant and 10% of the maximum fraction.

for any direction on the sky. Thus vectorial beamforming is a promising tool to improve the air shower parameter reconstruction when it comes to radio detection of air showers at highest energies.

6.2.3. Vectorial Beamforming on Data

To check the benefits of vectorial beamforming, the procedure was applied to the reconstruction of LOPES data. The selection criterion was calculated as described in chapter 4 but with radio events that were reconstructed using vectorial beamforming, see also figure 6.6. It can be seen that for the vectorial CC-beam the most probable value is 3 and sigma is ≈ 0.5. This is an improvement compared to the non-vectorial beamforming ($MPV \approx 3.75$ and $\sigma \approx 0.65$) and expected since in the vectorial CC-beam calculation the orientation of the electric field vector is taken into account and not only the amplitude and phase like in the classic beamforming. This gives noise a higher probability to cancel out. The amount and ratio of reconstructed events using the vectorial beamforming are shown in

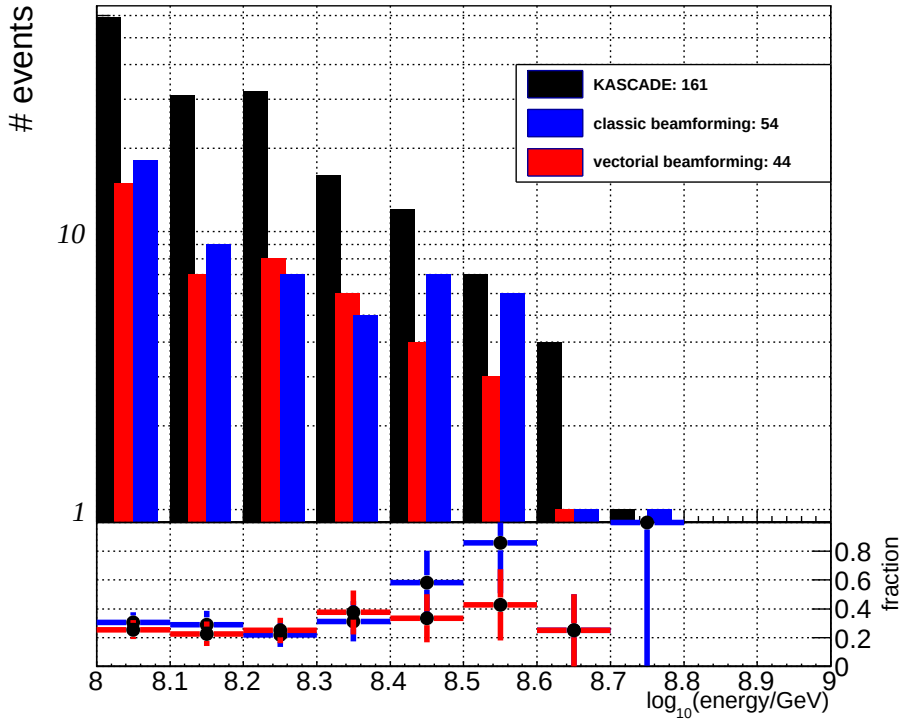

Figure 6.7.: Rate of reconstructed events using vectorial beamforming compared to the former classic beamforming (i.e. beamforming on single polarizations).

table 8.1 and plotted for the normal-KASCADE selection in figure 6.7 for vectorial and classic CC-beamforming. Fewer events can be reconstructed when applying vectorial beamforming which was expected since this selection contains showers with geometries for which the vectorial beamforming is less effective. Nevertheless it has to be considered that if an air shower has been successfully reconstructed using vectorial beamforming, this means that the air shower signal was detected in all three components of the electric field. For the comparison shown in figure 6.7, for the classic beamforming events are counted that could be reconstructed in at least one component of the electric field vector.
When only looking at events that could be reconstructed in all components of the electric field vector (i.e. detected in east-west AND north-south AND vertical) the number of events for the classic CC-beamforming drops to 15. With this condition more events could be reconstructed using the vectorial beamforming as expected since more information is combined during the analysis.

6.3. Conclusion

In this chapter vectorial beamforming was introduced, which can significantly improve the analysis by increasing the signal-to-noise ratio of the CC-beam. Nevertheless, calculating the CC-beam vectorially can also harm the analysis. Depending on the distribution of the air shower radio signal on the single components either classic or vectorial beamforming is applicable. The distribution of the signal is depending on the arrival direction, thus a model calculation for the effective and ineffective regions for vectorial beamforming was given. However, an air shower reconstructed with the vectorial beamforming contains the maximum information since it has a detected signal in all three components of the electric field vector. Thus the ideal approach is to try first a vectorial beamforming and if this fails try beamforming on single components.

CHAPTER 7

Analysing the Polarization of the LOPES 3D-Recorded electric field Vector

With the vectorial gain treatment and the detailed calibration, LOPES 3D is a well understood experiment for air shower detection via digital radio interferometry. In this chapter the typical analysis flow for LOPES is briefly described.
For the first time, the analysis done with LOPES recorded data can be based on the electric field vector due to the vectorial gain. An analysis based on these single reconstructed electric field vectors to confirm a second order emission mechanism is developed and discussed. A discriminating variable is derived which describes the charge excess contribution in each measured electric field vector.

7.1. The Analysis Chain for LOPES

The reconstruction of air shower parameters with LOPES is done in several steps that are explained in detail in the following. A flowchart of the typical analysis procedure is shown in figure 7.1. Here input from external sources is highlighted in yellow, the beamforming and simplex-fit procedure in green, the data treatment in blue and the LOPES data file is shown in red. First the recorded data are transformed to the frequency domain via FFT (fast Fourier transform), this step is not shown in figure 7.1. Then the data are corrected for the delay, the dispersion and the attenuation in the electronics, c.f. chapter 3. This is done by modifying the amplitude and phase of the Fourier transformed data. Then the

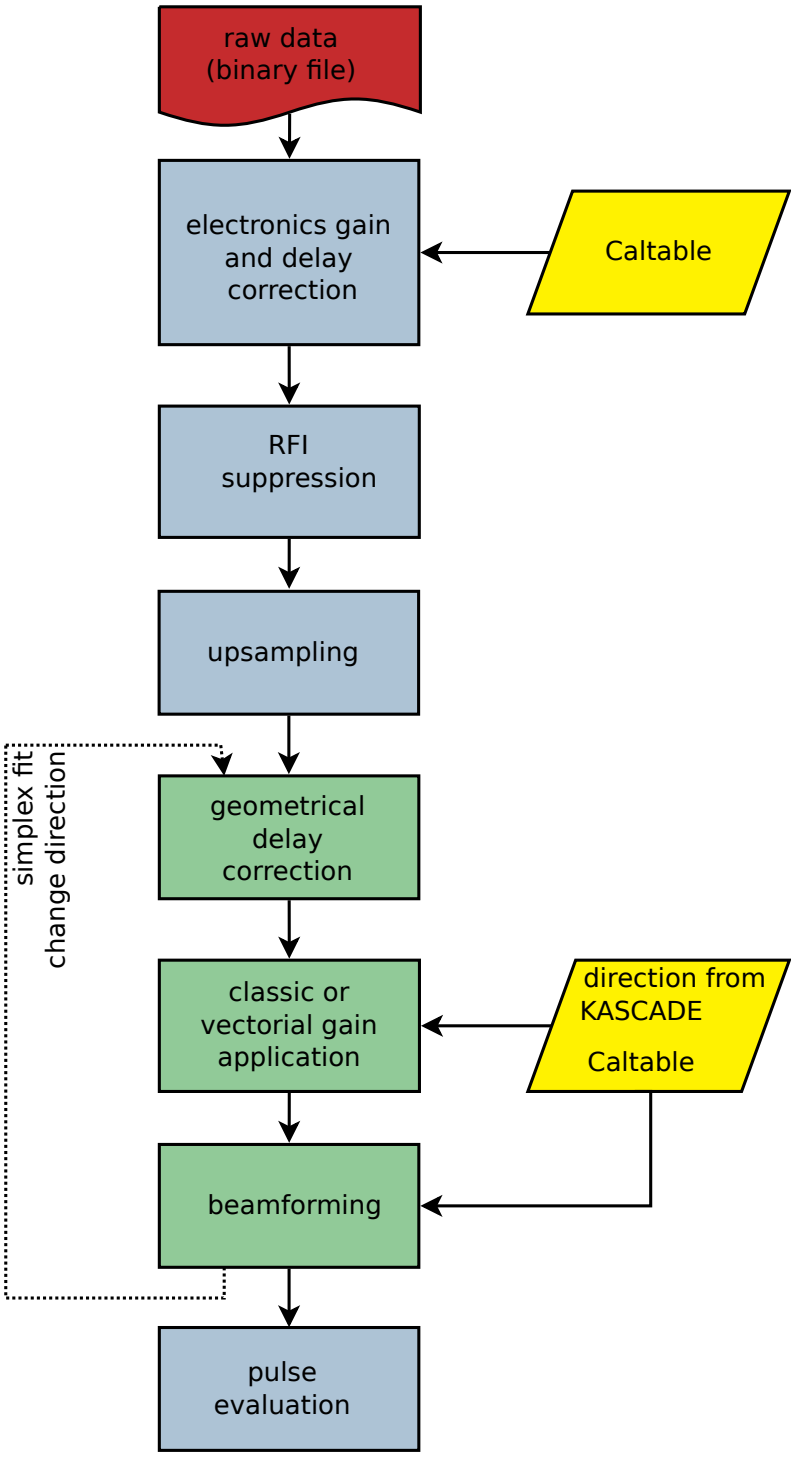

Figure 7.1.: Flow chart of the typical beamforming procedure as performed in the LOPES analysis software.

data are digitally filtered to the designed bandwidth. This is needed since the filter modules used in LOPES 3D are not all of the same type and have different effective bandwidths, by digital filtering this is compensated for. After this, the narrow-band RFI (radio frequency interference) peaks are cut out, this is done by simply cutting all narrow band peaks out in the Fourier transformed data[1]. With this the noise is significantly reduced but the air shower radio signal is not affected (Luis, P. Facal San, 2013). This step is needed to significantly increase the signal-to-noise ratio and thus the efficiency of air-shower detection. Then, if desired, the data are upsampled. In this procedure the data points that are missing due to the limited sampling rate are reconstructed. If the sampling frequency is twice the bandwidth of the sampled signal, no information gets lost during the digitalization according to Nyquist (1928). For the upsampling several methods can be used. In LOPES zero-padding is applied. For further details we refer to Bracewell (1986). After this, the beamforming procedure is performed. This is highlighted in green in figure 7.1. The initial direction for the beamforming is taken from the KASCADE-Grande reconstruction, the distance is set to a default value of $2500\,\mathrm{m}$. First the antenna gain (c.f. chapter 5.1) and the geometric delay[2] are incorporated. After this the CC-beam (c.f. chapter 6) is calculated for all points lying on a defined grid around the direction given by KASCADE-Grande. Then a simplex fit is performed starting with that point of the grid that had the highest CC-beam value. During the simplex fit the distance and the arrival direction are varied until the highest CC-beam value is found. After this several parameters like the CC-beam height, the signal height in single antennas, the arrival direction etc. are calculated and saved in a ROOT file to be further processed. In this step plots of the single events, like e.g. CC-beam, traces, spectra, lateral distributions etc. can be generated. The lateral distributions are calculated in shower coordinates and show the field strength as function of distance to the shower axis. The uncertainties are calculated the following way: A 5% calibration uncertainty is assumed and additionally the noise in the single antenna traces is calculated and added. Further details on the noise calculation can be found in (Schröder, 2011). Based on the generated ROOT files the radio data can be further processed for the desired analysis. Examples of single event plots are shown in figures 7.2, 7.3 and the lateral distribution functions are shown in figure 7.4.

The measured and simulated calibration values needed to reconstruct the electric field correctly are stored in a digital binary format, the so-called "CalTable". In the "CalTable" the following quantities are stored:

[1] Radio emission from cosmic ray air showers is broadband, thus narrow band peaks can only be caused by noise and are cut out.

[2] The geometric delay is the difference in the travel time of the radio signals caused by the different distances between antennas and the source. Consequently the geometric delay depends on the radio wave front.

- the simulated gain patterns and phases of the antennas
- the positions of the tripole antennas
- the measured delay, amplification and dispersion of each channel
- the measured reference phase for the beacon correction of each channel
- the combination of three channels to one tripole

7.1.1. The Vectorial Lateral Distribution Function

Within this thesis the lateral distribution function was updated to work on the complete electric field vector. The lateral distribution function (ldf) describes the measured radio field strength as a function of distance to the shower axis. In principle this is a 2-dimensional function, but since at LOPES too few antennas are available, a 1-dimensional dependency is used instead (Apel et al., submitted 2014b). This function carries information on both, the mass and the energy of the primary particle. The mass of the primary particle correlates with the atmospheric depth at which the shower has its maximum amount of particles X_{max}. The larger cross-section for heavier nuclei leads to a faster development of the air shower, thus to a larger X_{max}. This faster development causes the radio pulse to be emitted at a larger distance to the array which then leads to a flatter lateral distribution and vice versa for light nuclei (Apel et al., submitted 2014a). So far the ldf was calculated for the signal measured in the east-west or north-south separately. With LOPES 3D (not yet using the vertically aligned antennas) the full electric field vector can be reconstructed and with this the lateral distribution function can be improved significantly. The reconstructed electric field vector is rotated to shower coordinates and the length of this vector is plotted over the distance to shower axis. With this for the first time in LOPES the complete electric field vector is used in a lateral distribution function. When rotating the measured electric field vector to shower coordinates, the noise can be estimated for the exact time of the measurement. The part of the measured vector perpendicular to the shower plane is mainly caused by noise and is therefore a very good estimator for the noise level at the time of the measurement. In figure 7.5 an example of such an ldf is shown. On top the 1-dimensional ldf as described above can be seen, here the error bars represent the part of the electric field vector perpendicular to the shower plane. On the bottom the single electric field vectors are plotted starting at the antenna positions in shower coordinates, the red arrow starting at the star is the predicted emission vector according to the $\vec{v}\times\vec{B}$-model. In this presentation the field strength and the orientation of the measured vectors can be observed in the same plot for the fist time in LOPES.

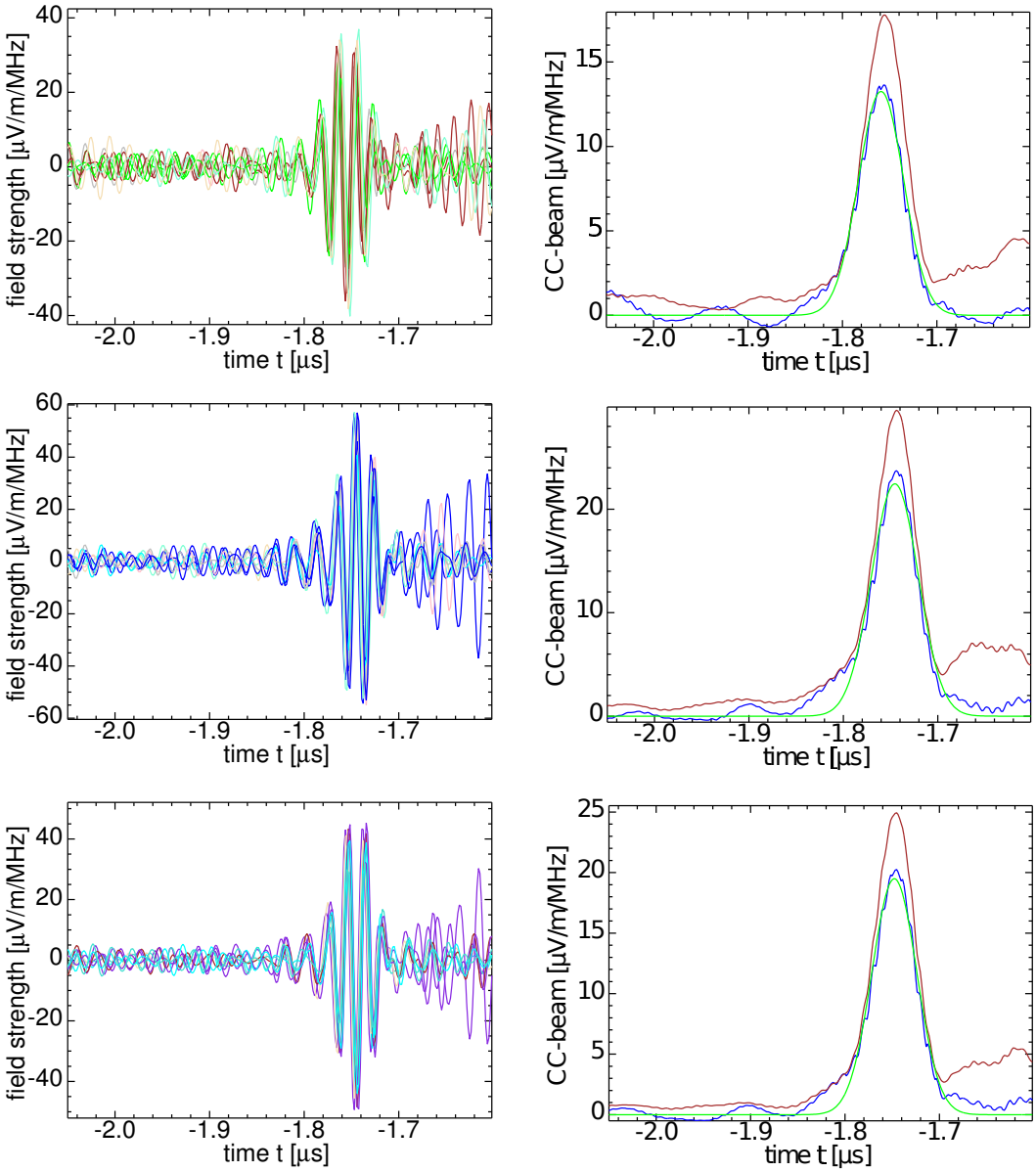

Figure 7.2.: Recorded and reconstructed traces for the east-west, north-south and vertical component on the left side and on the right side the according classically calculated CC-beam (blue), Power-beam (red) and the Gaussian fit to the CC-beam (green) of one event after full reconstruction.

7.2. Contribution of the $\vec{v} \times \vec{B}$-Model

The main part of the emission of radio pulses from extensive air showers can be described by a simple $\vec{v} \times \vec{B}$ dependence. This was confirmed by several

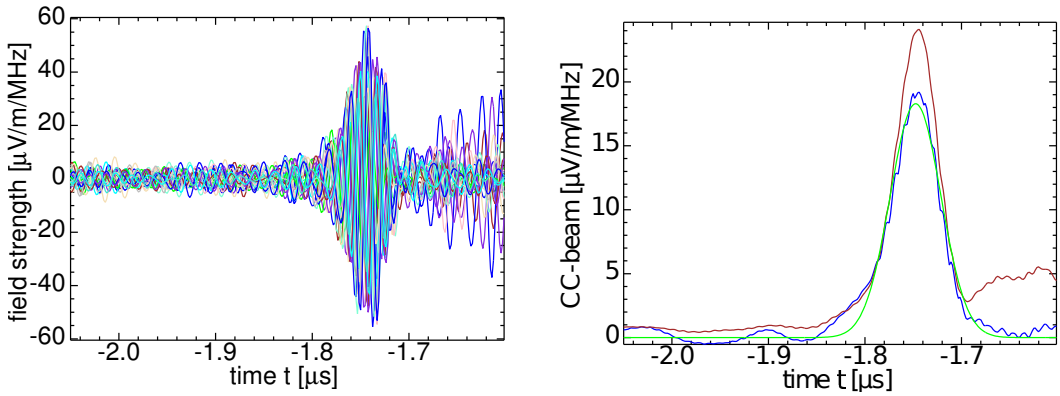

Figure 7.3.: Recorded and reconstructed traces for the same event shown in figure 7.2 but using vectorial beamforming on the left side and on the right side the according CC-beam (blue), Power-beam (red) and the Gaussian fit to the CC-beam (green). In this presentation the single components of the electric field vector are shown, thus they can be shifted against each other by $180°$, whereas the electric field vectors are still in phase

experiments. A second-order emission mechanism is the charge excess which was also confirmed by CODALEMA (Marin and et al., 2011) and AERA (Aab et al., 2014). The AERA group has estimated the net contribution of charge excess to be $\approx 14\%$ in agreement with older publications (Prescott J. R. and K., 1971). In the case of LOPES 3D all three electric field components are measured, thus for the first time analyses of the orientation of the electric field vector have become feasible. In order to analyse the $\vec{v} \times \vec{B}$ dependence the following analysis is conducted. The measured electric field vector is divided in a part which is parallel to the $\vec{v} \times \vec{B}$ predicted vector and a part perpendicular to it. The fraction of the electric field vector oriented in $\vec{v} \times \vec{B}$ direction is then plotted as a function the geomagnetic angle. The agreement between the predicted and the measured vector is expected be good for large angles since here the $\vec{v} \times \vec{B}$ is dominant and should be weaker the smaller the angle gets. In figure 7.6 this measured fraction is shown. For each measured electric field vector $\vec{E}$ the ratio $\frac{|\vec{E}_{\parallel \vec{v} \times \vec{B}}|}{|\vec{E}|}$ was calculated and the average for each bin was plotted. For this analysis the datasets were: normal-KASCADE plus inclined-KASCADE. The cuts were a signal-to-noise ratio of the CC-beam of $MPV + 2 \cdot \sigma = 5.0$, at least 50% of the received power has to be coherent and the signal-to-noise ratio in single electric field vectors has to be greater than 2. In total 80 measured electric field vectors from 28 events survive these cuts. It can be seen that as expected the fraction gets lower for smaller geomagnetic angles. Furthermore for geomagnetic angles greater than $45°$ the contribution of the geomagnetic effect can be estimated to be $\geq 65\%$. The noise is not considered in this plot. However, with decreasing geomagnetic angle the emission gets weaker and with this the influence of noise for smaller geomagnetic

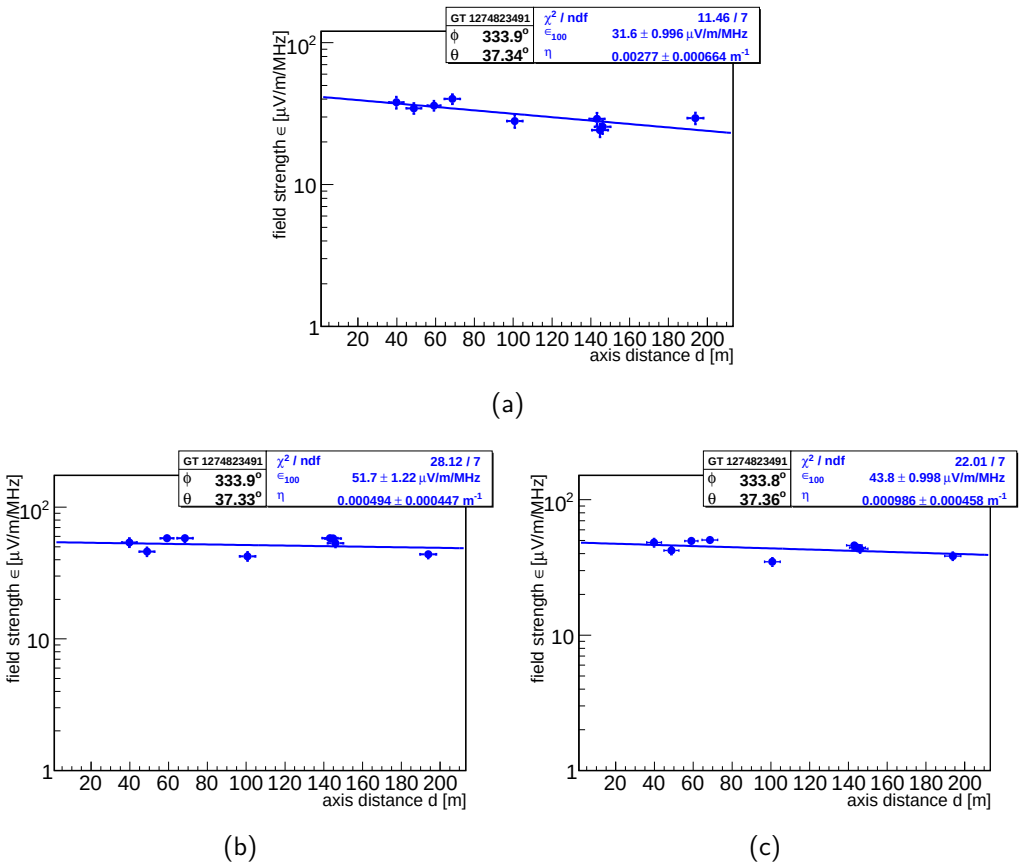

Figure 7.4.: Lateral distribution functions and an exponential fit for the same event shown in figure 7.2 measured with LOPES 3D for the east-west, north-south and vertical component. The errors are calculated according to the standard procedure of the analysis framework. This is an event with very high amplitudes, thus it is far away from the region for which the standard calculation was developed. An alternative estimation for the errors is discussed in section 7.1.1 and shown for the same event in figure 7.5.

angles is in general larger. Nevertheless geomagnetic emission can be confirmed to be the dominant emission mechanism.

7.3. A Parameter Representing the Charge-Excess Contribution

Within this thesis an analysis procedure was developed to use the reconstructed electric field vector to search for hints of a second order emission mechanism. This

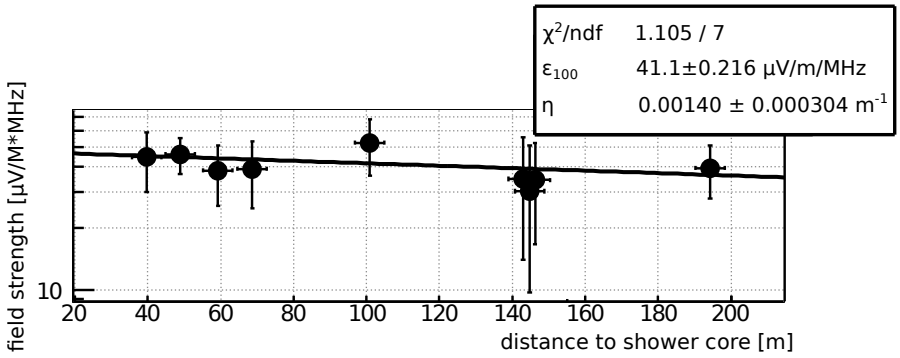

(a) Absolute field strength of the measured electric field vector projected to the shower plane. Error bars represent the part of the vector that is perpendicular to the shower plane.

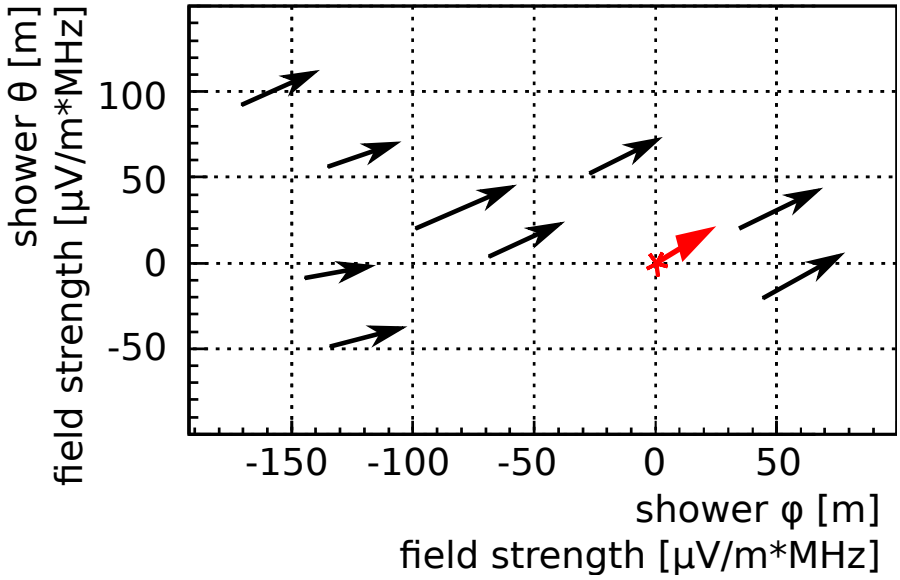

(b) Orientation of the measured electric field vectors in the shower plane. The vectors start at the antenna position and the length is the field strength in $\frac{\mu V}{m \cdot MHz}$. The red arrow starting at the star is the predicted emission vector according to the $\vec{v} \times \vec{B}$-model. This model only makes predictions on the orientation of the vector not the absolute emission, therefore only the direction of the vector is of interest in this plot. The red star marks the position of the shower core.

Figure 7.5.: Lateral distribution functions for a measured event.

analysis can be adopted for any air shower radio experiment if the geomagnetic field, the arrival direction and the shower core are known. A charge-excess-like emission mechanism is suggested when statistically combining measured electric field vectors from single tripoles. Nevertheless, the data quality of LOPES 3D is low, thus we can not claim to have significant evidence for a charge-excess like

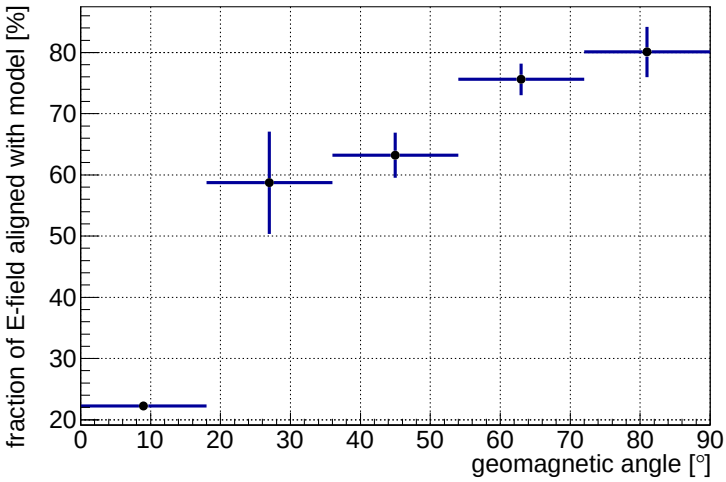

Figure 7.6.: Fraction of the electric field vector pointing in the $\vec{v} \times \vec{B}$ direction.

emission mechanism. In the following the analysis is described, starting with the discussion of the electric field vector measurement.

7.3.1. Measurement of the electric field Vector

At the LOPES site the radio background is very high, thus a CC-beamforming is mandatory in order to measure the radio emission from cosmic ray air showers. During the CC-beamforming all components of the electric field vector get a positive algebraic sign. This is due to filtering and the beamforming procedure in which the time traces are shifted with respect to each other. The resulting effects on the measurement are described in equation 7.1 and sketched in figure 7.7. With this the reconstructed electric field vector always has positive algebraic signs in all components. For simplicity the two dimensional case is discussed in the following, however, the statements developed are also valid for the three dimensional case. In figure 7.7 the conversion of the electric field vector during the measurement and reconstruction is sketched. Here the dashed green vectors mark the three other possibilities of an emitted vector that are all converted to the same solid green vector during the measurement and reconstruction procedure.

$$\begin{pmatrix} E_1 \\ E_2 \\ E_3 \end{pmatrix} \rightarrow \begin{pmatrix} |E_1| \\ |E_2| \\ |E_3| \end{pmatrix} \tag{7.1}$$

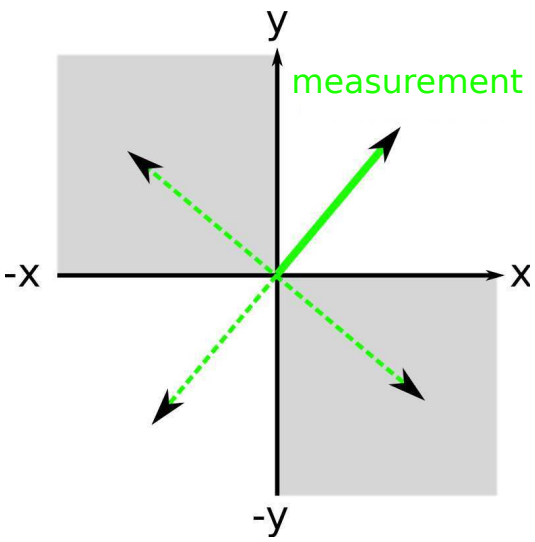

Figure 7.7.: Sketch explaining the information loss during the measurement of the electric field vector. The electric field vector is measured with absolute value in every component. With this every vector indicated by the dashed lines is converted to the vector drawn with solid line.

7.3.2. Cut Definitions Considering the Measurement of the electric field Vector

The loss of the algebraic sign of the single vector components is a serious issue when comparing measured vectors with model assumptions. Therefore the cuts have to be selected very carefully. In principle there are two ways to compensate this information loss.

- The sign can be reconstructed using the model assumption from the main emission model (i.e. the $\vec{v}\times\vec{B}$-model). This is not applicable for this analysis since a reconstruction of the electric field vector using model assumptions would prevent an unbiased model comparison.

- The electric field vector is reconstructed in the antenna coordinate system and additionally converted according to equation 7.1.The emitted vector has to lie in the shower plane. Consequently, only vectors that are not affected by the loss of the algebraic sign will also lie mainly in the shower plane after the reconstruction. These are the vectors that have the same algebraic sign in all components. The reconstructed vectors are divided into a part lying in the shower plane $\vec{E}_{\parallel}$ and a part perpendicular to the shower plane $\vec{E}_{\perp}$. After this a cut is applied on the fraction $\frac{|\vec{E}_{\parallel}|}{|\vec{E}_{\perp}|}$. This fraction has to be larger than 20 for two reasons. Firstly, with this tight cut it is assured that the reconstructed electric field vectors mainly lie in the

shower plane also after the reconstruction. Secondly, the part perpendicular to the shower plane is either originating from the loss of the algebraic sign during the reconstruction, or due to noise. Thus the fraction $\frac{|\vec{E}_{\parallel}|}{|\vec{E}_{\perp}|}$ can be interpreted as a signal-to-noise ratio. With the cut value of 20 a sensitivity to a $\approx 5\%$ effect is assured. This is well motivated since on average the charge excess contribution is found to be 14% in Argentina (Schoorlemmer, 2013). This leads to an expected average charge excess contribution of 7% for LOPES 3D, because the Earth's magnetic field in Karlsruhe is twice as strong (Barton, 1997). In principle a higher cut on the signal-to-noise ratio is desirable but not feasible with LOPES 3D data due to limited statistics.

With the cut described above the measured electric field is determined except for one degree of freedom, which is the algebraic sign of the complete vector. This is also sketched in figure 7.7, here the grey shaded areas are excluded. To be able to compare this measured vector with model predictions the following approach was chosen. First the predicted vector according to the $\vec{v} \times \vec{B}$-model was calculated for the arrival direction of the air shower. After this the algebraic signs in all components were checked. If the predicted $\vec{v} \times \vec{B}$-vector had mixed algebraic signs this shower would not have been considered in the analysis. Then the vector was converted according to equation 7.1 to be comparable to the measurement.

7.3.3. Derivation of a Charge-Excess-Sensitive Parameter

In this analysis predictions for the orientation of the electric field vector projected on the shower plane according to two models are taken into account. A method was derived which allows an analytic calculation of the relative contribution of the charge excess to the $\vec{v} \times \vec{B}$ prediction in a measured vector. This is done in the following way: First the two predicted vectors in the shower plane are normalized, this is done since only the predicted directions and not the length of the electric field vector are used in this analysis. The two predicted vectors $\vec{E}_{\mathsf{vxB}}$ and $\vec{E}_{\mathsf{ce}}$ are combined to match the orientation of the measurement $\vec{E}_{\mathsf{m}}$ according to equation 7.2. Naturally only the directions of the vectors are taken into account and not their lengths.

$$\mathsf{Dir}(\vec{E}_{\mathsf{m}}) = \mathsf{Dir}(\vec{E}_{\mathsf{vxB}} + k \cdot \vec{E}_{\mathsf{ce}}) \tag{7.2}$$

With this k is determined and can be calculated using the following condition, cf. equation 7.3.

$$\begin{pmatrix} E_{\mathsf{m},1} \\ E_{\mathsf{m},2} \\ E_{\mathsf{m},3} \end{pmatrix} \times \begin{pmatrix} E_{\mathsf{vxB},1} & +k \cdot E_{\mathsf{ce},1} \\ E_{\mathsf{vxB},2} & +k \cdot E_{\mathsf{ce},2} \\ E_{\mathsf{vxB},3} & +k \cdot E_{\mathsf{ce},3} \end{pmatrix} \stackrel{!}{=} \begin{pmatrix} 0 \\ 0 \\ 0 \end{pmatrix} \tag{7.3}$$

Since the vectors lie in the shower plane their third component always equals 0. With this, k is determined according to equations 7.4, 7.5 and 7.6.

$$\begin{pmatrix} E_{\text{vxB},1} & +k \cdot E_{\text{ce},1} \\ E_{\text{vxB},2} & +k \cdot E_{\text{ce},2} \\ 0 & +k \cdot 0 \end{pmatrix} \times \begin{pmatrix} E_{\text{m},1} \\ E_{\text{m},2} \\ 0 \end{pmatrix} \stackrel{!}{=} \begin{pmatrix} 0 \\ 0 \\ 0 \end{pmatrix} \tag{7.4}$$

$$\Rightarrow (E_{\text{vxB},1} + k \cdot E_{\text{ce},1}) \cdot (E_{\text{m},2}) - ((E_{\text{vxB},2} + k \cdot E_{\text{ce},2}) \cdot (E_{\text{m},1})) = 0 \tag{7.5}$$

$$\Rightarrow k = \frac{E_{\text{m},1} \cdot E_{\text{vxB},2} - E_{\text{m},2} \cdot E_{\text{vxB},1}}{E_{\text{m},2} \cdot E_{\text{ce},1} - E_{\text{m},1} \cdot E_{\text{ce},2}} \tag{7.6}$$

This k-parameter represents the relative composition of the charge excess to the $\vec{v}\times\vec{B}$ prediction needed to match the direction of the measured electric field vector. When considering the amplitudes of the two emission mechanisms a quantity can be derived which is constant to first order. This is done in the following way. To first order both emission mechanisms depend approximately linearly on the energy e_s of the shower (Horneffer et al., 2008; Gorham et al., 2007). The $\vec{v} \times \vec{B}$ prediction additionally depends on the sine of the geomagnetic angle α. With this the product of the k-parameter with $\sin(\alpha)$ should be constant according to equations 7.7 and 7.8, assuming the same linear energy dependency for both emission mechanisms.

$$\Rightarrow k = \frac{|\vec{E}_{\text{vxB}}|}{|\vec{E}\text{ce}|} \approx \frac{f(e_s)}{g(e_s, \sin(\alpha))} \tag{7.7}$$

$$\Rightarrow k \cdot \sin(\alpha) \approx \text{constant} \tag{7.8}$$

7.3.4. The k-Parameter in Data

The observation of the k-parameter in LOPES 3D data is only possible for the constant product $k \cdot \sin(\alpha)$. LOPES is affected by high background noise and a non-constant quantity would not be distinguishable from background. Nevertheless, when the constant quantity $k \cdot \sin(\alpha)$ is found, the charge excess contribution for single air showers can be calculated if the geomagnetic angle α is known. In addition to the cuts on a successful reconstruction motivated in chapter 4 the following cuts had to be applied to the data: In order to ensure high data quality but also enough statistics the cut on the fraction $\frac{|\vec{E}_{\parallel}|}{|\vec{E}_{\perp}|}$ was set to 20, as motivated above. Furthermore, a cut of at least 45° between predicted electric field vectors from the $\vec{v} \times \vec{B}$-model and the charge excess, respectively, was applied. This cut is needed to have a large lever arm, since the method works only on

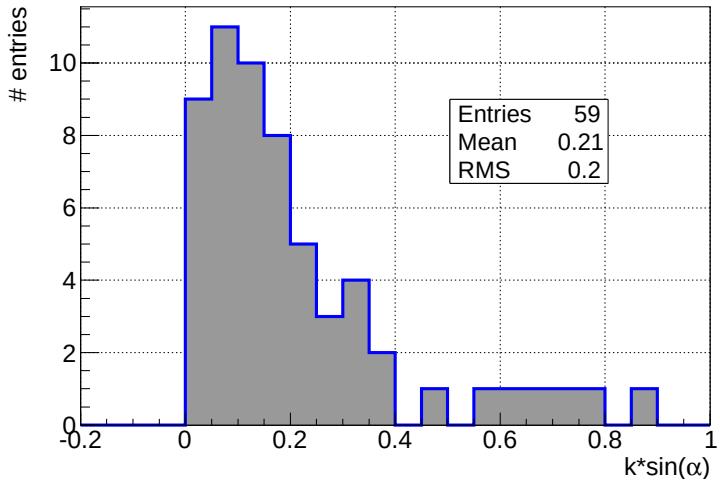

Figure 7.8.: Distribution of the measured $k \cdot \sin(\alpha)$ distribution for the Grande-normal dataset. The peak value at 0.1 indicates a charge excess like emission mechanism. This is not significantly seen due to the low data quality.

directions. In principle the method gets more effective the higher the angle is chosen. Like the cut on the fraction $\frac{|\vec{E}_{\parallel}|}{|\vec{E}_{\perp}|}$ the low cut of at least $45°$ is due to the low statistics. As described above, the measured electric field vector and the predicted electric field vector from the $\vec{v} \times \vec{B}$-model are determined except for the algebraic sign. Thus, the measured vector is reconstructed either by $\vec{E}_{\text{vxB}} + k \cdot \vec{E}_{\text{ce}}$ or by $\vec{E}_{\text{vxB}} + (-1 \cdot k) \cdot \vec{E}_{\text{ce}}$. Consequently only the absolute value of the product $k \cdot \sin(\alpha)$ can be analysed.

The distribution of $k \cdot \sin(\alpha)$ for the Grande-normal dataset is shown in figure 7.8. The 59 entries originate from 23 events in total with 1 to 6 suitable electric field measurements. It was only possible to do this analysis for the Grande-normal dataset since for the KASCADE-normal dataset only four measurements survived the quality cuts. This shows that this analysis suffers strongly from the limited data quality of LOPES 3D. In principle measurements of air showers with higher energies are needed to look for a ≈7% effect in the noisy environment of LOPES. However, KASCADE-Grande (and by this also LOPES) is not sensitive to such high energies. Nevertheless, the analysis was applied on data and a peak at a value of ≈ 0.1 was observed. To check the validity of this value the following approach was chosen. The distribution of $k \cdot \sin(\alpha)$ was calculated for the same cuts but no cut on the fraction $\frac{|\vec{E}_{\parallel}|}{|\vec{E}_{\perp}|}$. Thus the influence of noise on the distribution can be studied. The distribution is shown in figure 7.9(a). For noise the peak value is 0. This is expected since a value of 0 means that the measured electric field vector is completely aligned with the $\vec{v} \times \vec{B}$-predicted vector. The product $k \cdot \sin(\alpha)$ gets

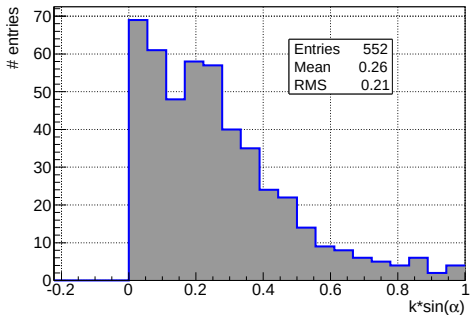

(a) Background distribution for $k \cdot \sin(\alpha)$.

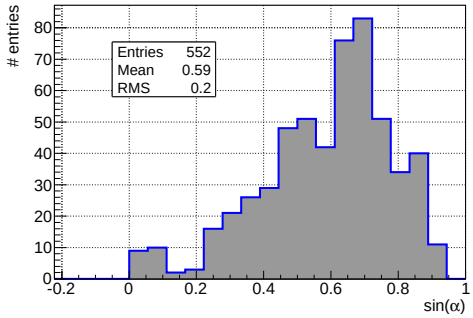

(b) Background distribution for $sin(\alpha)$.

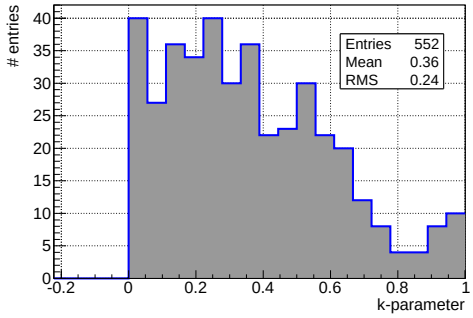

(c) Background distribution for k.

Figure 7.9.: Background for the product $k \cdot \sin(\alpha)$ and both factors separately to check if the observed peak in figure 7.8 is background induced.

higher values the more the measured electric field vector is aligned with the charge excess predicted direction. Naturally, high values are less probable since this would imply a large deviation from the main emission mechanism. Nevertheless a peak on top of the background at ≈ 0.25 is observed. To investigate the origin of this peak the distributions of the k-parameter and the sine of the geomagnetic angle α were plotted separately. The observed peak at ≈ 0.25 is due to the folding of typical $\sin(\alpha)$ values with the derived k-parameter, see also figures 7.9(b) and 7.9(c).

Observing the peak of the $k \cdot \sin(\alpha)$ distribution for higher quality data at a different value than in the distribution containing more noise is a weak indication to a charge-excess like emission mechanism in LOPES 3D data. Nevertheless we cannot exclude that the observed peak in the higher quality data set is due to a statistical fluctuation of the background. The width of this distribution gives an estimation of the high noise level present at the LOPES site.

The value of $k \cdot \sin(\alpha) \approx 0.1$ was chosen for a $\vec{v} \times \vec{B} + k(\alpha) \cdot \vec{ce}$-model, with $k(\alpha) \approx \frac{0.1}{\sin(\alpha)}$. The derived value for $k \cdot \sin(\alpha)$ was determined by the position of the peak and not the mean value of the distribution since in this distribution the

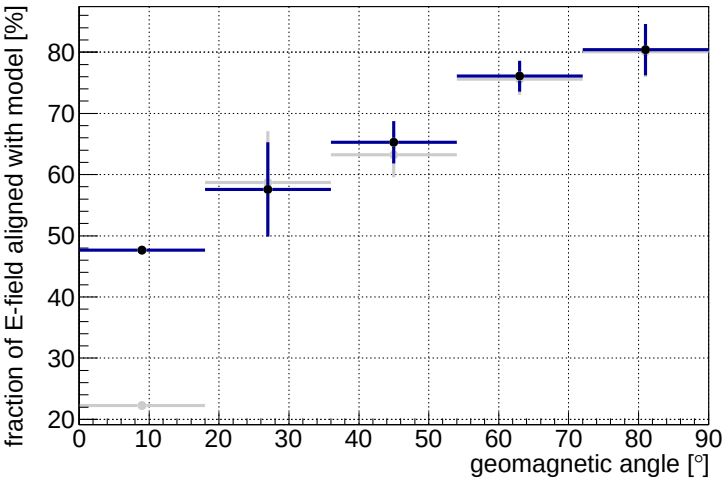

Figure 7.10.: Fraction of the electric field vector pointing in the $\vec{v}\times\vec{B}+\frac{0.1}{\sin(\alpha)}\cdot ce$ direction in blue, and fraction of the electric field vector pointing in the $\vec{v}\times\vec{B}$ direction in grey.

absolute value of the product $k\cdot\sin(\alpha)$ was used and thus the mean value is biased towards larger values. The measured electric field vectors were tested against this model the same way as they were tested against the pure $\vec{v}\times\vec{B}$ assumption as described above in section 7.2. In figure 7.10 the agreement with this model is shown for the same data as in section 7.2. The pure $\vec{v}\times\vec{B}$ assumption is shown in light grey and in blue the new $\vec{v}\times\vec{B}+k(\alpha)\cdot\vec{ce}$ model. A weak and not significant improvement in describing the measured electric field vector on average is seen. This is another hint for a charge-excess-like second-order emission mechanism.

7.4. Conclusion

In this chapter the standard LOPES analysis procedure was presented. Furthermore an update on the ldf was introduced which allows to calculate an ldf of the complete electric field vector. With this an estimate on the noise was derived which allows an evaluation of the noise at the very moment of the measurement. The $\vec{v}\times\vec{B}$ model was confirmed by statistically comparing the predictions of the model with measured electric field vectors. Furthermore, a method was developed to analytically calculate the charge excess contribution in a measured electric field vector. This method was applied on a suitable set of electric field vectors recorded with LOPES 3D. The derived result was tested on a second data set. An indication for a charge-excess-like second-order emission mechanism was found, however it was not statistically significant.

CHAPTER 8

Studies on the Benefits of Measurements with Vertical Antennas

The outstanding feature of LOPES 3D is the additional direct measurements with vertically aligned antennas. In this chapter we discuss the benefits of these measurements. With equations 5.8 and 5.9 it is proven that with measurements of two antennas at the same place the complete electric field vector can be reconstructed when knowing the arrival direction of the shower. At LOPES 3D we measure air showers with three antennas at the same place, thus the electric field vector can be reconstructed three times. Several methods to make use of this redundancy are developed and discussed. These methods are tested on data with a focus on inclined showers. Additionally the background noise is studied.

8.1. Sky Coverage in the Context of the Antenna Gain

When measuring air showers one crucial point is the direction-dependent sensitivity of the detector. It is in principle desirable to have a full sky coverage because this results in the largest fiducial volume and by this the best statistics. However to achieve a full sky coverage, an additional measurement with vertically aligned antennas is indispensable from the theoretical point of view. This can be explained when looking at the direction (and polarization) dependent sensitivity of

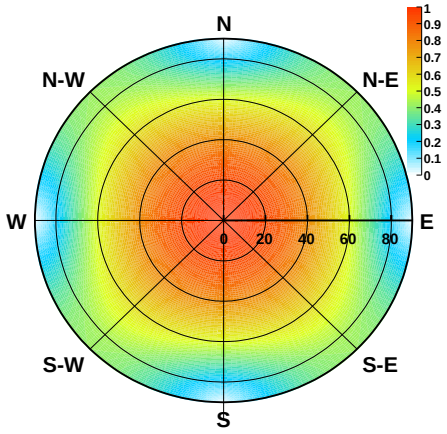

(a) Estimated sensitivity of east-west aligned antenna combined with a north-south aligned antenna.

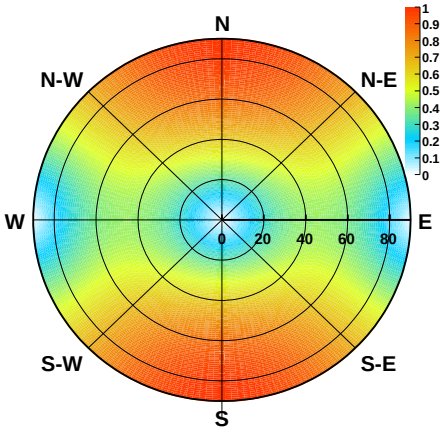

(b) Estimated sensitivity of east-west aligned antenna combined with a vertically aligned antenna.

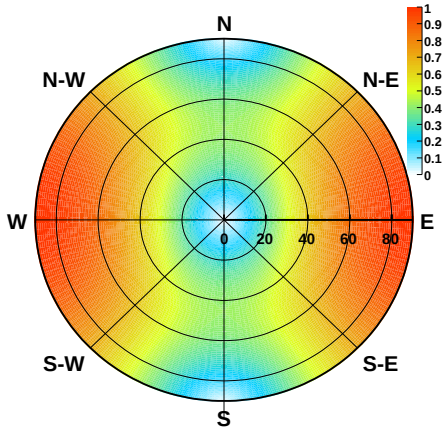

(c) Estimated sensitivity of north-south aligned antenna combined with a vertically aligned antenna.

Figure 8.1.: Normalized estimated maximum sensitivity of two pairs of antennas depending on the direction of the incoming radio signal.

a dipole antenna[1]. A horizontal dipole aligned with the north-south direction for example is not capable of detecting radio signals arriving from the horizon if they are arriving from north or south. Even if the radio signals are arriving from east or west, this antenna can only measure them if they are partly horizontally aligned.

[1] In this case dipole antennas are discussed since they are used within LOPES 3D but in principle most antenna types have a region with nearly no sensitivity and thus this discussion is valid for most antenna types.

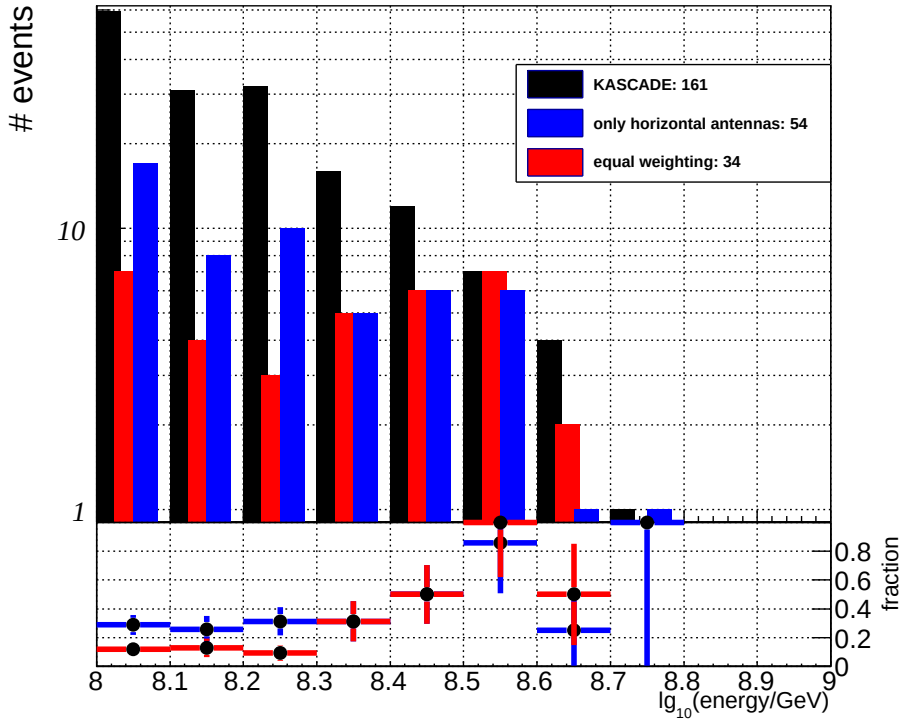

Figure 8.2.: Number of reconstructed events combining all reconstructed vectors equally compared to the former LOPES weighting (only north-south and east-west).

This feature is true for any horizontally aligned antenna if the geometry is adapted accordingly. Thus the vertical component of radio signals that are arriving from the horizon can never be measured when using only horizontally aligned antennas. To correctly reconstruct the electric field vector measurements with at least 2 antennas at the same place are required, cf. chapter 5. When measuring with only horizontally aligned antennas this is not realisable for the full sky any more since the regions where one of these two antennas is not sensitive have to be excluded. To have easier access to this discussion, the measurement is simplified as a projection of the electric field vector on the axis aligned with the antenna, which gives in first order a good approximation. In figure 8.1(a) the sensitivity of two horizontally aligned antennas using the simplification described above is shown. Even in the best case scenario of a horizontally aligned vector a large fraction of the horizon has to be excluded, this will get even worse if the electric field vector is partly vertically aligned. The sensitivity to these regions and partly vertically oriented electric field vectors can only be achieved by additional measurements with vertically aligned antennas.
If the vector is completely aligned with one of the horizontal antennas only this

antenna will measure a signal. But, only when the vertically aligned antenna and the other horizontally aligned antenna both measure no signal it is proven that the vector is completely aligned with the antenna. In any other case at least one of the other antennas will measure a signal.
In figures 8.1(b) and 8.1(c) the sensitive regions of a vertically aligned antenna combined with each horizontal antenna are shown. With this it is shown that a full sky coverage is only feasible with additional measurements with vertically aligned antennas.

8.2. Measurements of Vertical Showers

In chapter 5 we have shown that the complete electric field vector can be reconstructed with a measurement with two antennas at the same place, if the arrival direction is known. LOPES 3D was measuring with three antennas at the same place, thus the electric field vector can be reconstructed three times. This brings up the question how to gain the maximum advantage of this redundancy. Either noisy or broken channels can be compensated or the reconstruction of the electric field vector can be performed three times using every combination of two antennas. The first, straightforward, approach how to handle this redundancy is to take the mean of all three reconstructed electric field vectors. This has several draw backs:

- Not every reconstruction has the same accuracy and quality.
- A dipole is insensitive to arrival directions along the the dipole axis. Thus, it can happen for dedicated arrival directions that only two dipoles are sensitive. (For this case all reconstructions using data recorded with the insensitive dipole should be taken out of the analysis.)
- From the emission models there are reliable predictions how much signal will be emitted in which component of the electric field. (Reconstructions using channels with no expected signal should be taken out of the analysis.)
- Background noise is not considered. (Most of the anthropogenic noise is expected to be present in the vertical component (Rothammel, 1995).)

In figure 8.2, the fraction of reconstructed events is shown for the KASCADE-normal dataset: once only taking the reconstruction from measurements with the two horizontally aligned antennas into account and once combining every reconstruction of the electric field vector with equal weight. In total fewer events

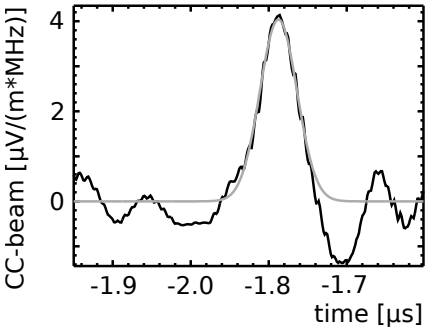

(a) CC-beam in black and Gaussian fit in grey for the east-west component of the electric field vector reconstructed using only horizontally aligned antennas.

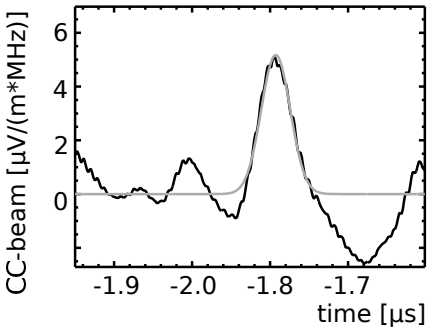

(b) CC-beam in black and Gaussian fit in grey for the north-south component of the electric field vector reconstructed using only horizontally aligned antennas.

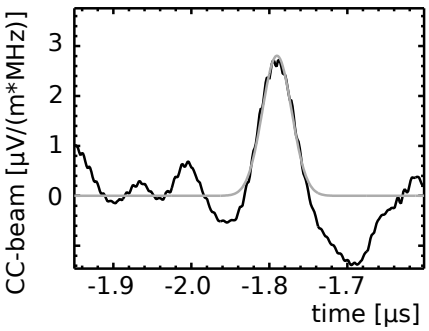

(c) CC-beam in black and Gaussian fit in grey for the vertical component of the electric field vector reconstructed using only horizontally aligned antennas.

Figure 8.3.

can be reconstructed in the latter case.
Nevertheless, the fraction of reconstructible events increases for higher energies. This is expected for both reconstructions since the signal increases with rising energy. With this also a signal above threshold in the vertically aligned antennas is expected.
It was shown that combining the different reconstructions of the electric field vector impacts the number of reconstructible radio events. Thus, the effect of differently weighting the three reconstructions of the electric field vector is studied and is discussed in the following. To have a better access to this topic one example event and the fraction of reconstructible events is shown. In figure 8.3 the CC-beam of the example event is shown for all three components of the electric field vector separately. The reconstructed energy of the primary particle which induced

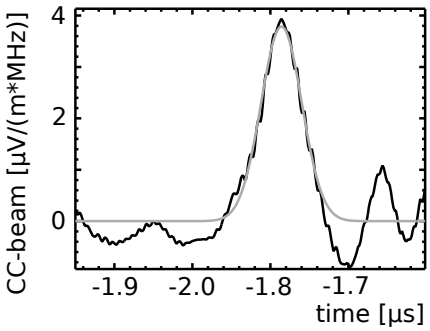

(a) CC-beam in black and Gaussian fit in grey for the east-west component of the electric field vector reconstructed using equal weights for all three reconstructions.

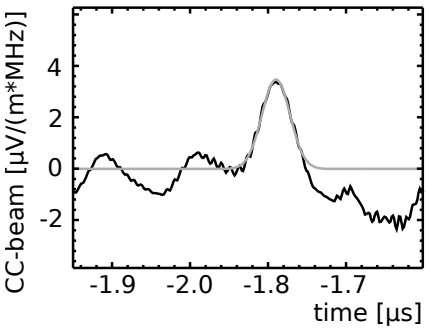

(b) CC-beam in black and Gaussian fit in grey for the north-south component of the electric field vector reconstructed using equal weights for all three reconstructions.

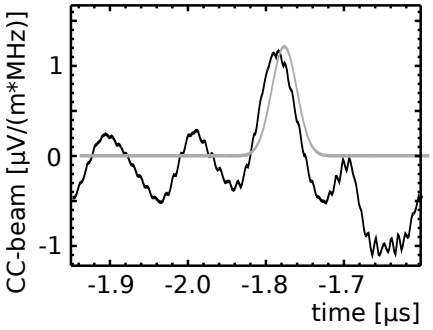

(c) CC-beam in black and Gaussian fit in grey for the vertical component of the electric field vector reconstructed using equal weights for all three reconstructions.

Figure 8.4.

this shower was $10^{17.1}$ eV. The shower arrived with an azimuthal angle of $26.1°$ and a zenith angle of $27.0°$. The radio signal from the shower is visible in all three components at the expected time of ≈ -1.8 µs. When using only horizontally aligned antennas the CC-beam value is higher compared to the CC-beam when equally combining all three reconstructions, which is shown in figure 8.4.

8.2.1. The Active Antenna Height

Another possibility to reconstruct the electric field vector using measurements from all three dipoles is the active antenna height. In this approach the sensitivity of the antennas is considered according to the arrival direction of the shower

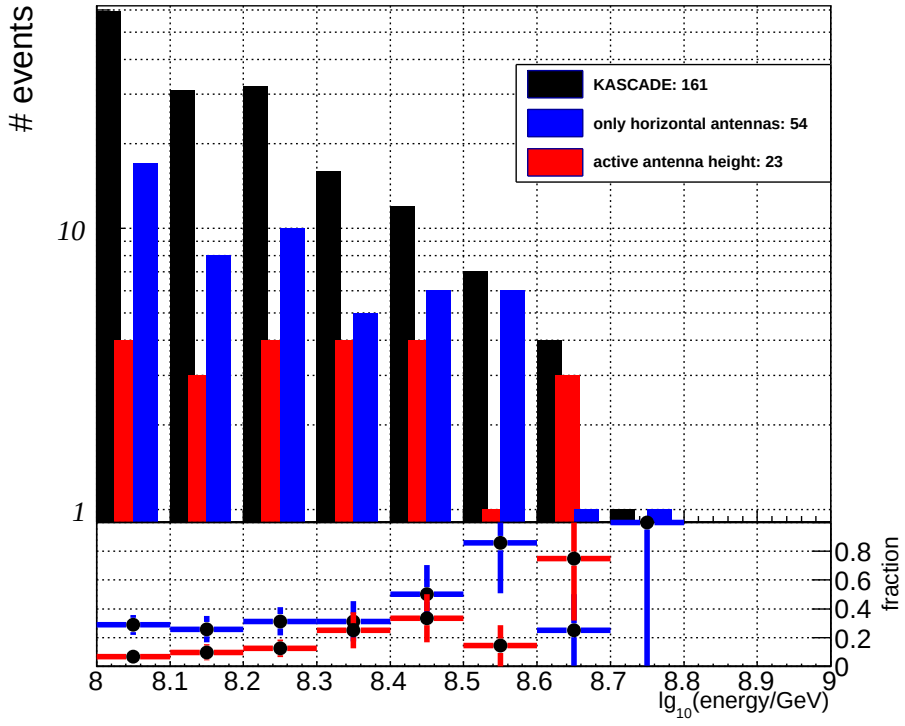

Figure 8.5.: Number of reconstructed events using the active antenna height compared to the former LOPES weighting (only north-south and east-west).

whereas the information that the electric field vector has to lie in the shower plane is ignored. Thus, the redundancy of the measurement with three antennas gets lost and all three measurements need to be used to reconstruct the electric field vector. The active antenna height is derived in the following way: The antenna gain $\vec{G}$ is simulated in the coordinate system of the antenna. This is done for all three antennas of one tripole. Then these gain-vectors are combined into a matrix. This matrix is used to describe the measurement according to equation 8.1.

$$\begin{pmatrix} G_{\mathrm{ew},1} & G_{\mathrm{ew},2} & G_{\mathrm{ew},3} \\ G_{\mathrm{ns},1} & G_{\mathrm{ns},2} & G_{\mathrm{ns},3} \\ G_{\mathrm{ve},1} & G_{\mathrm{ve},2} & G_{\mathrm{ve},3} \end{pmatrix} \times \begin{pmatrix} E_{\mathrm{ew}} \\ E_{\mathrm{ns}} \\ E_{\mathrm{ve}} \end{pmatrix} = \begin{pmatrix} V_{\mathrm{ant,ew}} \\ V_{\mathrm{ant,ns}} \\ V_{\mathrm{ant,ve}} \end{pmatrix} \tag{8.1}$$

With the components of the electric field vector E_{ew}, E_{ns} and E_{ve} and the corresponding voltages at the antenna foot-points $V_{\mathrm{ant,ew}}$, $V_{\mathrm{ant,ns}}$ and $V_{\mathrm{ant,ve}}$. Consequently, the inverse of this matrix can be used to derive the electric field vector

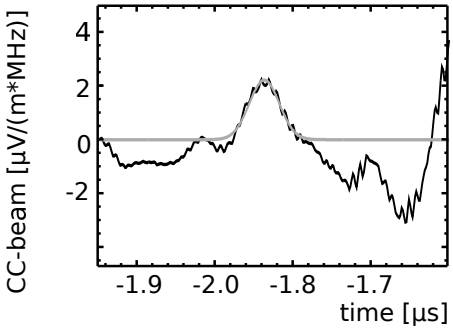

(a) CC-beam in black and Gaussian fit in grey for the east-west component of the electric field vector reconstructed using the active antenna height.

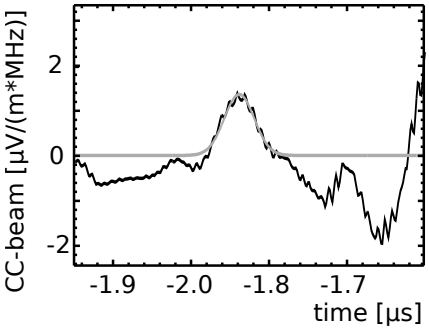

(b) CC-beam in black and Gaussian fit in grey for the north-south component of the electric field vector reconstructed using the active antenna height.

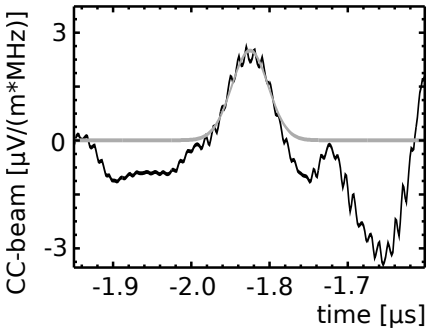

(c) CC-beam in black and Gaussian fit in grey for the vertical component of the electric field vector reconstructed using the active antenna height.

Figure 8.6.

from the measured voltages. This reconstruction is done according to equation 8.2.

$$\begin{pmatrix} E_{\mathrm{ew}} \\ E_{\mathrm{ns}} \\ E_{\mathrm{ve}} \end{pmatrix} = \begin{pmatrix} G_{\mathrm{ew},1} & G_{\mathrm{ew},2} & G_{\mathrm{ew},3} \\ G_{\mathrm{ns},1} & G_{\mathrm{ns},2} & G_{\mathrm{ns},3} \\ G_{\mathrm{ve},1} & G_{\mathrm{ve},2} & G_{\mathrm{ve},3} \end{pmatrix}^{-1} \times \begin{pmatrix} V_{\mathrm{ant,ew}} \\ V_{\mathrm{ant,ns}} \\ V_{\mathrm{ant,ve}} \end{pmatrix} \tag{8.2}$$

The fraction of reconstructed events using the active antenna height is shown in figure 8.5. With increasing energies also more events are reconstructible but fewer than with the former LOPES weighting. This is expected since the shower arrival direction is only used indirectly during the reconstruction, namely for the calculation of the active antenna height. In figure 8.6 the CC-beams of the example event are shown. As expected the reconstruction gets worse. Nevertheless

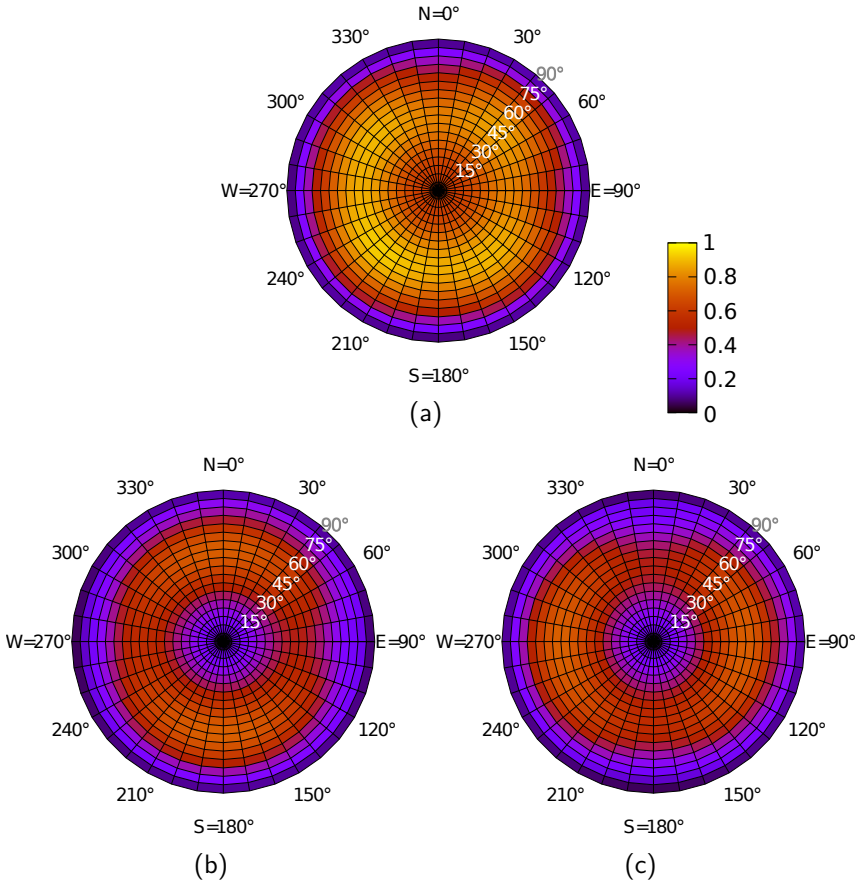

Figure 8.7.: Polar plot of the weighting-factors calculated with the gain-method for the reconstruction of the electric field vector using the following combination of two dipoles: east-west and north-south aligned (a), east-west and vertically aligned (b) and north-south and vertically aligned (c) antennas.

the air shower is seen in all three components at the expected time.

8.3. Weighting Methods for a Redundantly Determined electric field Vector

Within the scope of this thesis different weighting schemes considering the arrival direction of the air shower have been developed and studied. In the following the different approaches will be explained in detail:
When calculating the different weights it is important to consider that the elec-

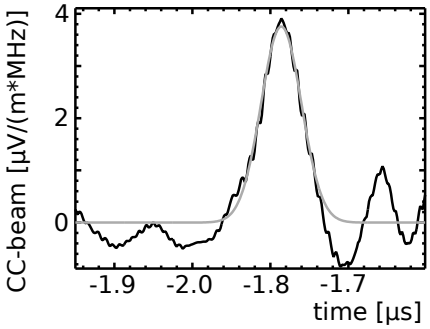

(a) CC-beam in black and Gaussian fit in grey for the east-west component of the electric field vector reconstructed using the gain-method weighting.

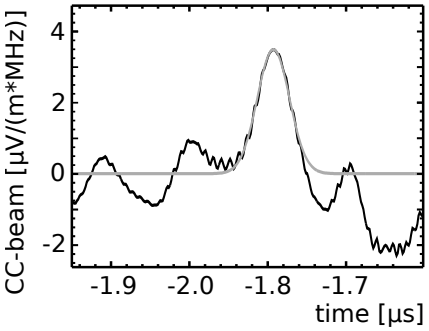

(b) CC-beam in black and Gaussian fit in grey for the north-south component of the electric field vector reconstructed using the gain-method weighting.

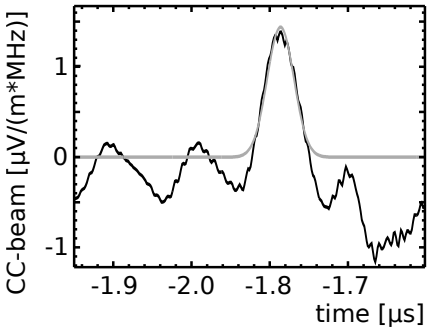

(c) CC-beam in black and Gaussian fit in grey for the vertical component of the electric field vector reconstructed using the gain-method weighting.

Figure 8.8.

tric field vector is reconstructed by combining measurements with two antennas. This means that the best results will be achieved when giving a high weight to that reconstruction which is performed using measurements from two antennas that measured a high signal. This is realized in the following way: First, quality factors for each of the three different antennas are defined. These quality factors depend on the arrival direction of the air shower. To obtain the weight for each pair of antennas, the two quality factors are multiplied. This multiplication avoids antennas with a quality factor of ≈ 0 (= no information) being considered. The product of the quality factors is then used as weight w_1, w_2 and w_3. The weighting of the three electric field vectors $\vec{E}_{EW-NS}$, $\vec{E}_{EW-VE}$ and $\vec{E}_{VE-NS}$, is then done according to equation 8.3.

$$\vec{E}_{EW-NS} \cdot \frac{w_1}{n} + \vec{E}_{EW-VE} \cdot \frac{w_2}{n} + \vec{E}_{VE-NS} \cdot \frac{w_3}{n} = \vec{E}_{\text{reconstructed}} \qquad (8.3)$$

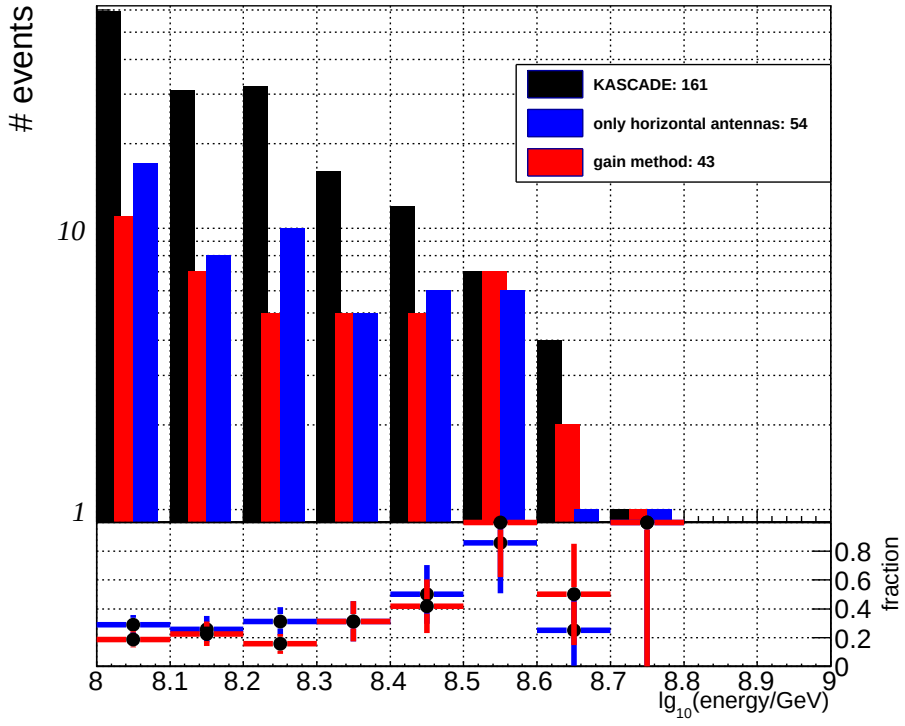

Figure 8.9.: Number of reconstructed events using the gain-method compared to the former LOPES weighting (only north-south and east-west).

with $n = w_1 + w_2 + w_3$. In the following two weighting schemes will be discussed. One weighting scheme was developed regarding the antenna properties, the so-called gain-method. In this approach we assume that antennas with a high sensitivity receive a high signal. Consequently these antennas get a high quality factor. Another weighting scheme was developed regarding the predicted emission, the so-called $\vec{v} \times \vec{B}$-method. In this approach we calculate the emission in the single components according to the $\vec{v} \times \vec{B}$-model. Consequently the antennas aligned with components which have a high predicted signal get a high quality factor.

8.3.1. The Gain-Method

In the gain-method the quality factors are defined by the simulated antenna sensitivity for each direction. The simulated total gain $\vec{G}$ of the antenna is converted from dBi to a factor that can be multiplied to the voltage at the antenna foot-point in order to get the electric field according to equation 8.4.

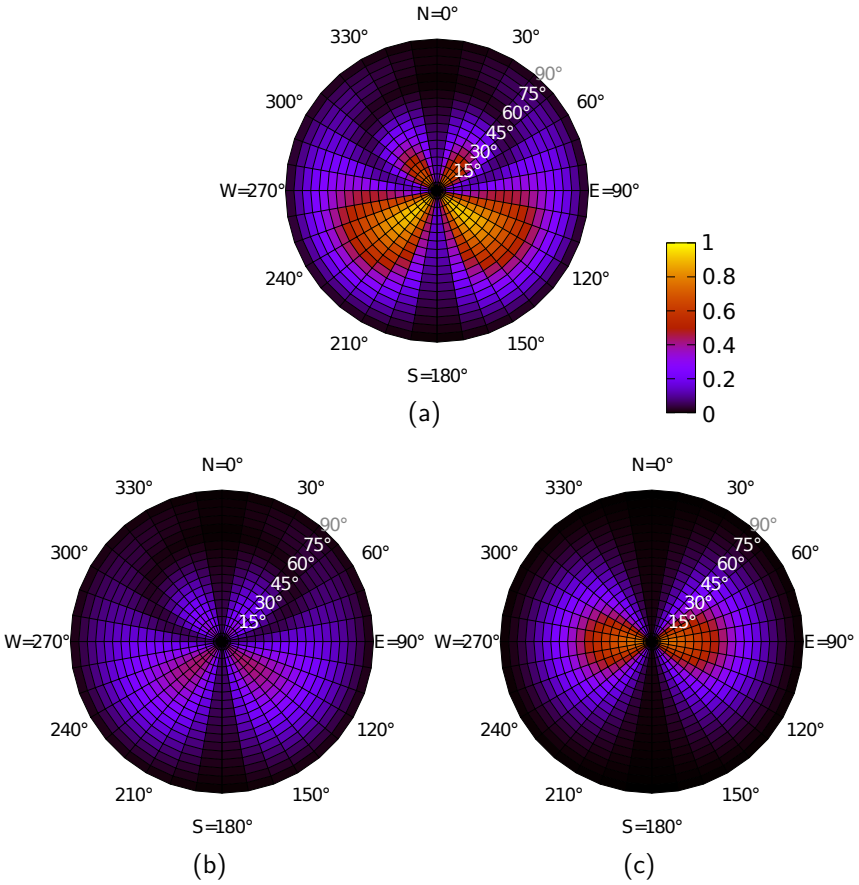

Figure 8.10.: Polar plot of the weighting-factors calculated with the $\vec{v} \times \vec{B}$-method for the reconstruction of the electric field vector using the following combination of two dipoles: east-west and north-south aligned (a), east-west and vertically aligned (b) and north-south and vertically aligned (c) antennas.

$$f_{\text{amp}} = \frac{1}{\sqrt{10^{\frac{|\vec{G}|}{20}}}} \tag{8.4}$$

This is calculated for all directions in the sky and for all frequencies in the bandwidth of LOPES 3D in $2\,\text{MHz}$ steps. Since the radio emission from air showers is broad band, the frequency values are averaged over the bandwidth. The inverse of these factors is used as the quality factor for the corresponding channel. Consequently arrival directions with a high sensitivity receive a higher quality factor. Thus, the electric field vector which is reconstructed with two antennas that have a high sensitivity to the arrival direction receives a high weight. The weighting factors are presented in figure 8.7.

The fraction of reconstructed events using the gain-method is shown in figure

8.9. It can be seen that the gain-method is effective for high energies. This is most probably connected to the higher signal in all dipoles since with this, the incorporation of the vertical dipoles leads to a contribution with a measured signal over threshold. In figure 8.8 the CC-beams for the example event are shown. An improvement compared to the active antenna height reconstruction can be seen. Nevertheless, the highest CC-beam values for this air shower are achieved when using only horizontal antennas.

8.3.2. The $\vec{v} \times \vec{B}$-Method

In the $\vec{v} \times \vec{B}$-method, the quality factors for each antenna are modelled by the predictions of the dominant geomagnetic emission mechanism. The emission is caused by the geomagnetic deflection of the charged particles in the Earth's magnetic field and can therefore be described by a $\vec{v} \times \vec{B}$ dependence with $\vec{v}$ the shower axis and $\vec{B}$ the vector pointing in the direction of the Earth's magnetic field. In equation 8.5 the calculation of the quality factors is described: with X_d being the quality factor for antenna d, $\hat{d}$ the normalized vector oriented parallel with the antenna. The Earth's magnetic field direction was assumed to be $B_{az} = 0^\circ$ and $B_{ze} = 64.4^\circ$ for the geomagnetic field in Karlsruhe (Barton, 1997)[2].

$$X_d = (\vec{v} \times \vec{B}) \cdot \hat{d} \tag{8.5}$$

These quality factors then lead to the weighting factors shown in figure 8.10. In figure 8.11 the fraction of reconstructible events using this weighting scheme is shown. It can be seen that for most of the events just considering the predicted polarization and not taking into account the detector characteristics leads to fewer reconstructed events. In the $\vec{v} \times \vec{B}$-method the measurements with vertical antennas get in general a higher weighting than in the other weighting schemes. These antennas have low sensitivity to signals arriving from the zenith. Thus measurements with these antennas are expected to have few air shower signals over threshold in case of near vertical air showers. Nevertheless, the example event was also reconstructible using this weighting method, see figure 8.12.

[2]The LOPES 3D antennas were adjusted with a compass. Thus the north-south dipole is aligned with the Earth's magnetic field. The declination of the electric field changed $21'$ over the runtime of LOPES 3D. This is far less than the accuracy for the antenna alignment performed with the compass and therefore ignored in the calculation.

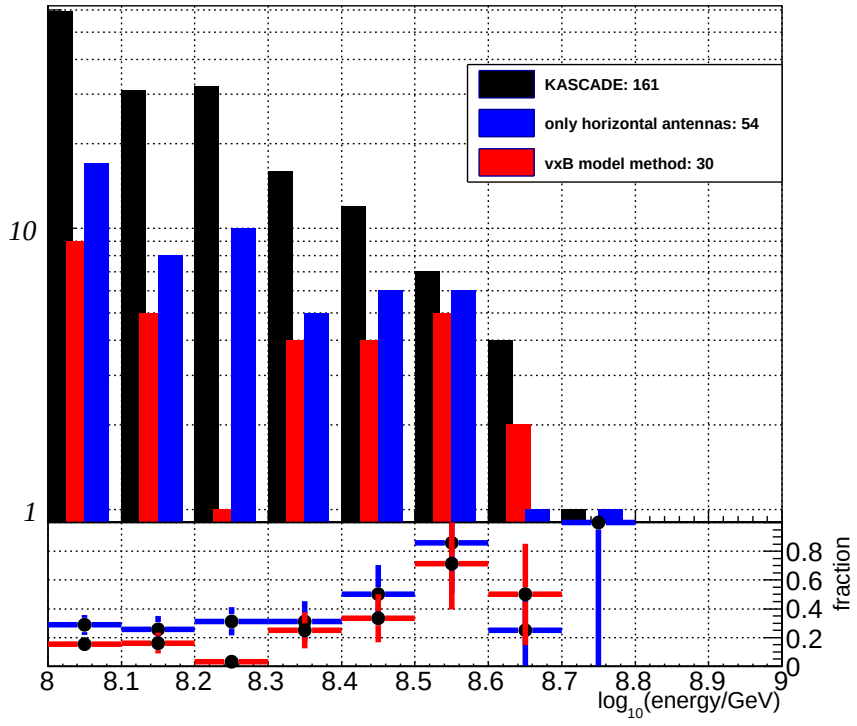

Figure 8.11.: Number of reconstructed events using the $\vec{v} \times \vec{B}$ method compared to the former LOPES weighting (only north-south and east-west).

8.3.3. Conclusion for Vertical Showers

For vertical showers, i.e. in this case showers with zenith angles smaller than $45°$, the former LOPES weighting (only using data from horizontal antennas) gives the best results in the number of reconstructible events and in addition the best reconstruction of the arrival direction. See figure 8.13 here the mean angular deviation between the reconstructed showers with LOPES and KASCADE is shown exemplary for reconstructions using only horizontally aligned antennas and the gain-method weighting scheme. The reconstructions using the other weighting schemes agree equivalently with the KASCADE-reconstructed direction within the uncertainties. For the corresponding KASCADE-Grande plots see appendix D. It is expected from geometrical considerations that using only horizontally aligned antennas to reconstruct showers with zenith angles smaller than $45°$ gives the best results. Every electric field vector lies in the shower plane and with this the projection of this vector to the north-south and east-west is always greater or equal to the projection to the vertical (for showers with zenith angles smaller than $45°$). Thus, in a selection of events with zenith angles smaller than $45°$, the

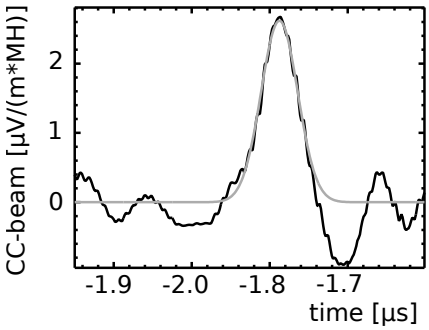

(a) CC-beam in black and Gaussian fit in grey for the east-west component of the electric field vector reconstructed using the $\vec{v} \times \vec{B}$ weighting.

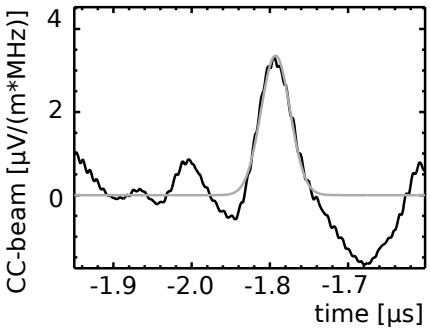

(b) CC-beam in black and Gaussian fit in grey for the north-south component of the electric field vector reconstructed using the $\vec{v} \times \vec{B}$ weighting.

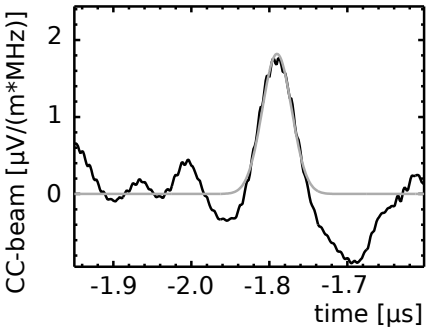

(c) CC-beam in black and Gaussian fit in grey for the vertical component of the electric field vector reconstructed using the $\vec{v} \times \vec{B}$ weighting.

Figure 8.12.

measurement with vertically aligned antennas can only contribute with equal or less signal compared to the two horizontal antennas.

8.4. Inclined Showers

Inclined showers are special in several aspects. First of all, inclined showers are hard to detect by traditional particle detector arrays since most of these detectors are optimized for showers arriving from zenith and are therefore naturally less sensitive to inclined showers. Furthermore the shower gets observed in a very late state of its development, since it has to pass more atmosphere before reaching the detector. This means that fewer particles reach the detector which in addition

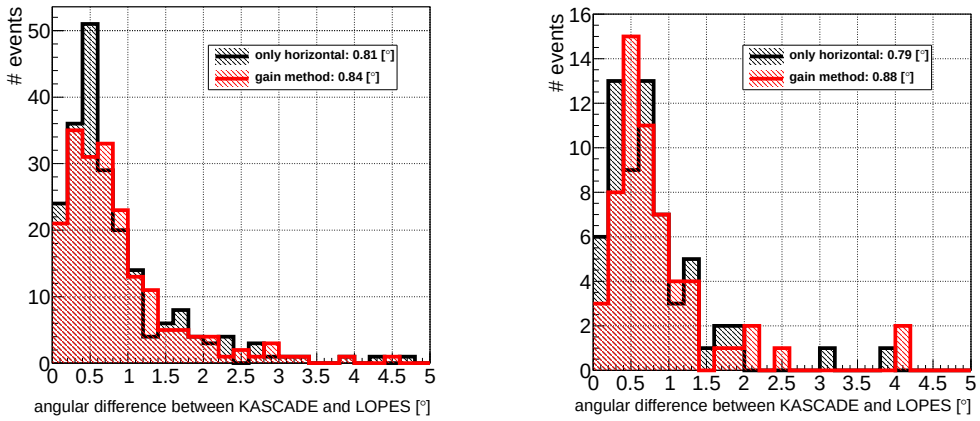

(a) (b)

Figure 8.13.: Angular difference for showers with zenith angles smaller than 45° between the KASCADE and LOPES reconstructed arrival direction for two different weightings of the reconstruction of the electric field vector for classic (left) and vectorial (right) beamforming.

makes it harder to detect these kind of showers.

8.4.1. Inclined Hadronic Showers

Inclined hadronic showers develop in the atmosphere far away from the detector. Except for muons most of the particles will be either absorbed in the atmosphere or low energetic. With ground based detectors, inclined showers will be observed in a late state of their development, see also figure 8.14. Nevertheless the electromagnetic waves generated during the shower development will not be attenuated. Thus detection techniques sensitive to the electromagnetic emission, such as fluorescence detectors or radio arrays, are preferable for the detection of inclined showers.

8.4.2. Inclined Neutrino Showers

Inclined showers are one good possibility to detect neutrinos. Since neutrinos have a low cross-section they need to pass more matter to interact. Thus, if an inclined shower is observed that has its maximum close to the detector it was most probably a neutrino induced air shower. This makes inclined showers ideal to look for neutrinos since they are better detectable and very well distinguishable from hadronic showers which will start much earlier in the atmosphere.

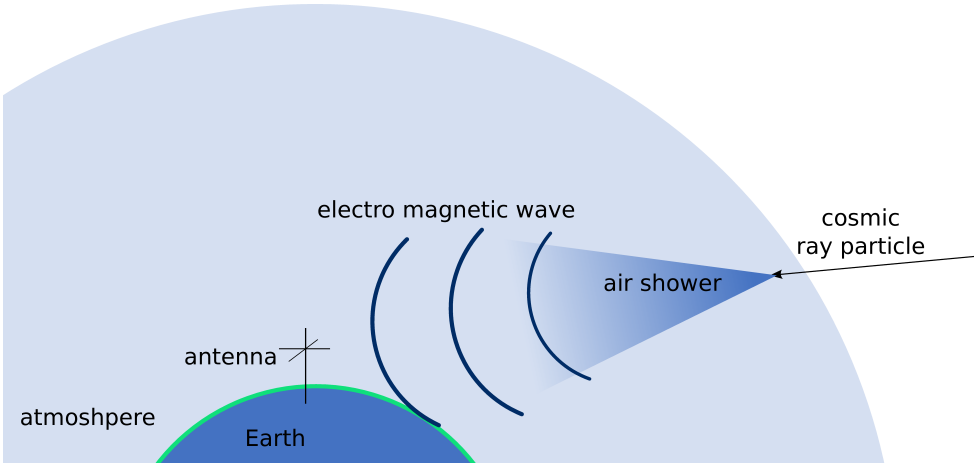

Figure 8.14.: Sketch of a cosmic ray interacting with the Earth's atmosphere and creating an inclined shower. The particle component of the shower is dying out whereas the electromagnetic wave propagates and can be detected by an antenna.

8.5. Radio Detection of Inclined Showers

The radio method is supposed to be suitable for detecting inclined showers because the radio signal is generated over the complete shower development and therefore it is in principle preferable to observe an air shower in a late state of development (as it is the case for inclined showers). The radio waves are not significantly attenuated when they traverse the atmosphere. However, compared to vertical showers a higher signal is expected in the vertical component for inclined showers. Naturally it is desirable to have antennas sensitive to the vertical component to achieve a high detection efficiency and high data quality for inclined showers. In the case of LOPES 3D this was realized by additionally measuring with vertically aligned antennas. This is the best way when having enough electronic channels available. Another possibility is to deploy only two antennas at each position. For this method at least one antenna has to be also sensitive the vertical component. The advantage of this method is that only two channels per station are occupied. The drawbacks however are:

- a higher background noise, since antennas sensitive to more components naturally record more noise,
- a not redundant measurement, see chapter 5.1,
- and lower data quality if the background noise is higher in the vertical component (as expected for anthropogenic noise).

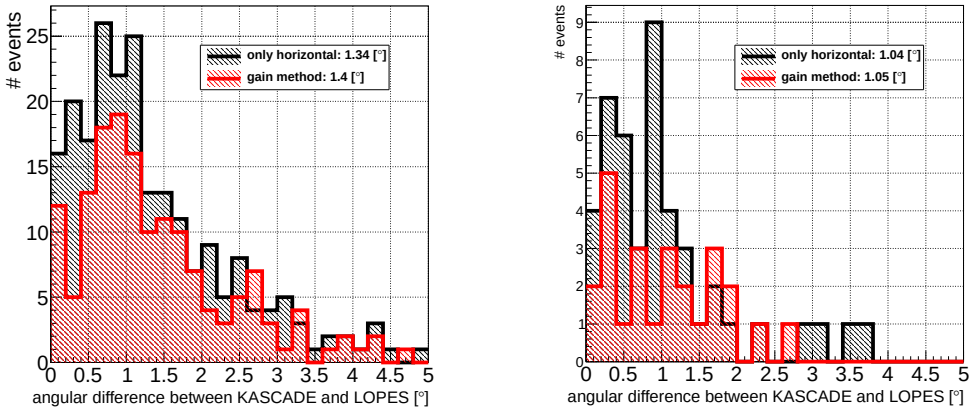

(a) (b)

Figure 8.15.: Angular difference for inclined showers between the KASCADE and LOPES reconstructed air shower arrival direction for two different weighting schemes of the reconstruction of the electric field vector for classic (left) and vectorial (right) beamforming.

Thus from the theoretical point of view, the only way to have good data quality for vertical showers and inclined showers at the same time is to measure with at least three antennas at the same place, as done in LOPES 3D.

8.5.1. Probing of the Weighting Factors on Inclined Showers

The different weighting factors described in section 8.3 have also been applied to reconstruct inclined events. The results are presented in table 8.1. In figure 8.15 the mean angular deviation for inclined showers from the KASCADE reconstructed direction is shown for showers reconstructed with two different weighting methods. The reconstructions using the other weighting schemes agree equivalently with the KASCADE-reconstructed direction within the uncertainties. The number of reconstructed events including measurements with vertically aligned antennas and using only horizontal antennas get more similar for the inclined dataset. This in addition with an increasing background noise in the vertical component, cf. section 8.5.3, is a hint that measurements with vertically aligned antennas are needed to achieve a high reconstruction efficiency for inclined showers. Nevertheless this is only feasible in regions with low man-made noise.

Table 8.1.: Overview on the reconstructed events using different methods to derive the electric field vector, for the the different event samples of the LOPES 3D recorded data. In this selection only events recorded before the increase in background noise are considered.

event sample	weighting method	reconstructed events	
		vectorial beam-forming	classic beam-forming
KASCADE-normal	former LOPES	44	54
	equal weight	31	34
	$\vec{v} \times \vec{B}$-method	32	30
	gain-method	34	43
	active antenna height	22	23
Grande-normal	former LOPES	34	101
	equal weight	41	83
	$\vec{v} \times \vec{B}$-method	42	97
	gain-method	35	101
	active antenna height	43	92
KASCADE-inclined	former LOPES	36	44
	equal weight	19	47
	$\vec{v} \times \vec{B}$-method	16	50
	gain-method	19	47
	active antenna height	21	47
Grande-inclined	former LOPES	6	22
	equal weight	10	19
	$\vec{v} \times \vec{B}$-method	8	13
	gain-method	5	20
	active antenna height	22	23

8.5.2. Efficiency for Inclined Showers

Defining an efficiency for the detection of inclined showers is challenging since the more inclined the showers get, the worse the reconstruction of KASCADE-Grande gets. One flawed parameter is the energy, thus the data set of KASCADE triggered inclined showers has to be considered separated into two parts. The first part contains showers with zenith angles smaller than 60° and larger than 45° the second contains showers with zenith angles larger than 60°. This separation was chosen since the energy reconstruction seems to be more trustful for the geometries with $\theta \leq 60^\circ$ see also chapter 4. Nevertheless the reconstructed energy is overestimated. Another issue for inclined showers is the declining efficiency of KASCADE-Grande and with this the loss of triggers. With the flawed energy reconstruction and the incalculable trigger efficiency it is impossible to give an estimation for the radio detection efficiency of inclined showers. Nevertheless the numbers of detected events in both samples can be regarded as lower limit for the detection efficiency of air showers via radio. In figures 8.16, 8.17, 8.18 and 8.19 the number of detected air showers for the former LOPES weighting and the different weighting schemes discussed above are shown in dependence of the zenith angle of the air showers. A general increase of the fraction of detected air showers can be observed for zenith angles up to 60°. The drop in the fraction of detected air showers for larger angles can be explained by the overestimation of the energy for these geometries, c.f. figure 4.10. With this more low energy events for which no radio signal is expected are in the selection which results in a lower fraction of reconstructible events.

8.5.3. Background noise

At the LOPES site the background noise is the limiting factor for the event detection in radio. This was already shown by the decrease of the event rate with the increase of background noise which was already discussed in chapter 4. Thus a detailed study of the background noise was done. The measurement with tripoles and the beamforming enable LOPES 3D to look for a direction dependence of the average and coherent noise in single components of the electric field vector. This is done by calculating the p-beam or CC-beam in a certain direction. With this, the antenna array gets sensitive in only this direction. The direction dependence of the average noise was determined by calculating the RMS value of the p-beam and is shown in figure 8.20 left. It can be seen that the noise in the two horizontal components more or less stays constant over the whole zenith angle range, whereas the noise in the vertical component increases with increasing zenith angle. This is expected since most of the man-made noise is arriving from

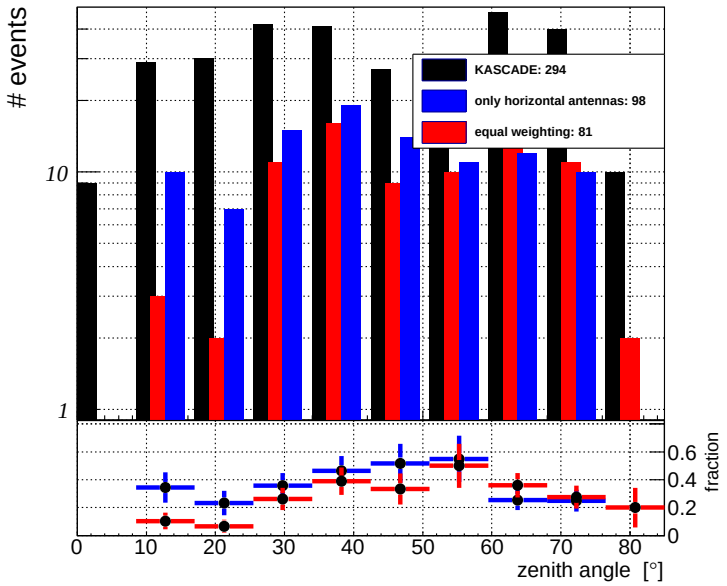

Figure 8.16.: Absolute amount of reconstructed events for KASCADE, black, the former LOPES weighting, blue, and equal weighting, red and the according fraction of reconstructed events.

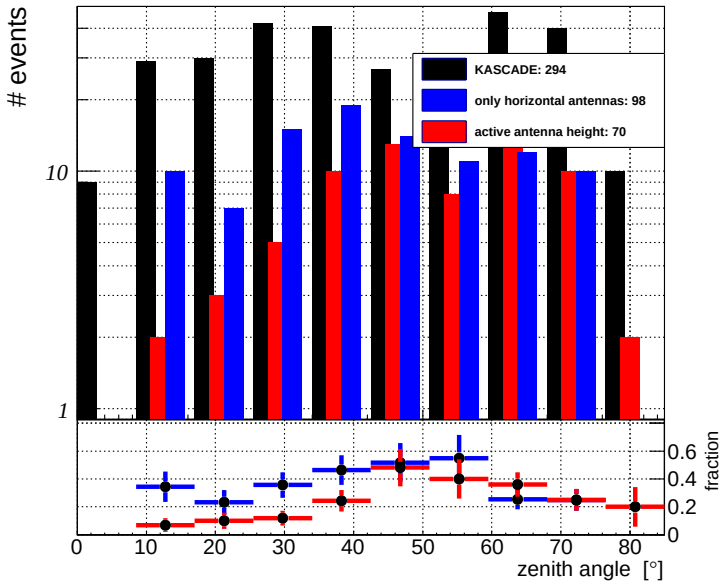

Figure 8.17.: Absolute amount of reconstructed events for KASCADE, black, the former LOPES weighting, blue, and the active antenna height, red and the according fraction of reconstructed events.

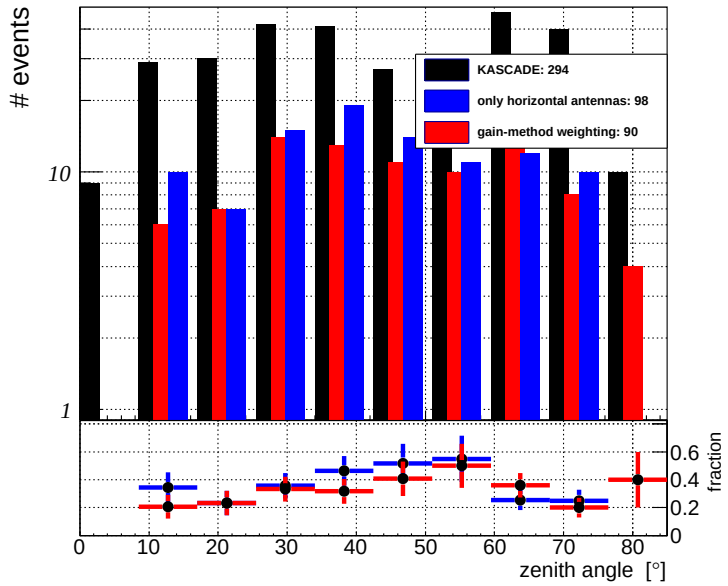

Figure 8.18.: Absolute amount of reconstructed events for KASCADE, black, the former LOPES weighting, blue, and the gain-method weighting, red and the according fraction of reconstructed events.

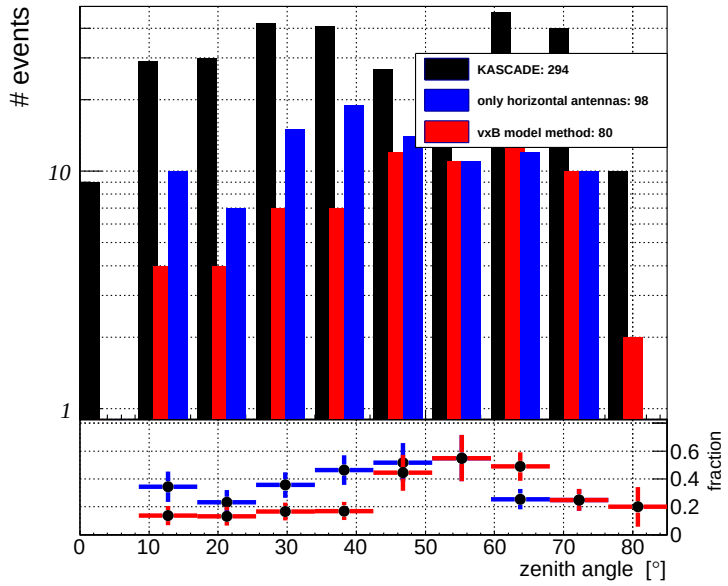

Figure 8.19.: Absolute amount of reconstructed events for KASCADE, black, the former LOPES weighting, blue, and the $\vec{v} \times \vec{B}$-method weighting, red and the according fraction of reconstructed events.

the horizon and is vertically aligned. On the right-hand side of figure 8.20 the zenith angle dependence of coherent noise is shown. This was derived by calculating the RMS of the CC-beam which was formed in the according direction. The coherent noise is also dependent on the zenith angle for the vertical polarization, whereas the two horizontal polarizations show no zenith angle dependence.

In figure 8.21 the reconstructed noise is shown when using only data from horizontal antennas for the calculation. It can be seen that the noise in the vertical component is not increasing. This in principle can have two reasons. Either the reconstruction using only data from horizontal antennas underestimates the noise in the vertical component or the selection containing data from all three antennas overestimates the noise in the vertical component.
In order to distinguish between these two possibilities the man-made radio background, also known as anthropogenic noise, has to be discussed. Anthropogenic noise is more prominent in the vertical component for several reasons.

1. The mean attenuation is weakest for the vertical polarization when propagating near ground (Rothammel, 1995). With this in general more noise is expected to be in the vertical component, independently of where it was generated.

2. Most man-made noise consists of signals that are emitted and need to be detected on ground. Thus, it is very desirable to have low attenuation during the propagation in order to gain high ranges with low emission power. This is realized when emitting in the vertical polarization.

3. For many applications an emission in all directions of the horizon is desired, this is the case for example for broadcasting stations. The only way to realize this is to use a vertically oriented dipole antenna or an antenna with similar emission patterns, cf. emission pattern of the vertical dipole shown in figure 3.14.

Thus, the noise dependency that is measured including the vertically aligned antennas is expected.
With this, it is proven that the horizontally aligned antennas get less capable to measure the vertical component the more inclined a shower gets. Otherwise the same dependence should be seen in the measurement with only horizontally aligned antennas. This is also supported by the simulated gain pattern for horizontally aligned antennas which has in general low sensitivity to the vertical component.

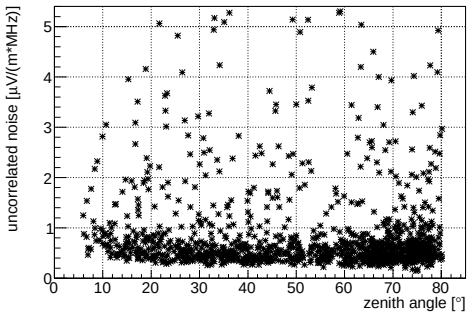

(a) Average noise in the north-south component of the electric field vector.

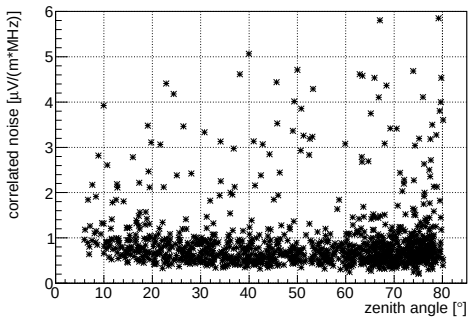

(b) Coherent noise in the north-south component of the electric field vector.

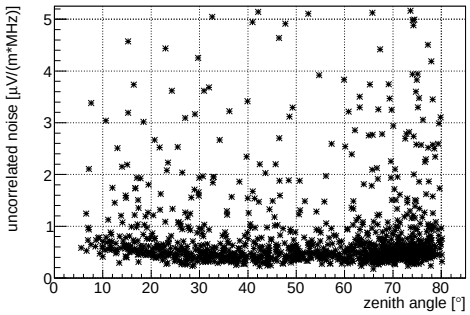

(c) Average noise in the east-west component of the electric field vector.

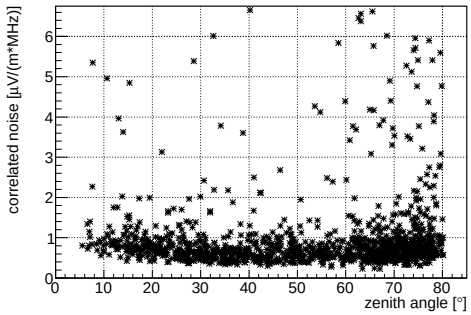

(d) Coherent noise in the east-west component of the electric field vector.

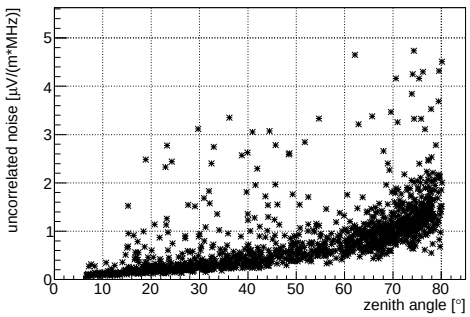

(e) Average noise in the vertical component of the electric field vector.

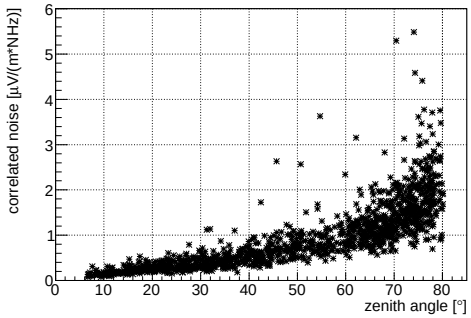

(f) Coherent noise in the vertical component of the electric field vector.

Figure 8.20.: Zenith dependence of the background noise (left) and coherent background noise (right) in the different components (north-south top, east-west middle, vertical bottom). For the north-south and east-west component no dependence can be seen whereas the vertical component the background noise is correlated with the zenith angle.

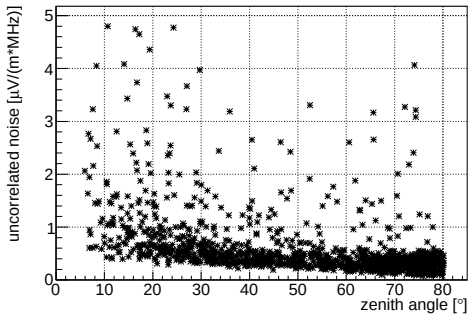

(a) Average noise in the north-south component of the electric field vector.

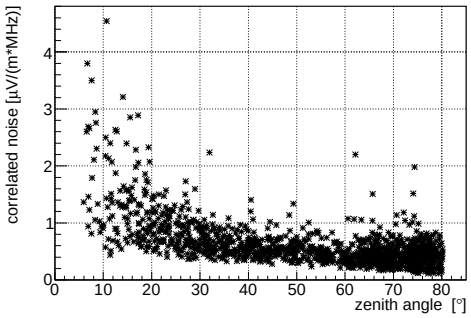

(b) Coherent noise in the north-south component of the electric field vector.

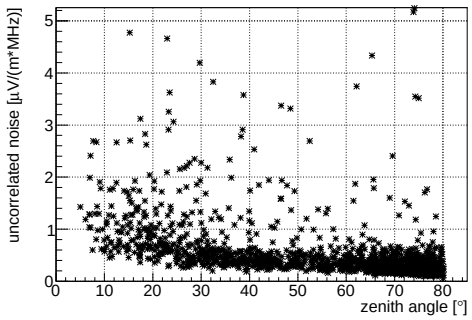

(c) Average noise in the east-west component of the electric field vector.

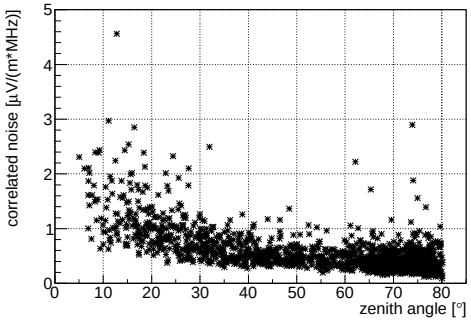

(d) Coherent noise in the east-west component of the electric field vector.

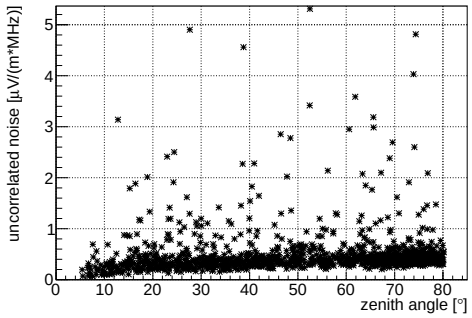

(e) Average noise in the vertical component of the electric field vector.

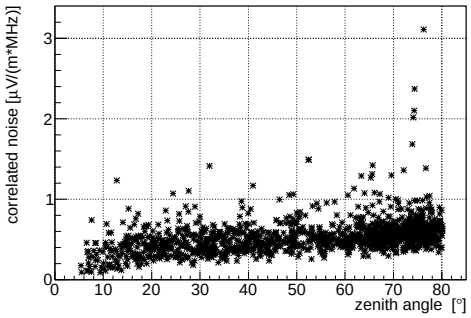

(f) Coherent noise in the vertical component of the electric field vector.

Figure 8.21.: Zenith dependence of the "flawed" (i.e. reconstructed with only horizontal antennas) background noise (left) and coherent background noise (right) in the different components (north-south top, east-west middle, vertical bottom).

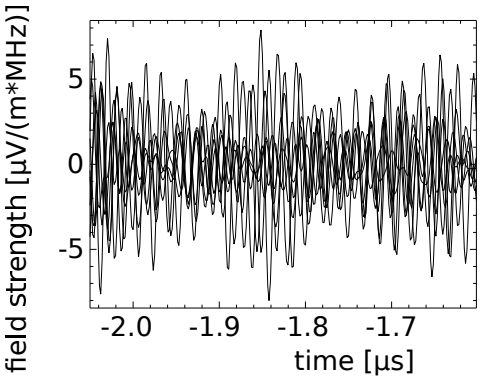

(a) Vertical components of the electric field vector as a function of time.

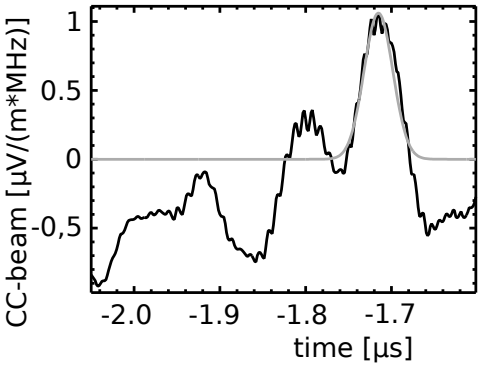

(b) CC-beam in black and Gaussian fit in grey for the vertical component.

Figure 8.22.: Vertical components of the electric field vector reconstructed using only horizontally aligned antennas for an air shower with a zenith angle of 65.6° and an azimuthal angle of 208.6°.

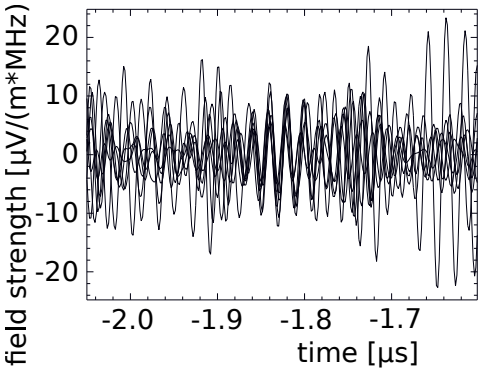

(a) Vertical components of the electric field vector as a function of time.

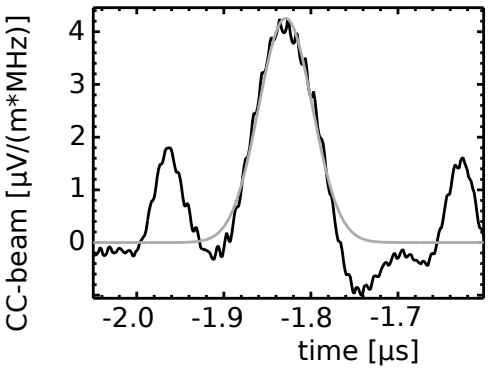

(b) CC-beam in black and Gaussian fit in grey for the vertical component.

Figure 8.23.: Vertical components of the electric field vector reconstructed using the gain-method for an air shower with a zenith angle of 65.6° and an azimuthal angle of 208.6°.

8.6. Example Events With Zenith Angles $\theta \geq 65^\circ$

The fractions of reconstructed showers did not significantly improve for inclined events when taking into account measurements with vertically aligned antennas. This was not expected. Thus, the functionality of the vertically aligned antennas has to be probed. We do this by looking at two inclined showers exemplarily. The first shower hit KASCADE with a zenith angle of 65.6° and an azimuthal angle of 208.6°. The energy of the primary particle was estimated to $10^{17.6}$ eV by the KASCADE reconstruction. Note that the reconstruction is not accurate

for these zenith angels, cf. chapter 4. In figures 8.22(a) and 8.23(a) the vertical components of in total 7 reconstructed electric field vectors are shown as a function of time. The electric field vectors shown in figure 8.22(a) were reconstructed using only data from horizontally aligned antennas. No coherent signal is observed which is also indicated by the corresponding CC-beam which is shown in figure 8.22(b). Here the peak in the CC-beam is low and not at the expected time. In figure 8.23(a) the vertical components of the electric field vectors of the same event are shown. These electric field vectors were reconstructed including measurements with vertically aligned antennas, more precisely the gain-method weighting was used. A coherent signal is observed at the expected time which is also indicated by the corresponding CC-beam which is shown in figure 8.23(b). A higher peak at the expected time is observed. This is similar for all weighting schemes including vertically aligned antennas except the active antenna height. The higher noise when including measurements with vertically aligned antennas can be seen nicely by looking at the time traces.

The second event which is discussed here is one of the most inclined events in this selection. The air shower arrived with a zenith angle of 76.7° and an azimuthal angle of 199.4°. The energy of the primary particle was (over-)estimated to $10^{18.4}$ eV by the flawed KASCADE energy reconstruction. This event can only be detected in radio when the vertically aligned antennas are considered. In figures 8.24(a) and 8.24(b) the vertical components of the reconstruction using only horizontally aligned antennas are shown. Again no coherent part can be observed. But, when incorporating the measurements with vertically aligned antennas, this event can be detected in radio see figures 8.25(a) and 8.25(b). Here a coherent part and a peak at the expected time can be observed. The weighting scheme again was the gain-method. Also for this event all weighting schemes including vertically aligned antennas except for the active antenna height give qualitatively the same results.

8.7. Conclusion

In this chapter the benefits of the additional measurements with vertical aligned antennas at LOPES were discussed, for regular, $\theta \leq 45^\circ$, and inclined, $\theta \geq 45^\circ$, showers. Furthermore we developed and discussed several weighting schemes for the redundant measurement of the electric field vector.
For the regular dataset the best results are achieved when using only data from horizontal antennas. This is supported by geometric considerations as well as the measured background noise.

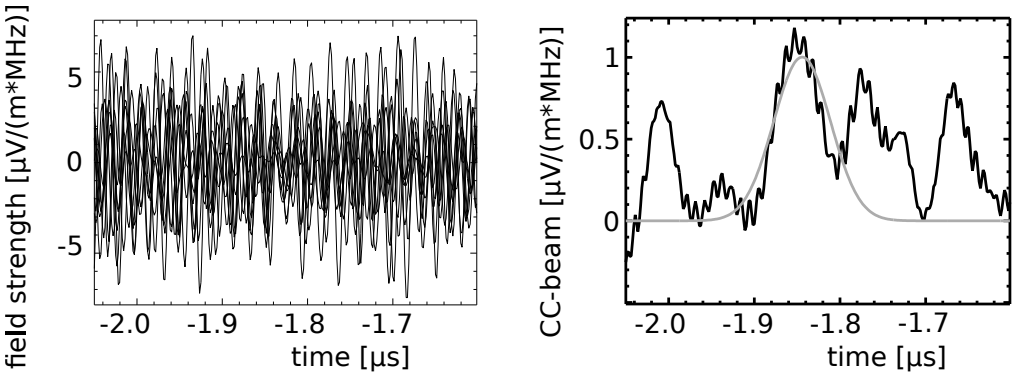

(a) Vertical components of the electric field vector as a function of time.

(b) CC-beam in black and Gaussian fit in grey for the vertical component.

Figure 8.24.: Vertical components of the electric field vector reconstructed using only horizontally aligned antennas for an air shower with a zenith angle of $76.7°$ and an azimuthal angle of $199.4°$.

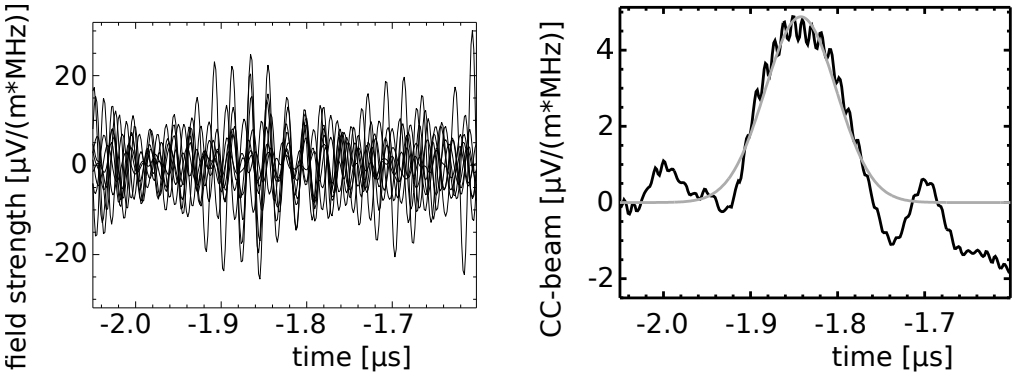

(a) Vertical components of the electric field vector as a function of time.

(b) CC-beam in black and Gaussian fit in grey for the vertical component.

Figure 8.25.: Vertical components of the electric field vector reconstructed using the gain-method for an air shower with a zenith angle of $76.7°$ and an azimuthal angle of $199.4°$.

For inclined showers, however, the measurement with vertically aligned antennas did not deteriorate the number of reconstructed events. But also no significant improvement was found. The higher background noise and the similar numbers in reconstructed events are hints that the measurements with vertically aligned antennas get more important for inclined showers. Nevertheless, the functionality of measurements with vertically aligned antennas was demonstrated exemplarily. The additional measurement with vertically aligned antennas did not have the desired benefits for LOPES. This is because of the weak emission in the vertical component and the zenith angle dependence of the background noise which was measured with LOPES for the first time in each component separately.

CHAPTER 9

Conclusions and Outlook

The radio detection of cosmic rays is a promising alternative technique which offers sensitivity to the shower development in combination with a high uptime. Thus the radio detection technique is developed with large effort. The aim of this work was to check the benefits of additional measurements with vertical antennas. In an earlier work (Huber, 2010) the LOPES antenna array was reconfigured and equipped with tripole antennas. Within this thesis the analysis of the data taken with this new setup was developed and conducted and a detailed calibration of the array was performed. Several aspects were analysed and proven within the present work.

- The tripole antenna was calibrated in great detail and the data taken with LOPES 3D was tested successfully for consistency. Within the amplitude calibration a method to calibrate electronic channels connected to vertical antennas was developed and checked. Furthermore an alternative and frequency dependent delay calibration was derived.

- It was shown that LOPES 3D is sensitive to galactic plane transit. Although LOPES is located in an industrial like radio loud area the periodicity of the galactic transit was clearly visible in the recorded data.

- The gain application in the analysis software was updated to work vectorially and to reconstruct the electric field vector with only two pairs of antennas. Thus, for each tripole station the electric field vector can be reconstructed three times. Several weighting schemes, depending on the arrival direction, have been developed to achieve the best combination of the three vectors.

These schemes have been tested on the reconstruction efficiency and accuracy. It was found that for air showers arriving with zenith angles smaller than 45° only using horizontally aligned antennas gives the best results. For inclined showers more signal is expected to be in the vertical component. However this could not be proven by data for several reasons. At the KIT where LOPES 3D was built there is in general a high background noise level. Thus, the detection of air shower radio signals is very challenging even in the preferred east-west component. The background noise in the vertical component was found to increase with the zenith angle. Consequently, taking into account measurements with vertically aligned antennas did also not improve the reconstruction of inclined showers with LOPES 3D.

- The rate of reconstructible radio air shower signals significantly decreased, which was found to be correlated to an increase in the radio background noise. With this in total 10 months of unbiased data could be recorded with LOPES 3D.

- An analysis was developed to analytically calculate the charge excess contribution in a single measured electric field vector. This analysis was applied on a suitable selection of measured electric field vectors. Although the data quality of LOPES 3D is rather low hints for a $\approx 10\%$ charge excess contribution were found.

- The cross-correlation beamforming was updated to work on the complete electric field vector and not only one component. This was found to have in general no advantage over the beamforming in single components, as there is not always a signal in all components expected. Nevertheless, in some cases the vectorial beamforming is superior. A successfully reconstructed event using the vectorial beamforming implies a detection in all three components, which is a much stronger condition than a detection in a single component. Nevertheless the vectorial beamforming can be improved by giving different components different weights. This goes beyond the scope of this work but might be of interest if beamforming and more precisely vectorial beamforming is considered in future experiments.

- The measurement with vertically aligned antennas is supposed to be suitable for the measurement of inclined showers. This was shown using model calculations and tested against data. Nevertheless, the rate of reconstructed events when including measurements with vertically aligned antennas does not show much improvement in data. Thus, measurements with vertically aligned antennas should be avoided, at least for noise situations like at the LOPES site.

- A study on the background noise in the different components was done for the first time in LOPES. It was found that, as expected, the vertical component shows a dependence on the zenith angle. This is supported also by theory, since the vertical component for signals that propagate near ground is less attenuated than the horizontal component. Furthermore most anthropogenic noise is vertically polarized.

- It was shown, using model calculations, that in order to reach a full sky coverage with radio, measurements with three antennas per station are necessary.

The reconfiguration of LOPES was necessary for the desired study on the additional measurements with vertical antennas. LOPES 3D was a test setup, thus, the antenna type was chosen to have a homogeneous sensitivity. With this the horizontally aligned antennas got more sensitive to signals from the horizon which caused them to record more noise. This and the reduction of the positions reduced the data quality compared to former setups of LOPES. Nevertheless, the radio signal of air showers could be detected and analysed in all three components. The derived results will have a significant impact on future efforts in the radio detection of cosmic rays. For future efforts radio measurements should be performed in radio quiet areas, this is of high importance especially for the vertical component, as here high noise is present and for most of the geometries only a weak signal is expected. For inclined showers the vertical component generally increases according to the $\vec{v} \times \vec{B}$-model but stays the weakest component. The detection of inclined showers is possible and thus radio so far is the only technique capable of measuring the electromagnetic component and the shower development of inclined showers. If combined with a existing particle array the radio technique can significantly increase the statistic and provide a high data quality also for inclined showers. The ground dependence of the gain pattern is a serious issue when it comes to inclined shower detection. To minimize the uncertainties either antennas that depend only weak on the ground conditions have to be used, or the ground conditions have to be monitored and regarded in an offline data analysis. The gain pattern of a deployed antenna should be measured in the field very detailed and precisely to estimate the quality of the gain pattern simulations. If the gain pattern is well understood and a site with convenient noise conditions is found, the radio technique and especially the vertical component can significantly increase the statistic and quality of detected air showers.

APPENDIX A

Lightning detection with LOPES

In this chapter the influence of high atmospherical electric fields on air showers and mutual interactions between air showers and lightnings are discussed. Most of this chapter has already been published by the author in reference (Apel et al., 2011a). The aim of such studies is that by knowing the influence of electric fields on the radio emission in EAS the radio signal recorded during extreme weather conditions can be corrected for and therefore these periods are not lost for the analysis. This could lead to an uptime for the radio detection technique close to 100%, which is important as the flux of high-energy cosmic rays is very low. For the time being the atmospheric monitoring is used as veto for the standard operation of radio antenna arrays such as LOPES.

A.1. Atmospheric Electric Field during Thunderstorms

The exact measurement of the atmospheric electric field with a high time resolution is very important to provide information for the radio detection of cosmic ray induced air showers. The radiation in the radio regime is emitted by the propagating electrons and positrons of an air shower mainly due to their time dependent spatial (charge) separation in the Earth's magnetic field. The atmospheric electric field has an influence on the propagation of the charged particles of the shower and therefore on the radio emission. Only knowledge of the field allows detailed

studies of the influence of the atmospheric electric field on the radio emission.

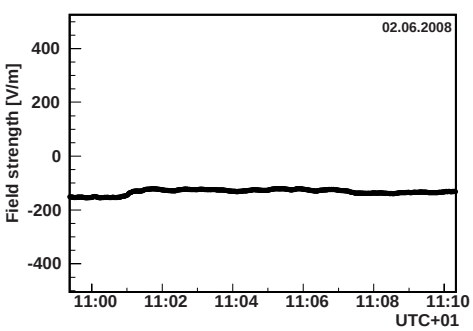

(a) Electric field measured by an electric field mill during fair weather conditions

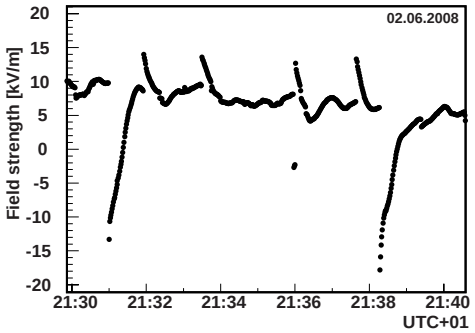

(b) Electric field measured by an electric field mill during a thunderstorm, where discontinuities and jumps in the electric field strength are seen. In addition, a much higher field strength than during fair weather is measured

Figure A.1.: Two examples of the electric field measured by an electric field mill.

To measure the atmospheric electric field a field mill is used. With such a device it is possible to record the vertical electric field between the lowest cloud layer and the ground. The electric field strength gives clear evidences whether there are fair weather conditions or a close thunderstorm.

During fair weather conditions, the atmospheric electric field experiences only small changes between -100 and $-200\,\mathrm{Vm}^{-1}$. The amplitudes increase when rain clouds cross over but the changes are on large time scales. During thunderstorms the field strength can reach values up to $\pm 20\,\mathrm{kVm}^{-1}$ and there are sudden changes in the electric field occurring on a very short time scale, see figure A.1.

A.2. Influence of Atmospheric Electric Fields on Radio Detection of EAS

An additional or strongly varying atmospheric electric field can lead to different strengths and geometries of the radio emission from charged particles, in particular secondaries from a cosmic-ray air shower in the Earth's atmosphere (Buitink S. et al., 2007; Buitink et al., 2010). In figure A.2, this effect is shown schematically. The electric field in thunderclouds, especially within the convective region, can reach values up to $\pm 100\,\mathrm{kVm}^{-1}$. With radio antenna arrays, like e.g. LOPES,

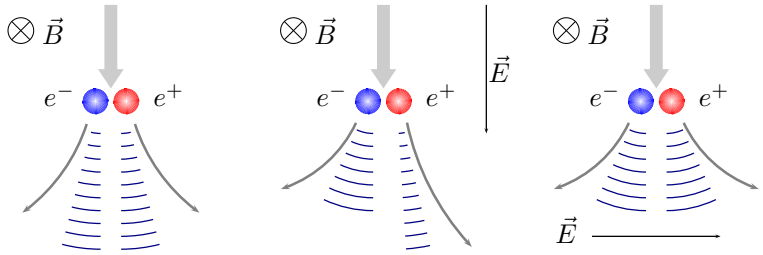

Figure A.2.: Scheme of the influence of an additional electric field on the electrons and positrons of an air shower. On the left hand side no additional electric field is shown. In the middle, an electric field parallel to the direction of the air shower is shown which leads to an acceleration of the positrons and a deceleration of the electrons. On the right hand side, an electric field which is perpendicular to the shower direction is shown which results in a stronger deflection of the electrons and positrons (from reference Buitink S. et al. (2007)). A simulation study showed that electric fields that are perpendicular to the shower axis have an influence on the transverse currents and thus on the $\vec{v} \times \vec{B}$-dependent emission electric fields that are parallel to the shower axis have an influence on the Askaryan emission (Gelb, 2012).

this effect can be seen in the observation of cosmic rays by recording an amplified or weakened radio signal during thunderstorms and extreme weather conditions. In order to detect a thunderstorm a field mill has been installed at the LOPES site (Nehls, 2008) serving as a monitoring and veto device for the LOPES analysis. One example of such an amplification can be seen in figure A.3 where two events with very similar shower geometry and primary energy are shown. The first event was recorded during fair weather conditions with no observable radio signal in the trace which should occur at about -1.8 μs. This is expected for the low estimated primary energy by KASCADE-Grande observations of $5.4 \cdot$ 10^{16} eV. The incoherent signal starting at $-1.75\,\mu$s is assigned to detector noise from the KASCADE particle detectors. This air shower arrived at the KASCADE array with $\phi = 110.39\,^\circ$ and $\theta = 31.5\,^\circ$, where ϕ is the KASCADE reconstructed azimuth of the shower direction and θ the zenith angle. The second event is an air shower with $\phi = 110.35\,^\circ$ and $\theta = 32.1\,^\circ$ and an even lower energy estimated to $4.3 \cdot 10^{16}$ eV. The average distance of the antennas to the shower core is also in the same order for both events. In the time trace of this event a coherent radio pulse at -1.8 μs is observed, but for that energy no radio signal is expected. The most likely explanation for such a clear detection is the amplification of the EAS radio signal in the strong electric fields of the thundercloud present at that time.

The energy threshold for triggering LOPES by KASCADE-Grande is lower than the possible detection threshold ($5{\cdot}10^{16}$ eV) at the site of LOPES with its industrial environment and high noise level. Because of that only in a small fraction of the triggered events a radio pulse can be observed. In a fraction of $(0.96 \pm 0.12) \cdot 10^{-2}$

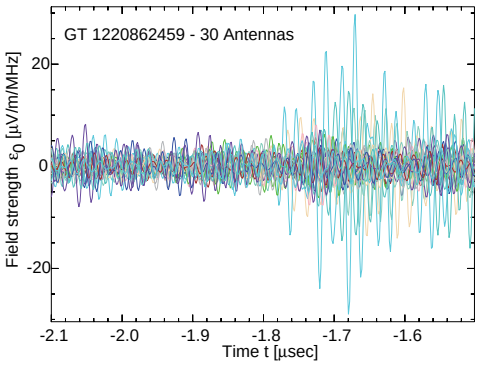

(a) Time traces of an event recorded during fair weather conditions, where no coherent signal can be seen. The increase in some of the traces starting at $-1.75\,\mu$s is assigned to detector noise from the KASCADE particle detectors.

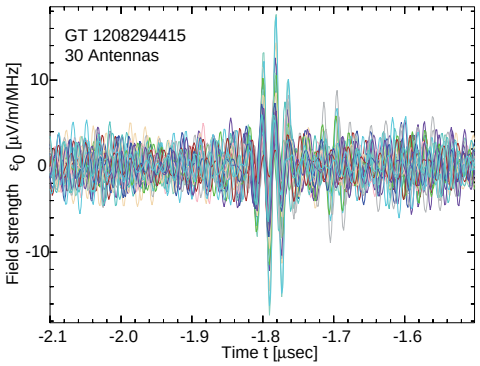

(b) Time traces of a similar event which was recorded during a thunderstorm. The amplified coherent signal from the direction of the air shower at $-1.8\,\mu$s is clearly visible.

Figure A.3.: Bandwidth normalized field strength in μV/m/MHz vs. time in μs for two events with similar geometry and primary energy.

of the events recorded during fair weather conditions a coherent radio signal has been seen. In 2007, 2008 and 2011 roughly three full days of data were recorded during periods of thunderstorms. Because of these low statistics only few such corresponding fair weather - thunderstorm partner events could be analysed. But the fraction of events that were recorded during thunderstorms and that show a coherent signal of $(2.39 \pm 0.27) \cdot 10^{-2}$ is about a factor two to three higher than in fair weather conditions. This results in 134 events that are recorded during thunderstorms having a cross-correlation beam above threshold. This is considered as a clear indication that strong atmospheric electric fields during thunderstorms have an influence on the radio emission of cosmic ray air showers and might more likely amplify the signal than attenuate it. For smaller atmospheric electric fields there might be no big effect (Buitink S. et al., 2007) but investigations have shown that strong atmospheric electric fields without thunderstorm that can occur in rain clouds also have an influence on the radio emission but the number of events recorded during such conditions are even lower (Ender, M. et al., 2009).

A.3. Radio Background during Thunderstorms

The beacon, cf.chapter 3.4, emits constant sine waves at 63.5, 68.1 MHz and (since end of 2010) 53.1 MHz which form a considerable background of the measurements during fair weather. During thunderstorms the general ambient background is much higher and in addition radio signals from lightning strikes contribute to the background. In figure A.4 two average background frequency spectra are shown. The upper spectrum was recorded during fair weather conditions. The narrow band noise and the peaks of the beacon signals are clearly seen. The lower part of the figure shows a spectrum taken during thunderstorm conditions. Here, the beacon signals and other narrow band noise sources can hardly be identified over the high broadband radio emission. As the beacon signals are buried in background noise in such periods the recorded events cannot be analysed.

Another aspect that makes it impossible to analyse individual events is the fact that the sensitive electronics needed to observe the weak radio signals from cosmic-ray air showers are saturated by the strong signals from lightnings.

A.4. Problem of Lightning Initiation

One of the most extreme weather conditions mankind can think of are thunderstorms and lightning. Although these appearances are known for a very long time and have been the focus of many studies, the mechanism that leads to the final electric breakdown is still not well known. The field strengths of the electric fields in thunderclouds are large, but too small for a classic breakdown. One mechanism that could explain how a breakdown can happen with smaller electric field strengths are relativistic runaway electron avalanches (RREA). These RREA occur at a certain critical field strength when the cross-section of the electron-electron interaction gets smaller which leads to ionization losses that are smaller compared to the energy gain at the critical field strength. This results in a net energy gain of the electrons and an increasing number of electrons. This is because the electrons coming from the ionization are also accelerated and again produce new unbound electrons. This mechanism can only take place when the number of unbound electrons that can be accelerated, the seed electrons, is high enough within the strong electric field of a thundercloud. A source that can provide these seed electrons are cosmic ray induced air showers. During an air shower development up to 10^6 electrons and positrons can be generated on a very limited area, which is the location of the shower maximum, typically in a height of 3-8 km above sea level. These particles are then accelerated in the strong electric field

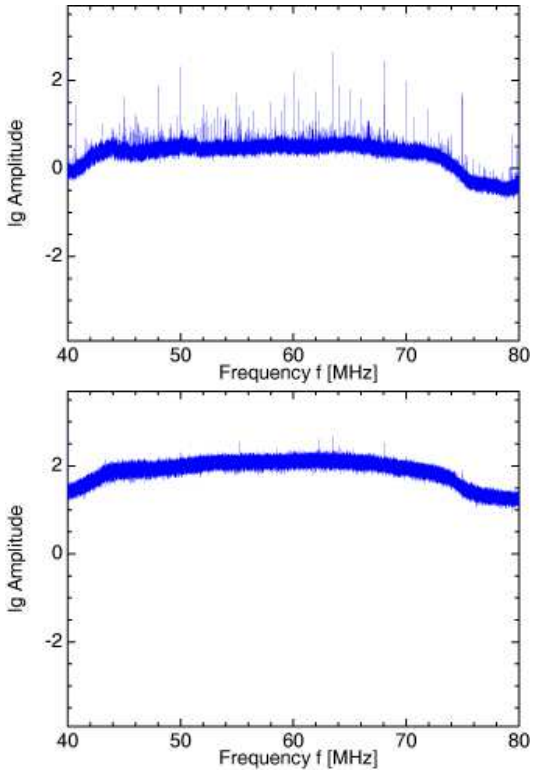

Figure A.4.: Logarithm of the mean amplitude of background frequency spectra in arbitrary units. Top: Background spectrum recorded during fair weather conditions, where a lot of narrow band noise sources are observed as small peaks. Bottom: Background spectrum recorded during a thunderstorm. The much higher broad band background level exceeds nearly all narrow band noise peaks including the beacon signals needed for the event-by-event time calibration.

of the thundercloud and lead to an RREA which results in a breakdown, called RRB, relativistic runaway breakdown. So, cosmic rays could be the initiator for lightning by providing the seed electrons for an RREA (Dwyer, J. R., Uman M. A., and Rassoul H. K., 2009).

A.5. Radio Signal from Lightning Strikes

The jumps and discontinuities in the electric field are clear evidence for thunderstorms and are used at LOPES to change the data acquisition into the so-named thunderstorm mode (Nehls, 2008). During this special mode the recorded time

traces are roughly eight times longer than the usual 0.82 ms and 6.55 ms of data taken for each triggered event, where the pre-trigger time of 0.41 ms remains the same. This is done to be able to look for temporally extended lightning signals in the recorded traces visible after the EAS signal, see an example in figure A.5. A discharging process like a lightning is always accompanied by strong electric fields in thunderclouds and always emits broadband electromagnetic radiation (Rakov, 2005). The radiation can be observed in the radio regime over long distances with antenna arrays originally designed to detect the radio emission from cosmic-ray air showers. The time structure of the signal can be very different depending on the distance and the nature of the discharging process. Figure A.5 shows a lightning signal recorded by all antennas of the LOPES array.

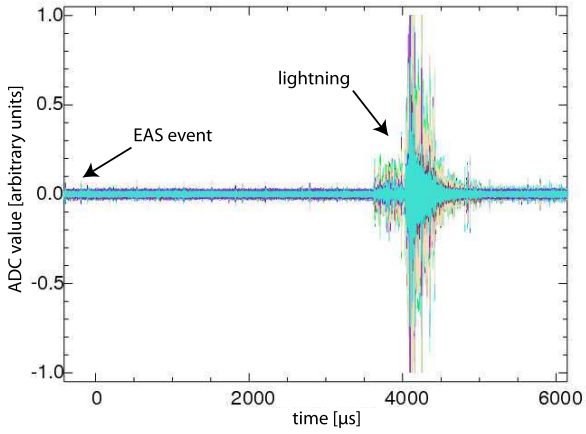

Figure A.5.: Example of time traces of the 30 LOPES antennas recorded in the thunderstorm mode for a KASCADE triggered air shower. The cosmic ray event triggering the readout is visible as small peak in the beginning of the traces. In this particular event a lightning strike occurs approximately 4 ms after the EAS. Structures in the radio emission of this lightning are very nicely resolved in all 30 antennas.

Discharges located in clouds with altitudes between 5 and 20 km above sea level can produce very short and strong pulses that are described as narrow bipolar pulses by (Gurevich and Zybin, 2004). It is an interesting question to investigate if such short pulses seen in figure A.5 just in front of the large emission from the lightning strike are generated by relativistic runaway breakdowns (RBB) and if such RRB's are always present at the initiation of lightning strikes.

Discharges within or between clouds or from cloud to ground result in signals that last longer than RRBs or EAS signals (see figure A.5). This gives us the possibility to calculate the CC-beam for many successive time slots and in every direction of the sky and to combine them into a skymap. Typically the cross-

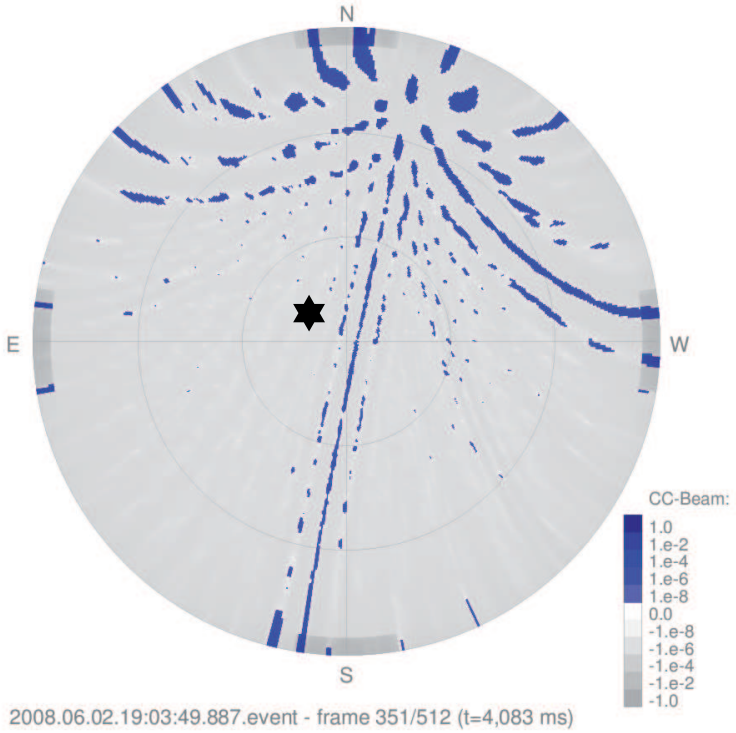

Figure A.6.: This figure shows a skymap of a lightning recorded with LOPES, where for each cell the amplitude of the cross-correlation beam is displayed. The whole sky is shown with the zenith in the center of the plot and the horizon at the edge. The lightning can bee seen as the strong signal in the North-Northwest (circle). The signals spread over the whole sky are due to the grating lobes of the antenna array which is a well understood artifact of skymapping in astronomy and only depends on the geometry of the antenna positions on ground. The event corresponds to the traces shown in figure A.5 and the star assigns the location of the detected EAS in this event.

correlation beam is used, since the signal from lightning strikes is coherent, but if desired also the power beam (averaged power of all antennas in a certain direction) is used to generate the skymap. By this procedure the lightning development is observed and the location of origin, the type and the direction of the lightning is reconstructed. For the principles of lightning observation using radio interferometers see also (Rhodes, C. T., Shao X. M., Krehbiel P. R.,Thomas R. J., and Hayenga C. O., 1994). For example the lightning strike displayed in figure A.6 (which corresponds to the time traces shown in Figure A.5) is a cloud-to-cloud lightning as the track does not reach the horizon. This example shows the capabilities of EAS radio antenna arrays to investigate in detail the radio emission from individual lightning discharges.

A.6. Correlations of EAS and Lightnings

To study the possibility of cosmic rays causing lightning strikes there are two correlations to investigate, the temporal and the spatial connections of air showers and lightning.

To investigate the temporal correlation, at LOPES a lightning is detected by the electric field mill, where a jump in the electric field corresponds to a discharge process. If cosmic-ray air showers induce these lightning strikes they should be observed by KASCADE-Grande or LOPES shortly before the lightning. In figure A.7, the time differences between jumps in the electric field with detected cosmic ray events is shown. The time binning of one second is determined by the time resolution of the electric field mill used at the LOPES site. In order to systematically investigate introduced uncertainties, similar plots with same dataset but artificially introduced time delays to scramble the possible correlation were produced. These studies resulted only in statistically insignificant enhancements at $t_{diff} = 0$.

The time resolution of the electric field mill is too low for such an analysis, but is high enough to determine whether there is a thunderstorm or not. To see a time correlation between cosmic-ray air showers and lightnings, a better time resolution is necessary. This can be provided by LOPES, but the statistics for such an analysis is still too low at LOPES. In addition, the area where EAS can be detected is much smaller than the sensitive area for lightning strikes, which also worsen the search for time correlations.

A more promising correlation study between cosmic rays and lightning is the search for a combined spatial and temporal correlation. To study this it is essential to detect lightnings with a high spatial resolution and to detect cosmic-ray air showers with a high efficiency and also a good spatial resolution. For the lightning detection a LOPES like array can be used as a combined lightning mapping and EAS detection array. The direction of the lightning can be determined by calculating the cross-correlation beam in every direction of the sky. A calculated skymap is shown in figure A.6, where an intracloud discharge can be seen. A star marks the direction of the air shower arriving shortly before the lightning. In this event and also in others no correlation could be observed. To improve the search for spatial correlations a better detection of the lightning and especially the lightning development is needed. Not only the direction where the lightning happened is of interest but also the path of the lightning and whether a cosmic-ray air shower passed there at the start of the lightning or somewhere near. The path of the air shower can be observed very well and reconstructed with KASCADE-Grande and LOPES. The development of the lightning is difficult to reconstruct with the given instruments since LOPES was not designed for that kind of studies and still the covered area is too small.

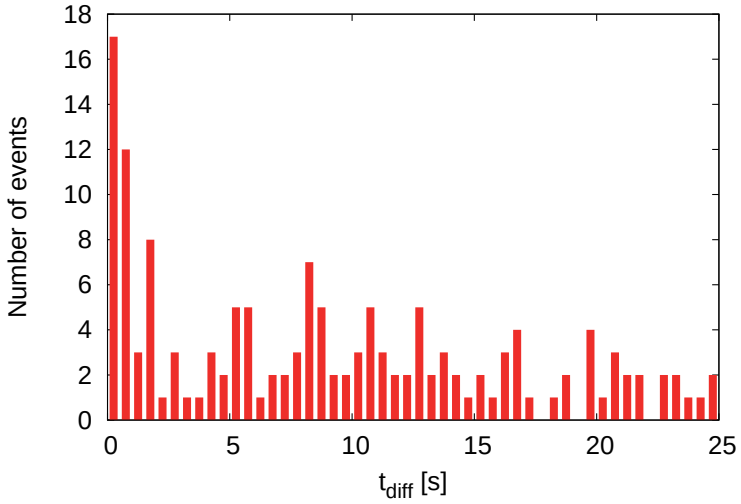

Figure A.7.: Time correlation between lightning and air shower events. Shown is the time difference between cosmic-ray event and lightning, where the lightning is detected by an electric field mill.

A.7. Further Investigations Using kHz Antennas

Along with the measurements of the MHz signals also some efforts were done in the kHz frequency band were undertaken. At the LOPES site there were three kHz antennas installed to investigate air shower radio emission in the kHz range (Link, 2009). These antennas were reactivated to measure lightning strikes (Braun, 2011). A lightning strike is a discharge process that appears on large scales and therefore has a huge amount of power emitted in the kHz range.

A.7.1. Experimental Setup

The three kHz antennas are loop antennas and thus sensitive to the magnetic component of radio emission. They are oriented in all three polarization directions and designed as active antennas. After receiving the signal is transmitted via 100 m long coaxial cables to the filters in which the signals are filtered from 50 to 500 kHz. After filtering the signal is recorded with a trace length of 150 ms. In contrast to air shower radio emission the radio emission from lighting strikes is much higher, therefore the dynamic range was adapted to a maximum input voltage at the ADC of 10 V. In order to compare and study lightning also a commercial lightning detection system has been installed at the LOPES site. The reconstruction algorithm of these station is not public therefore the received spa-

tial resolution has to be handled with care and no real error estimation can be performed.

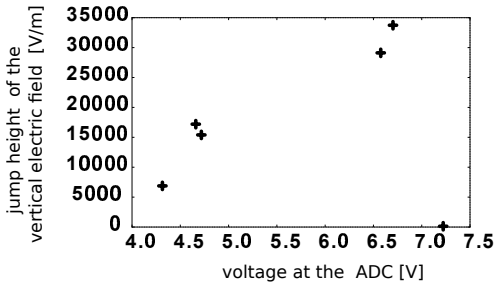

(a) Height of the jumps in the recorded vertical electric field over the peak height of signals recorded with the kHz antennas.

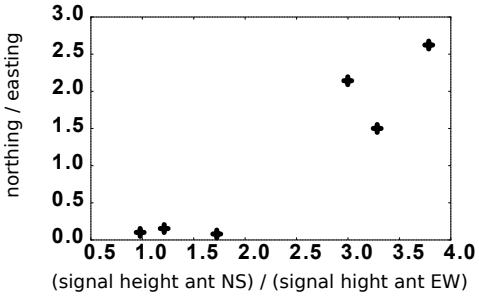

(b) Correlation between distance and peak height ratio of detected lighting strikes.

Figure A.8.

A.7.2. Detected Lightning strikes

During the operation of the kHz antennas in thunderstorm mode in total six lightning strikes could be detected with both, the commercial system and the kHz antennas. These strikes occurred at large distances from the array and therefore were only seen in the kHz antennas. For the kHz antennas there is no absolute calibration available, therefore only ratios or tendencies can be analysed. In figure A.8(a) the correlation with the height of the jump in the electric field mill is shown. As expected most of the lightnings correlate in amplitude with the jump height of the electric field mill. Only one strike was not detected by the electric field mill which can be explained by a cloud to cloud lightning in the upper cloud layers which will not affect the horizontal electric field measured by the electric field mill, since the electric field mill is only sensitive between lowest cloud layer and ground. In figure A.8(b) the ratio of the distance in north and the distance in west is plotted over the ratio of signal height in the north-south oriented antenna and the east-west oriented antenna. The observed correlation hints that with kHz antennas the direction of lightning strikes can be reconstructed. This is only possible since the kHz antennas deployed at LOPES have a gain pattern that is only sensitive in the forward direction. Therefore the signal height in this antenna is correlated with the projection of the signal in the corresponding direction.

A.8. Further Investigations with KASCADE

To check the influence of extreme weather conditions on air shower parameters the electron muon ratio of the air showers measured with KASCADE was investigated. For this analysis several different weather categories were analysed to have a very detailed view which condition has which effect on the ratio. During a thunderstorm there are not only strong electric fields but also differences in the pressure and the temperature. These different aspects were analysed separately. The data samples for the weather periods have been chosen carefully. The influence was estimated to be linearly correlated. After disentangling the different weather conditions and their influence on the electron muon ratio according to table A.1 the correction factors for the different conditions were calculated and applied on the thunderstorm data. Even with this correction the fraction of the two ratios (i.e. $\frac{\left(\frac{lg(N_\mu)}{lg(N_e)}\right)_a}{\left(\frac{lg(N_\mu)}{lg(N_\mu)}\right)_b}$ with a representing the fair weather data and b the exceptional weather data) is significantly different from the expectations which hints to a mutual non-linear interaction between the different weather phenomena.

Table A.1.: Electron muon ratio for different conditions

Category	difference from expectation $[10^{-3}]$
rain vs. fair weather	4.24 ± 0.32
random samples vs. fair weather	0.023 ± 0.165
low- vs. normal pressure	6.29 ± 0.17
high- vs. low temperature	6.46 ± 0.17
rain corrected $\cup$ pressure corrected $\cup$ temperature corrected vs. fair weather	1.53 ± 0.32
random samples corrected vs. fair weather	0.024 ± 0.165
thunderstorm vs. fair weather	6.71 ± 2.85
thunderstorm corrected for rain-, pressure- and temperature dependence vs. fair weather	4.45 ± 2.85

A.9. Investigations at the Pierre Auger Observatory

Among different possible techniques, radio observations with dedicated antenna arrays are most suitable to follow the lightning development in time and space with highest resolution. Such lightning mapping arrays (LMA) (Rison, W., Thomas, R.J., Krehbiel, P.R., Hamlin, T., Harlin, J., 1999) are devices especially designed to better measure the initiation and generation of lightning and can be used - when co-located to air shower experiments - to investigate the influence of thunderstorms and lightning on the air shower detection by particle detectors. In this sense the "Lightning Air Shower Study" project LASS as a part of the Pierre Auger Observatory (Abraham J. et al., 2004) is the next generation experiment for lightning and thunderstorm investigations in combination with an air shower experiment. LASS will help to better understand the development of lightning as well as to investigate the influence of thunderstorms and lightning to the air shower detection by particle detectors, by fluorescence telescopes, and by radio antenna arrays such as LOPES or AERA, where AERA will be combined with the lightning mapping array.

By deploying different types of radio antennas and highly sensitive electric field mills a lightning can be observed with a spatial resolution of around 10 m and time resolution of about 40 ns (Thomas, R.J., Krehbiel, P.R., Rison, W., Hunyady, S.J., Winn, W.P., Hamli, T., Harlin, J., 2004). Data from the LMA stations can then be combined to provide three-dimensional images of the lightning channels, including lightning initiation positions and times of occurrence. Each LMA station records peak signal magnitude and time in every $80\,\mu$s interval in a quiet 6 MHz VHF band at typically 63 MHz.

The goals of such a project are the determination of a possible correlation between lightning and cosmic-ray air showers, to study the effects of strong electric fields on the radio emission of EAS, to study the influence of strong electric fields or thunderstorms on the particle component of EAS and to investigate whether distant lightnings harm the performance of the fluorescence detectors. For that purposes the installation within an existing EAS experiment, such as the Pierre Auger Observatory, is ideal. Both projects could profit from each other as lightning can also affect the air shower measurements by producing a broadband light flash that can harm fluorescence measurements over long distances. The X- and gamma rays produced by lightning strikes can irradiate the particle detectors and cause background. The moving charge in a lightning causes also emission in the MHz range which causes additional radio background. The strong atmospheric electric fields during thunderstorms can seriously influence the distributions of charged particles from an EAS in the atmosphere, which strongly affects the correct reconstruction of this air shower.

A.10. Conclusion

The radio detection technique has a high reliability in all but the most extreme weather conditions, as for example the reconstructed energy of an air shower is influenced by electric fields during thunderstorms, but not at normal weather conditions. This leads to a larger fraction of events with a detected coherent signal during thunderstorms. Consequently it is mandatory for antenna air-shower arrays to monitor the electric field of the atmosphere. LOPES was built within the existing cosmic-ray air shower experiment KASCADE-Grande. This allowed first low-level studies of correlations between cosmic rays and lightning strikes, by analysing the air-shower properties given by KASCADE-Grande and the geometry of the lightning strike observed with LOPES. These first analyses showed no significant correlation between cosmic rays and lightning strikes. Furthermore the influence of different weather conditions on the electron muon ratio of the air showers measured with KASCADE was investigated and hints for a mutual non-linear interaction between the different weather phenomena were found.

APPENDIX B

LOPES 3D calibration values

Table B.1.: Measured LOPES 3D calibration values.

antenna ID	northing [m]	easting [m]	diff. height[m]	polarization	station number	diff. delay [s]
10101	112.661	-64.153	-0.407	EW	1	0
10102	112.661	-64.153	-0.407	NS	1	2.241e-09
10201	55.804	-52.726	-0.335	EW	2	-4.17124e-07
10202	55.804	-52.726	-0.335	NS	2	-4.1532e-07
20101	-1.161	-40.853	-0.424	EW	4	-4.56464e-07
20102	3.451	41.535	-0.386	EW	3	-4.58752e-07
20201	3.451	41.535	-0.386	NS	3	-4.18035e-07
20202	3.3735	41.577	-0.303	VE	3	-4.18085e-07
30101	55.7265	-52.684	-0.252	VE	2	4.28688e-07
30102	112.584	-64.111	-0.324	VE	1	1.1299e-08
40101	-62.454	-111.186	0	EW	8	1.20428e-06
40102	-62.454	-111.186	0	NS	8	1.20519e-06
40201	-89.797	-10.449	-0.118	EW	9	1.19902e-06
40202	-62.5315	-111.144	0.083	VE	8	1.20375e-06
50101	-89.797	-10.449	-0.118	NS	9	1.20741e-06
50102	-110.688	64.425	0.107	EW	10	7.8912e-07
50201	-110.688	64.425	0.107	NS	10	7.85101e-07
50202	-110.766	64.467	0.19	VE	10	7.85561e-07
60101	-1.161	-40.853	-0.424	NS	4	1.20334e-06
60102	-89.8745	-10.407	-0.035	VE	9	1.20606e-06
70101	-13.081	-97.787	-0.119	EW	5	9.53602e-07
70102	-33.25	-22.987	-0.361	EW	6	9.52025e-07
70201	-33.25	-22.987	-0.361	NS	6	9.61199e-07
70202	-60.805	78.402	0.042	EW	7	5.61373e-07
80101	-60.805	78.402	0.042	NS	7	5.29173e-07
80102	-60.8825	78.444	0.125	VE	7	5.38034e-07
80201	-13.1585	-97.745	-0.036	NS	5	9.64152e-07
80202	-33.3275	-22.945	-0.278	VE	6	9.52537e-07
90101	-13.081	-97.787	-0.119	VE	5	5.42332e-07
90102	-1.2385	-40.811	-0.341	VE	4	9.58461e-07

APPENDIX C

Weighting factors for the gain-method

Table C.1.: Weighting factors for the gain-method.

ze / az	0-5	5-10	10-15	15-20	20-25	25-30	30-35	35-40	40-45	45-50	50-55	55-60	60-65	65-70	70-75	75-80	80-85	85-90
0-10	0.33	0.33	0.35	0.38	0.36	0.36	0.36	0.38	0.39	0.4	0.42	0.43	0.44	0.46	0.48	0.52	0.57	0.65
	0.33	0.26	0.23	0.2	0.2	0.21	0.23	0.24	0.25	0.25	0.26	0.26	0.26	0.26	0.25	0.24	0.21	0.17
	0.33	0.41	0.42	0.42	0.43	0.43	0.41	0.39	0.36	0.34	0.33	0.31	0.29	0.28	0.26	0.24	0.22	0.17
10-20	0.33	0.34	0.36	0.4	0.39	0.37	0.37	0.38	0.39	0.4	0.42	0.43	0.44	0.46	0.48	0.52	0.57	0.65
	0.33	0.26	0.24	0.21	0.22	0.23	0.23	0.24	0.25	0.26	0.26	0.26	0.26	0.26	0.25	0.24	0.21	0.17
	0.33	0.4	0.4	0.38	0.4	0.4	0.39	0.38	0.36	0.34	0.32	0.31	0.29	0.28	0.26	0.24	0.22	0.17
20-30	0.33	0.35	0.38	0.42	0.41	0.39	0.39	0.39	0.4	0.41	0.42	0.43	0.44	0.46	0.49	0.52	0.57	0.65
	0.33	0.28	0.26	0.23	0.24	0.24	0.25	0.25	0.26	0.26	0.27	0.27	0.27	0.26	0.25	0.24	0.21	0.17
	0.33	0.37	0.36	0.34	0.35	0.36	0.36	0.35	0.34	0.33	0.32	0.3	0.29	0.28	0.26	0.24	0.22	0.17
30-40	0.33	0.36	0.39	0.44	0.43	0.41	0.4	0.4	0.41	0.41	0.42	0.43	0.44	0.46	0.49	0.52	0.57	0.65
	0.33	0.29	0.28	0.25	0.25	0.26	0.27	0.27	0.27	0.27	0.27	0.27	0.27	0.26	0.25	0.24	0.21	0.17
	0.33	0.35	0.34	0.31	0.32	0.33	0.33	0.33	0.32	0.31	0.31	0.3	0.29	0.27	0.26	0.24	0.22	0.17
40-50	0.33	0.36	0.39	0.44	0.44	0.41	0.41	0.41	0.41	0.41	0.42	0.43	0.44	0.46	0.49	0.52	0.57	0.65
	0.33	0.31	0.29	0.27	0.27	0.28	0.29	0.29	0.29	0.29	0.28	0.28	0.27	0.27	0.26	0.24	0.21	0.17
	0.33	0.33	0.31	0.29	0.29	0.3	0.31	0.31	0.3	0.3	0.29	0.29	0.28	0.27	0.26	0.24	0.22	0.17
50-60	0.33	0.36	0.39	0.44	0.44	0.41	0.41	0.41	0.41	0.41	0.42	0.43	0.44	0.46	0.49	0.52	0.57	0.65
	0.33	0.33	0.31	0.29	0.29	0.3	0.31	0.31	0.3	0.3	0.29	0.29	0.28	0.27	0.26	0.24	0.21	0.17
	0.33	0.31	0.29	0.27	0.27	0.28	0.29	0.29	0.29	0.29	0.28	0.28	0.28	0.27	0.26	0.24	0.21	0.17
60-70	0.33	0.36	0.39	0.44	0.43	0.41	0.4	0.4	0.41	0.41	0.42	0.43	0.44	0.46	0.49	0.52	0.57	0.65
	0.33	0.35	0.34	0.31	0.32	0.33	0.33	0.33	0.32	0.31	0.31	0.3	0.29	0.27	0.26	0.24	0.22	0.17
	0.33	0.29	0.28	0.25	0.25	0.26	0.27	0.27	0.27	0.27	0.27	0.27	0.27	0.26	0.25	0.24	0.21	0.17
70-80	0.33	0.35	0.38	0.43	0.41	0.39	0.39	0.39	0.4	0.41	0.42	0.43	0.44	0.46	0.49	0.52	0.57	0.65
	0.33	0.37	0.36	0.34	0.35	0.36	0.36	0.35	0.34	0.33	0.32	0.3	0.29	0.28	0.26	0.24	0.22	0.17
	0.33	0.28	0.26	0.23	0.24	0.24	0.25	0.25	0.26	0.26	0.27	0.27	0.27	0.26	0.25	0.24	0.21	0.17
80-90	0.33	0.34	0.36	0.41	0.39	0.37	0.37	0.38	0.39	0.4	0.42	0.43	0.44	0.46	0.49	0.52	0.57	0.65
	0.33	0.39	0.4	0.38	0.4	0.4	0.39	0.38	0.36	0.34	0.32	0.31	0.29	0.28	0.26	0.24	0.22	0.17
	0.33	0.26	0.24	0.21	0.22	0.23	0.23	0.24	0.25	0.26	0.26	0.26	0.26	0.26	0.25	0.24	0.21	0.17
90-100	0.33	0.34	0.35	0.39	0.36	0.36	0.36	0.38	0.39	0.4	0.42	0.43	0.44	0.46	0.49	0.52	0.57	0.65
	0.33	0.41	0.42	0.41	0.43	0.43	0.41	0.39	0.36	0.34	0.33	0.31	0.29	0.28	0.26	0.24	0.22	0.17
	0.33	0.26	0.23	0.2	0.2	0.22	0.23	0.24	0.25	0.25	0.26	0.26	0.26	0.26	0.25	0.24	0.21	0.17
100-110	0.33	0.34	0.37	0.41	0.38	0.37	0.37	0.38	0.39	0.4	0.42	0.43	0.44	0.46	0.49	0.52	0.57	0.65
	0.33	0.39	0.4	0.38	0.4	0.4	0.39	0.38	0.36	0.34	0.32	0.31	0.29	0.28	0.26	0.24	0.22	0.17
	0.33	0.26	0.24	0.21	0.22	0.23	0.23	0.24	0.25	0.25	0.26	0.26	0.26	0.26	0.25	0.24	0.21	0.17
110-120	0.33	0.36	0.39	0.43	0.4	0.39	0.39	0.39	0.4	0.41	0.42	0.43	0.44	0.46	0.49	0.52	0.57	0.65
	0.33	0.37	0.36	0.34	0.36	0.37	0.36	0.36	0.34	0.33	0.32	0.3	0.29	0.28	0.26	0.24	0.22	0.17
	0.33	0.28	0.26	0.23	0.24	0.24	0.25	0.25	0.26	0.26	0.26	0.26	0.26	0.26	0.25	0.24	0.21	0.17
120-130	0.33	0.37	0.4	0.44	0.42	0.4	0.4	0.4	0.41	0.41	0.42	0.43	0.45	0.46	0.49	0.52	0.57	0.65
	0.33	0.34	0.33	0.31	0.33	0.33	0.34	0.33	0.33	0.32	0.31	0.3	0.29	0.27	0.26	0.24	0.22	0.17

ze / az	0-5	5-10	10-15	15-20	20-25	25-30	30-35	35-40	40-45	45-50	50-55	55-60	60-65	65-70	70-75	75-80	80-85	85-90
	0.33	0.29	0.27	0.25	0.26	0.26	0.26	0.27	0.27	0.27	0.27	0.27	0.27	0.26	0.25	0.24	0.21	0.17
	0.33	0.37	0.41	0.44	0.42	0.41	0.41	0.41	0.41	0.42	0.42	0.43	0.45	0.46	0.49	0.52	0.57	0.65
130-140	0.33	0.32	0.3	0.29	0.3	0.31	0.31	0.31	0.31	0.3	0.3	0.29	0.28	0.27	0.26	0.24	0.21	0.17
	0.33	0.31	0.29	0.27	0.28	0.28	0.28	0.28	0.28	0.28	0.28	0.28	0.27	0.27	0.26	0.24	0.21	0.17
	0.33	0.37	0.41	0.44	0.42	0.41	0.41	0.41	0.41	0.42	0.43	0.44	0.45	0.46	0.49	0.52	0.57	0.65
140-150	0.33	0.29	0.28	0.27	0.28	0.29	0.29	0.29	0.29	0.29	0.29	0.28	0.28	0.27	0.26	0.24	0.21	0.17
	0.33	0.33	0.31	0.29	0.3	0.3	0.3	0.3	0.3	0.29	0.29	0.28	0.28	0.27	0.26	0.24	0.21	0.17
	0.33	0.37	0.41	0.43	0.41	0.41	0.4	0.41	0.41	0.42	0.43	0.44	0.45	0.46	0.49	0.52	0.57	0.65
150-160	0.33	0.27	0.26	0.25	0.26	0.27	0.27	0.28	0.28	0.28	0.28	0.28	0.27	0.27	0.26	0.24	0.21	0.17
	0.33	0.35	0.33	0.32	0.32	0.32	0.32	0.32	0.31	0.3	0.3	0.29	0.28	0.27	0.26	0.24	0.21	0.17
	0.33	0.36	0.4	0.41	0.4	0.4	0.4	0.4	0.41	0.42	0.43	0.44	0.45	0.46	0.49	0.52	0.57	0.65
160-170	0.33	0.26	0.24	0.24	0.25	0.25	0.26	0.26	0.27	0.27	0.27	0.27	0.27	0.26	0.25	0.24	0.21	0.17
	0.33	0.38	0.36	0.35	0.35	0.35	0.34	0.33	0.32	0.31	0.3	0.29	0.28	0.27	0.26	0.24	0.22	0.17
	0.33	0.35	0.39	0.39	0.39	0.39	0.39	0.4	0.41	0.42	0.43	0.44	0.45	0.46	0.49	0.52	0.57	0.65
170-180	0.33	0.24	0.22	0.22	0.23	0.24	0.25	0.26	0.26	0.26	0.27	0.27	0.27	0.26	0.25	0.24	0.21	0.17
	0.33	0.41	0.39	0.38	0.38	0.37	0.36	0.35	0.33	0.32	0.31	0.3	0.29	0.27	0.26	0.24	0.22	0.17
	0.33	0.34	0.38	0.38	0.38	0.38	0.39	0.4	0.41	0.42	0.42	0.44	0.45	0.46	0.49	0.52	0.57	0.65
180-190	0.33	0.23	0.21	0.22	0.23	0.24	0.25	0.25	0.26	0.26	0.27	0.27	0.27	0.26	0.25	0.24	0.21	0.17
	0.33	0.43	0.4	0.4	0.39	0.38	0.37	0.35	0.34	0.32	0.31	0.3	0.29	0.27	0.26	0.24	0.22	0.17
	0.33	0.35	0.39	0.39	0.39	0.39	0.39	0.4	0.41	0.42	0.43	0.44	0.45	0.46	0.49	0.52	0.57	0.65
190-200	0.33	0.24	0.22	0.23	0.23	0.24	0.25	0.26	0.26	0.26	0.27	0.27	0.27	0.26	0.25	0.24	0.21	0.17
	0.33	0.4	0.38	0.38	0.38	0.37	0.36	0.35	0.33	0.32	0.31	0.3	0.29	0.27	0.26	0.24	0.22	0.17
	0.33	0.37	0.41	0.41	0.4	0.4	0.4	0.4	0.41	0.42	0.43	0.44	0.45	0.46	0.49	0.52	0.57	0.65
200-210	0.33	0.26	0.24	0.24	0.25	0.25	0.26	0.26	0.27	0.27	0.27	0.27	0.27	0.26	0.25	0.24	0.21	0.17
	0.33	0.37	0.35	0.35	0.35	0.35	0.34	0.33	0.32	0.31	0.3	0.29	0.28	0.27	0.26	0.24	0.22	0.17
	0.33	0.38	0.42	0.42	0.41	0.41	0.41	0.41	0.41	0.42	0.43	0.44	0.45	0.46	0.49	0.52	0.57	0.65
210-220	0.33	0.27	0.26	0.26	0.26	0.27	0.27	0.27	0.27	0.28	0.27	0.27	0.27	0.27	0.26	0.24	0.21	0.17
	0.33	0.34	0.32	0.32	0.33	0.33	0.32	0.32	0.31	0.3	0.3	0.29	0.28	0.27	0.26	0.24	0.22	0.17
	0.33	0.39	0.42	0.42	0.42	0.41	0.41	0.41	0.42	0.42	0.43	0.44	0.45	0.46	0.49	0.52	0.57	0.65
220-230	0.33	0.29	0.28	0.28	0.28	0.29	0.29	0.29	0.29	0.28	0.28	0.28	0.27	0.27	0.26	0.24	0.21	0.17
	0.33	0.32	0.3	0.3	0.3	0.3	0.3	0.3	0.3	0.29	0.29	0.28	0.28	0.27	0.26	0.24	0.22	0.17
	0.33	0.39	0.42	0.42	0.42	0.41	0.41	0.41	0.42	0.42	0.43	0.44	0.45	0.46	0.49	0.52	0.57	0.65
230-240	0.33	0.32	0.3	0.3	0.3	0.3	0.3	0.3	0.3	0.29	0.29	0.28	0.28	0.27	0.26	0.24	0.21	0.17
	0.33	0.29	0.28	0.28	0.28	0.29	0.29	0.29	0.29	0.28	0.28	0.28	0.27	0.27	0.26	0.24	0.21	0.17
	0.33	0.38	0.42	0.42	0.41	0.41	0.41	0.41	0.41	0.42	0.43	0.44	0.45	0.46	0.49	0.52	0.57	0.65
240-250	0.33	0.34	0.32	0.32	0.33	0.33	0.32	0.32	0.31	0.3	0.3	0.29	0.28	0.27	0.26	0.24	0.22	0.17
	0.33	0.27	0.26	0.26	0.26	0.27	0.27	0.27	0.27	0.28	0.27	0.27	0.27	0.27	0.26	0.24	0.21	0.17
	0.33	0.37	0.41	0.41	0.4	0.4	0.4	0.4	0.41	0.42	0.43	0.44	0.45	0.46	0.49	0.52	0.57	0.65
250-260	0.33	0.37	0.35	0.35	0.35	0.35	0.34	0.33	0.32	0.31	0.3	0.29	0.28	0.27	0.26	0.24	0.22	0.17
	0.33	0.26	0.24	0.24	0.25	0.25	0.26	0.26	0.27	0.27	0.27	0.27	0.27	0.26	0.25	0.24	0.21	0.17
	0.33	0.35	0.39	0.39	0.39	0.39	0.39	0.4	0.41	0.42	0.43	0.44	0.45	0.46	0.49	0.52	0.57	0.65
260-270																		

ze / az	0-5	5-10	10-15	15-20	20-25	25-30	30-35	35-40	40-45	45-50	50-55	55-60	60-65	65-70	70-75	75-80	80-85	85-90
	0.33	0.41	0.38	0.38	0.38	0.37	0.36	0.35	0.33	0.32	0.31	0.3	0.29	0.27	0.26	0.24	0.22	0.17
	0.33	0.24	0.22	0.23	0.23	0.24	0.25	0.26	0.26	0.26	0.27	0.27	0.27	0.26	0.25	0.24	0.21	0.17
	0.33	0.34	0.38	0.38	0.38	0.38	0.39	0.4	0.41	0.41	0.42	0.44	0.45	0.46	0.49	0.52	0.57	0.65
270-280	0.33	0.43	0.4	0.4	0.39	0.38	0.37	0.35	0.34	0.32	0.31	0.3	0.29	0.27	0.26	0.24	0.22	0.17
	0.33	0.23	0.21	0.22	0.23	0.24	0.25	0.25	0.26	0.26	0.27	0.27	0.27	0.26	0.25	0.24	0.21	0.17
	0.33	0.35	0.39	0.39	0.39	0.39	0.39	0.4	0.41	0.42	0.42	0.43	0.45	0.46	0.49	0.52	0.57	0.65
280-290	0.33	0.41	0.39	0.38	0.38	0.37	0.36	0.35	0.33	0.32	0.31	0.3	0.29	0.27	0.26	0.24	0.22	0.17
	0.33	0.24	0.22	0.22	0.23	0.24	0.25	0.26	0.26	0.27	0.27	0.27	0.27	0.26	0.25	0.24	0.21	0.17
	0.33	0.36	0.4	0.41	0.4	0.4	0.4	0.4	0.41	0.42	0.43	0.44	0.45	0.46	0.49	0.52	0.57	0.65
290-300	0.33	0.38	0.36	0.35	0.35	0.35	0.34	0.33	0.32	0.31	0.3	0.29	0.28	0.27	0.26	0.24	0.22	0.17
	0.33	0.26	0.24	0.24	0.25	0.25	0.26	0.26	0.27	0.27	0.27	0.27	0.27	0.27	0.26	0.24	0.21	0.17
	0.33	0.37	0.41	0.43	0.42	0.41	0.4	0.41	0.41	0.42	0.43	0.44	0.45	0.46	0.49	0.52	0.57	0.65
300-310	0.33	0.36	0.33	0.32	0.32	0.32	0.32	0.32	0.31	0.3	0.3	0.29	0.28	0.27	0.26	0.24	0.22	0.17
	0.33	0.28	0.26	0.25	0.26	0.27	0.27	0.28	0.28	0.28	0.28	0.28	0.27	0.27	0.26	0.24	0.22	0.17
	0.33	0.37	0.41	0.44	0.42	0.41	0.41	0.41	0.41	0.42	0.43	0.43	0.45	0.46	0.49	0.52	0.57	0.65
310-320	0.33	0.33	0.31	0.29	0.3	0.3	0.3	0.3	0.3	0.29	0.29	0.28	0.28	0.27	0.26	0.24	0.22	0.17
	0.33	0.29	0.28	0.27	0.28	0.29	0.29	0.29	0.29	0.29	0.29	0.28	0.28	0.27	0.26	0.24	0.22	0.17
	0.33	0.37	0.41	0.45	0.42	0.41	0.41	0.41	0.41	0.42	0.42	0.43	0.45	0.46	0.49	0.52	0.57	0.65
320-330	0.33	0.31	0.29	0.27	0.28	0.28	0.28	0.28	0.28	0.28	0.28	0.28	0.27	0.27	0.26	0.24	0.21	0.17
	0.33	0.32	0.3	0.29	0.3	0.31	0.31	0.31	0.31	0.3	0.3	0.29	0.28	0.27	0.26	0.24	0.22	0.17
	0.33	0.37	0.4	0.45	0.42	0.4	0.4	0.4	0.41	0.41	0.42	0.43	0.44	0.46	0.48	0.52	0.57	0.65
330-340	0.33	0.29	0.27	0.25	0.26	0.26	0.26	0.27	0.27	0.27	0.27	0.27	0.27	0.26	0.25	0.24	0.21	0.17
	0.33	0.34	0.33	0.31	0.33	0.33	0.34	0.33	0.33	0.32	0.31	0.3	0.29	0.28	0.26	0.24	0.22	0.17
	0.33	0.36	0.38	0.44	0.41	0.39	0.39	0.39	0.4	0.41	0.42	0.43	0.44	0.46	0.48	0.52	0.57	0.65
340-350	0.33	0.28	0.26	0.23	0.24	0.24	0.25	0.25	0.26	0.26	0.26	0.26	0.26	0.26	0.25	0.24	0.21	0.17
	0.33	0.37	0.36	0.34	0.36	0.37	0.36	0.36	0.34	0.33	0.32	0.3	0.29	0.28	0.26	0.24	0.22	0.17
	0.33	0.34	0.36	0.41	0.38	0.37	0.37	0.38	0.39	0.4	0.42	0.43	0.44	0.46	0.48	0.52	0.57	0.65
350-360	0.33	0.26	0.24	0.21	0.22	0.23	0.23	0.24	0.25	0.25	0.26	0.26	0.26	0.26	0.25	0.24	0.21	0.17
	0.33	0.39	0.4	0.38	0.4	0.4	0.39	0.38	0.36	0.34	0.32	0.31	0.29	0.28	0.26	0.24	0.22	0.17

APPENDIX D

Angular Deviation Between the LOPES 3D and the KASCADE-Grande Direction Reconstruction

In figures D.1 and D.2 the angular difference between the shower arrival direction reconstructed with LOPES 3D and the direction reconstructed with KASCADE-Grande are shown exemplary for two weighting schemes. The mean values for all weighting schemes can be found in table D.1.

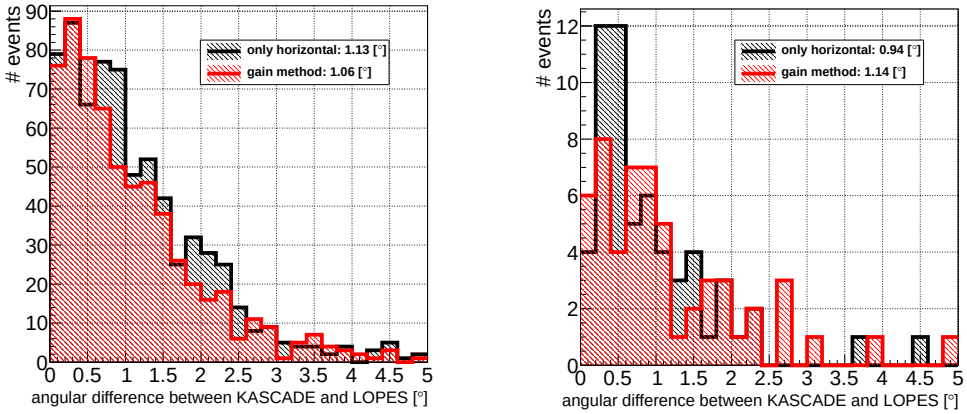

(a) (b)

Figure D.1.: Angular difference between the KASCADE-Grande and LOPES reconstructed air shower arrival direction for two different weightings of the reconstruction of the electric field vector for classic (left) and vectorial (right) beamforming for zenith angles $\theta \leq 45°$.

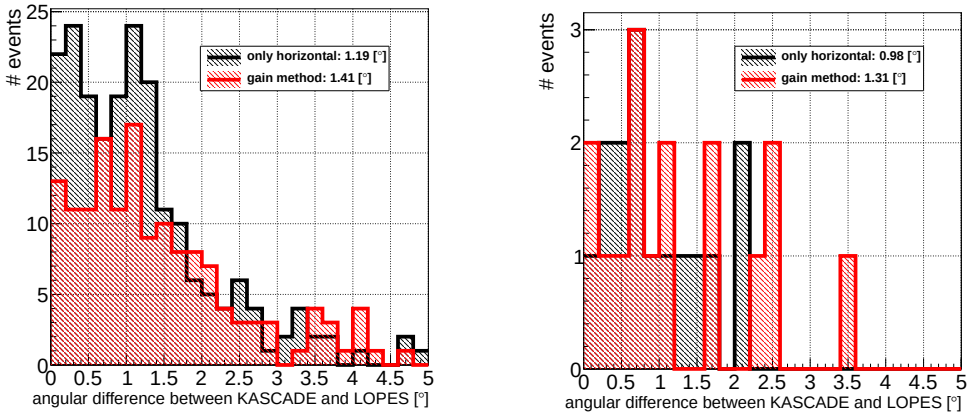

(a) (b)

Figure D.2.: Angular difference between the KASCADE-Grande and LOPES reconstructed air shower arrival direction for two different weightings of the reconstruction of the electric field vector for classic (left) and vectorial (right) beamforming for zenith angles $\theta \geq 45°$.

Table D.1.: Deviation between the LOPES 3D and the KASCADE-Grande direction reconstruction (mean values).

weighting scheme / dataset	only horizontal	equal weighting	gain method	vxB method	active antenna height
Grande-normal classic beamforming	1.13°	1.09°	1.07°	1.16°	1.52°
Grande-normal vectorial beamforming	0.94°	1.08°	1.14°	1.02°	1.18°
Grande-inclined classic beamforming	1.19°	1.55°	1.41°	1.42°	1.22°
Grande-inclined vectorial beamforming	0.99°	1.40°	1.31°	1.00°	1.37°

Bibliography

Aab, A. et al. (Pierre Auger Collaboration) (2014). *Probing the radio emission from air showers with polarization measurements*. Phys. Rev. D, 89: 052002. doi:10.1103/PhysRevD.89.052002.

Abraham, J. et al. (Pierre Auger Collaboration) (2010). *Measurement of the Depth of Maximum of Extensive Air Showers above* 10^{18} eV. Phys. Rev. Lett., 104 (9): 091101. doi:10.1103/PhysRevLett.104.091101.

Abraham J. et al. (Pierre Auger Collaboration) (2004). *Properties and performance of the prototype instrument for the Pierre Auger Observatory*. Nuclear Instruments and Methods in Physics Research A, 523 (1-2): 50 – 95. doi: DOI:10.1016/j.nima.2003.12.012.

Abraham J. et al. (Pierre Auger Collaboration) (2010). *The fluorescence detector of the Pierre Auger Observatory*. Nuclear Instruments and Methods in Physics Research A, 620 (2-3): 227 – 251. doi:DOI:10.1016/j.nima.2010.04.023.

Abreu, P. et al. (Pierre Auger Collaboration) (2012). *Antennas for the detection of radio emission pulses from cosmic-ray induced air showers at the Pierre Auger Observatory*. Journal of Instrumentation, 7 (10): P10011. URL http://stacks.iop.org/1748-0221/7/i=10/a=P10011.

Ackermann, M. et al. (2013). *Detection of the characteristic pion-decay signature in supernova remnants*. 339 (6121): 807–811. doi:10.1126/science.1231160.

Aglietta, M. et al. (1989). *The EAS-TOP array at* $E_0 = 10^{14}$ - 10^{16} *eV : stability and resolutions*. Nucl. Instr. Meth. A, A277: 23–28.

Aharonian, F. and Akerlof, C. (1997). *Gamma-ray astronomy with imaging atmospheric Cerenkov telescopes*. ANNUAL REVIEW OF NUCLEAR AND PARTICLE SCIENCE, 47: 273–314. doi:10.1146/annurev.nucl.47.1.273.

Allan, H. R. (1971). *Radio Emission From Extensive Air Showers*. Prog. in Element. part. and Cos. Ray Phys., Vol. 10: 171–302.

Alvarez-Muniz, J. et al. (2013). *The MIDAS telescope for microwave detection of ultra-high energy cosmic rays*. Nuclear Instruments and Methods in Physics Research Section A: Accelerators, Spectrometers, Detectors and Associated Equipment, 719 (0): 70 – 80. doi:http://dx.doi.org/10.1016/j.nima.2013.03.030.

ANKA (2014). *webpage of the ANKA the synchrotron light source facility at the Karlsruhe Institute of Technology (KIT)*. . URL http://www.anka.kit.edu/28.php.

Antoni, T. et al. (KASCADE Collaboration) (2003). *The Cosmic-Ray Experiment KASCADE*. Nucl. Instr. Meth. A, 513 (3): 490–510.

Apel, W. et al. (LOPES Collaboration) (2011a). *Thunderstorm observations by air-shower radio antenna arrays*. Advances in Space Research, 48 (7): 1295 – 1303. doi:http://dx.doi.org/10.1016/j.asr.2011.06.003.

Apel, W. et al. (LOPES Collaboration) (2012a). *LOPES-3D: An antenna array for full signal detection of air-shower radio emission*. Nuclear Instruments and Methods in Physics Research Section A: Accelerators, Spectrometers, Detectors and Associated Equipment, 696 (0): 100 – 109. doi:http://dx.doi.org/10.1016/j.nima.2012.08.082.

Apel, W. D. et al. (KASCADE Collaboration) (2010). *The KASCADE-Grande experiment*. Nucl. Instr. Meth. A, 620: 202–216.

Apel, W. D. et al. (KASCADE-Grande Collaboration) (2011b). *Kneelike structure in the spectrum of the heavy component of cosmic rays observed with KASCADE-Grande*. Phys. Rev. Lett., 107: 171104. doi:10.1103/PhysRevLett.107.171104.

Apel, W. D. et al. (LOPES Collaboration) (2012b). *Experimental evidence for the sensitivity of the air-shower radio signal to the longitudinal shower development*. Phys. Rev. D, 85: 071101. doi:10.1103/PhysRevD.85.071101.

Apel, W. D. et al. (KASCADE-Grande Collaboration) (2013). *Ankle-like feature in the energy spectrum of light elements of cosmic rays observed with KASCADE-Grande*. Phys. Rev. D, 87: 081101. doi:10.1103/PhysRevD.87.081101.

Apel, W. D. et al. (LOPES Collaboration) (submitted 2014a). *Reconstruction of the energy and depth of maximum of cosmic-ray air showers from LOPES radio measurements*. Physical Review D.

Apel, W. D. et al. (LOPES Collaboration) (submitted 2014b). *The wavefront of the radio signal emitted by cosmic ray air showers*.

Apel W. D. et al. (KASCADE Collaboration) (2007). *Test of interaction models up to 40 PeV by studying hadronic cores of EAS*. Journal of Physics G: Nuclear and Particle Physics, 34 (12): 2581. URL http://stacks.iop.org/0954-3899/34/i=12/a=005.

Ardouin, D. et al. (CODALEMA Collaboration) (2009). *Geomagnetic origin of the radio emission from cosmic ray induced air showers observed by CODALEMA*. Astroparticle Physics, 31 (3): 192 – 200. doi:10.1016/j.astropartphys.2009.01.001.

Askaryan, G. A. (1962). *Excess negative charge of an electron-photon shower and its coherent radio emission*. Soviet Physics JETP, 14: 441.

Askaryan, G. A. (1965). *Coherent radio emission from cosmic showers in air and in dense media*. Soviet Physics JETP, 21: 658.

Auger, P. et al. (1939). *Extensive Cosmic-Ray Showers*. Reviews of Modern Physics, 11: 288–291. doi:10.1103/RevModPhys.11.288.

Auger, P. et al. (1939). *Extensive cosmic-ray showers*. Rev. Mod. Phys., 11 (3-4): 288–291. doi:10.1103/RevModPhys.11.288.

Barton, C. E. (1997). *International Geomagnetic Reference Field: the seventh generation*. Journal of Geomagnetism and Geoelectricity, 49: 123–148.

Berezhnev, S. et al. (Tunka Collaboration) (2012). *The Tunka-133 EAS cherenkov light array: Status of 2011*. Nuclear Instruments and Methods in Physics Research Section A: Accelerators, Spectrometers, Detectors and Associated Equipment, 692 (0): 98 – 105. doi:http://dx.doi.org/10.1016/j.nima.2011.12.091. 3rd Roma International Conference on Astroparticle Physics.

bioliq (2014). *webpage of the bioliq facility at the Karlsruhe Institute of Technology (KIT) Campus North*. . URL http://www.bioliq.de/.

Bracewell, R. N. (1986). The Fourier Transform and Its Applications (Second Edition, Revised). McGraw-Hill Book Company. ISBN 0070070156.

Braun, S. (2011). *Gegenseitige Beeinflussung von Luftschauern und Gewittern*. Diploma thesis, Karlsruhe Institute of Technology.

Buitink, S., Huege, T., Falcke, H. and Kuijpers, J. (2010). *Simulation of radio emission from air showers in atmospheric electric fields*. Astroparticle Physics, 33 (5-6): 296 – 306. doi:http://dx.doi.org/10.1016/j.astropartphys.2010.02.010.

Buitink S. et al. (LOPES Collaboration) (2007). *Amplified radio emission from cosmic ray air showers in thunderstorms*. Astronomy & Astrophysics, 467: 385–394. doi:10.1051/0004-6361:20066006.

Buitink, S. et al. (LOFAR Collaboration) (2013). *Shower Xmax determination based on LOFAR radio measurements*. In Proceedings of the 33rd International Cosmic Conference, Rio de Janeiro.

Dwyer, J. R., Uman M. A., and Rassoul H. K. (2009). *Remote measurements of thundercloud electrostatic fields,*. J. Geophys. Res., 114. doi:doi:10.1029/2008JD011386.

Ender, M. et al. (LOPES Collaboration) (2009). *Radio Emission of Extensive Air Showers during Thunderstorms*. In Proceedings of the 31st ICRC, Łódź, Poland, 0405. URL http://icrc2009.uni.lodz.pl/proc/html/.

Engel, R., Heck, D. and Pierog, T. (2011). *Extensive air showers and hadronic interactions at high energy*. Ann.Rev.Nucl.Part.Sci., 61: 467–489. doi:10.1146/annurev.nucl.012809.104544.

Evans, L. and Bryant, P. (2008). *LHC machine*. Journal of Instrumentation, 3 (08): S08001. URL http://stacks.iop.org/1748-0221/3/i=08/a=S08001.

Falcke, H. et al. (2005). *Detection and imaging of atmospheric radio flashes from cosmic ray air showers*. Nature, 435 (7040): 313–316. URL www.scopus.com.

Fermi, E. (1949). *On the Origin of Cosmic Radiation*. Physical Review, 75 (8): 1169.

Fick, D. and Hoffmann, D. (2014). *Werner Kolhörster (1887–1945): The German pioneer of cosmic ray physics* . Astroparticle Physics , 53 (0): 50 – 54. doi:http://dx.doi.org/10.1016/j.astropartphys.2013.09.007. Centenary of cosmic ray discovery, URL http://www.sciencedirect.com/science/article/pii/S0927650513001497.

Fuchs, B. (Pierre Auger Collaboration) (2012a). *The Auger Engineering Radio Array* . Nuclear Instruments and Methods in Physics Research Section A: Accelerators, Spectrometers, Detectors and Associated Equipment, 692 (0): 93 – 97. doi:http://dx.doi.org/10.1016/j.nima.2012.01.058. 3rd Roma International Conference on Astroparticle Physics.

Fuchs, B. L. (2012b). *The lateral distribution of radio signals from cosmic ray air showers*. Phd thesis, Karlsruhe Institute of Technology.

Gaïor, R. e. a. (Pierre Auger Collaboration) (2013). *Detection of cosmic rays using microwave radiation at the Pierre Auger Observatory*. In Proceedings of the 33rd International Cosmic Conference, Rio de Janeiro.

Gaisser, T. K. and Stanev, T. (2006). *High-energy cosmic rays*. Nuclear Physics A, 777: 98–110.

Gelb, M. (2012). *Simluation of Extensive Air Showers and their Radio Emisison in the Prescence of Atmospheric Electric Fields*. Bachelor thesis, Karlsruhe Institute of Technology.

Giller, M. et al. (2005). *Similarity of extensive air showers with respect to the shower age*. Journal of Physics G: Nuclear and Particle Physics, 31 (8): 947. URL http://stacks.iop.org/0954-3899/31/i=8/a=023.

Gorham, P. W. et al. (ANITA Collaboration) (2007). *Observations of the Askaryan effect in ice*. Phys. Rev. Lett., 99: 171101. doi:10.1103/PhysRevLett.99.171101.

Gorham, P. W. et al. (2008). *Observations of microwave continuum emission from air shower plasmas*. Phys. Rev. D, 78: 032007. doi:10.1103/PhysRevD.78.032007. URL http://link.aps.org/doi/10.1103/PhysRevD.78.032007.

Grashorn, E. (2012). *ANITA and the highest energy cosmic rays*. Nuclear Physics B - Proceedings Supplements, 229-232 (0): 553 –. doi:http://dx.doi.org/10.1016/j.nuclphysbps.2012.09.190. Neutrino 2010.

Gress, O. et al. (1999). *The study of primary cosmic rays energy spectrum and mass composition in the energy range 0.5 - 50 pev with TUNKA EAS Cherenkov array*. Nuclear Physics B - Proceedings Supplements, 75 (1-2): 299 – 301. doi:http://dx.doi.org/10.1016/S0920-5632(99)00272-8.

Gurevich, A. and Zybin, K. (2004). *High energy cosmic ray particles and the most powerful new type discharges in thunderstorm atmosphere*. Phys.Lett., A329: 341–347. doi:10.1016/j.physleta.2004.06.094. hep-ex/0403050.

Haungs, A. (2009). *Radio detection of particles from the cosmos*. NIM A, 604: S236–S243.

Haungs, A., Rebel, H. and Roth, M. (2003). *Energy spectrum and mass composition of high-energy cosmic rays*. Reports on Progress in Physics, 66 (7): 1145. URL http://stacks.iop.org/0034-4885/66/i=7/a=202.

Heck, D. et al. (1998). CORSIKA: a Monte Carlo code to simulate extensive air showers.

HESS (2014). *webpage of hess*. URL http://www.mpi-hd.mpg.de/hfm/HESS/.

Hess, V. F. (1912). Z. Phys., 13: 1084.

Holt, E. M. (2013). *Simulationsstudie für ein großskaliges Antennenfeld zur Detektion von Radioemission ausgedehnter Luftschauer* . Diploma thesis, Karlsruhe Institute of Technology.

Horneffer, A. (2006). Measuring Radio Emission from Cosmic Ray Air Showers with a Digital Radio Telescope. Ph.D. thesis, Rheinische Friedrich-Wilhelms-Universität Bonn, Germany. URL http://nbn-resolving.de/urn:nbn:de:hbz:5N-07819.

Horneffer, A., Apel, W. D. and Arteaga, J. C. e. (2008). *Primary Particle Energy Calibration of the EAS Radio Pulse Height*. In International Cosmic Ray Conference, volume 4 of *International Cosmic Ray Conference*, 83–86.

Horneffer, A. et al. (2006). *Radio Detection of Cosmic Rays with LOPES*. In Proc. of the ARENA2005 conference, DESY Zeuthen, Germany, 21S1, 168–181. World Scientific. doi:10.1142/S0217751X0603357X.

Horneffer, A. et al. (2010). *Cosmic ray and neutrino measurements with LOFAR*. Nuclear Instruments and Methods in Physics Research Section A: Accelerators, Spectrometers, Detectors and Associated Equipment, 617 (1–3): 482 – 483. doi:http://dx.doi.org/10.1016/j.nima.2009.10.092.

Huber, D. (2010). *Messung des dreidimensionalen Polarisationsvektors der Radioemission aus Luftschauern*. Diploma thesis, Karlsruhe Institute of Technology.

Huege, T. (2004). Radio Emission from Cosmic Ray Air Showers. Ph.D. thesis, Rheinische Friedrich-Wilhelms-Universität Bonn, Germany. URL http://nbn-resolving.de/urn:nbn:de:hbz:5N-04797.

Huege, T. (2012). *Theory and simulations of air shower radio emission*. In Proceedings of the ARENA 2012 conference, Erlangen, Germany.

Huege, T. and Falcke, H. (2003). *Radio emission from cosmic ray air showers. Coherent geosynchrotron radiation*. Astronomy & Astrophysics, 412: 19–34. doi:10.1051/0004-6361:20031422.

Huege, T. and James, C. (2013). *Full Monte Carlo simulations of radio emission from extensive air showers with CoREAS*. In Proceedings of the 33rd International Cosmic Conference, Rio de Janeiro.

Huege, T., Ludwig, M., Scholten, O. and de Vries, K. D. (2010). *The convergence of EAS radio emission models and a detailed comparison of REAS3 and MGMR simulations*. In Nucl. Instr. and Meth. A; Proceedings of the ARENA 2010 conference, Nantes, France. doi:10.1016/j.nima.2010.11.041.

Huege, T. et al. (LOPES Collaboration) (2012). *The LOPES experiment–recent results, status and perspectives*. Nuclear Instruments and Methods in Physics Research Section A: Accelerators, Spectrometers, Detectors and Associated Equipment, 662, Supplement 1 (0): S72 – S79. doi:http://dx.doi.org/10.1016/j.nima.2010.11.081. 4th International workshop on Acoustic and Radio EeV Neutrino detection Activities.

Huege, T. and Ludwig, M. and James, C.W. (2013). *Simulating radio emission from air showers with CoREAS*.

Huege, T. et. al (Pierre Auger Collaboration) (2010). *Radio detection of cosmic rays in the Pierre Auger Observatory* . Nuclear Instruments and Methods in Physics Research Section A: Accelerators, Spectrometers, Detectors and Associated Equipment, 617 (1 – 3): 484 – 487. doi:http://dx.doi.org/10.1016/j.nima.2009.10.012.

James, C. W., Falcke, H., Huege, T. and Ludwig, M. (2010). *An 'endpoint' formulation for the calculation of electromagnetic radiation from charged particle motion*. Phys Rev. E, submitted. arXiv:1007.4146.

Jelley, J. et al. (1965). *Radio pulses from extensive cosmic-ray air showers*. Nature, 205: 327–328. doi:10.1038/205327a0.

Kahn, F. D. and Lerche, I. (1966). *Radiation from cosmic ray air showers*. In Proc. Roy. Soc., volume A-289, 206.

Kelley, J. e. a. (Pierre Auger Collaboration) (2011). *AERA: the Auger Engineering Radio Array*. In Proceedings of the 32nd International Cosmic Conference, Beijing, V3.

Knurenko, S. et al. (2008). *Recent results from the Yakutsk experiment: The development of EAS and the energy spectrum and primary particle mass composition in the energy region of 1015-1019 eV*. Nuclear Physics B - Proceedings Supplements, 175-176 (0): 201 – 206. doi:http://dx.doi.org/10.1016/j.nuclphysbps.2007.10.035.

Knurenko, S. P. et al. (2010). *32 MHz radio measurements at the Yakutsk EAS array*. In Proceedings of the 22nd ECRS, Turku, Finland, to appear in: Astrophysics and Space Sciences Transactions.

Kölbig, K. and Schorr, B. (1984). *A program package for the landau distribution*. Computer Physics Communications, 31 (1): 97 – 111. doi:http://dx.doi.org/10.1016/0010-4655(84)90085-7.

Lawrence, M. A., Reid, R. J. O. and Watson, A. A. (1991). *The cosmic ray energy spectrum above* $4 * 10^{17}$ *ev as measured by the haverah park array*. Journal of Physics G: Nuclear and Particle Physics, 17 (5): 733. URL http://stacks.iop.org/0954-3899/17/i=5/a=019.

Lehr, J. (2011). *Untersuchung von Sonnenerruptionen mit LOPES und AERA*. Bachelor thesis, Karlsruhe Institute of Technology.

Link, K. (2009). *Messung der Radioemisison kosmischer Strahlung im kHz-Frequenzbereich*. Diploma thesis, Universität Karlsruhe.

Link, K. (2014). Private Communication, Ph.D. thesis in preparation.

Ludwig, M. and Huege, T. (2011). *REAS3: Monte carlo simulations of radio emission from cosmic ray air showers using an end-point formalism*. Astroparticle Physics, 34 (6): 438 – 446. doi:http://dx.doi.org/10.1016/j.astropartphys.2010.10.012.

Luis, P. Facal San (2013). *Status of the program for microwave detection of cosmic rays at the Pierre Auger observatory*. EPJ Web of Conferences, 53: 08009. doi:10.1051/epjconf/20135308009.

MAGIC (2014). *webpage of magic*. URL https://magic.mpp.mpg.de/.

Marin, V. and et al. (CODALEMA Collaboration) (2011). *Charge excess signature in the CODALEMA data. interpretation with selfas2*. In Proceedings of the 32nd International Cosmic Conference, Beijing.

Martineau-Huynh, O. et al. (2012). *First results of the TIANSHAN radio experiment for neutrino detection*. Nuclear Instruments and Methods in Physics Research Section A: Accelerators, Spectrometers, Detectors and Associated Equipment, 662, Supplement 1 (0): S29 – S31. doi:http://dx.doi.org/10.1016/j.nima.2010.11.143. 4th International workshop on Acoustic and Radio EeV Neutrino detection Activities.

Nehls, S. (2008). *Calibrated Measurements of the Radio Emission of Cosmic Ray Air Showers*. FZKA Report 7440, Forschungszentrum Karlsruhe.

Nehls, S. et al. (2008). *Amplitude calibration of a digital radio antenna array for measuring cosmic ray air showers*. Nucl. Instr. Meth., 589: 350–361.

Nichol, R. (2011). *Radio detection of high-energy particles with the ANITA experiment*. Nuclear Instruments and Methods in Physics Research Section A: Accelerators, Spectrometers, Detectors and Associated Equipment, 626–627, Supplement (0): S30 – S35. doi:http://dx.doi.org/10.1016/j.nima.2010.06.268.

Nyquist, H. (1928). *Certain topics in telegraph transmission theory*. American Institute of Electrical Engineers, Transactions of the, 47 (2): 617–644. doi:10.1109/T-AIEE.1928.5055024.

Prescott J. R., H. J. H. and K., P. J. (1971). *Mechanism of radio emission from extensive air showers*. Nature, (41): 109–110. doi:10.1038/physci233109a0.

Rakov, U. M., V. (2005). Lightning: Physics and Effects. Cambridge Univ. Press, isbn 0-521-03541-4 edition.

Ravel, O. et. al (CODALEMA Collaboration) (2012). *The CODALEMA experiment*. Nuclear Instruments and Methods in Physics Research Section A: Accelerators, Spectrometers, Detectors and Associated Equipment, 662, Supplement 1 (0): S89 – S94. doi:http://dx.doi.org/10.1016/j.nima.2010.12.057. 4th International workshop on Acoustic and Radio EeV Neutrino detection Activities.

Rhodes, C. T., Shao X. M., Krehbiel P. R.,Thomas R. J., and Hayenga C. O. (1994). *Observations of lightning phenomena using radio interferometry*. J. Geophys. Res., 99(D6). doi:doi:10.1029/94JD00318.

Rison, W., Thomas, R.J., Krehbiel, P.R., Hamlin, T., Harlin, J. (1999). *A GPS-based three-dimensional lightning mapping system: initial observations in central New Mexico*. Geophys. Res. Lett., 26.

Rothammel, K. (1995). Rothammels Antennenbuch. Franckh-Kosmos, 11 edition.

Ruthroff, C. L. (1959). *Some Broad-Band Transformers*. In Proceedings of the Institute of Radio Engineers, 47.

Scholten, O., de Vries, K. D. and Werner, K. (2010). *Coherent radiation from extensive air showers*. In Nucl. Instr. and Meth. A; Proceedings of the ARENA 2010 conference, Nantes, France. doi:10.1016/j.nima.2010.11.125.

Scholten, O., Werner, K. and Rusydi, F. (2008). *A macroscopic description of coherent geo-magnetic radiation from cosmic-ray air showers*. Astroparticle Physics, 29: 94–103. astro-ph/0709.2872.

Schoorlemmer, H. (2013). Tuning in on comsic rays. Ph.D. thesis, RU Nijmegen.

Schröder, F. G. (2011). Instruments and Methods for the Radio Detection of High Energy Cosmic Rays. Ph.D. thesis. URL http://digbib.ubka.uni-karlsruhe.de/volltexte/1000022313.

Schröder, F. G. et al. (LOPES Collaboration) (2010). *New method for the time calibration of an interferometric radio antenna array*. Nuclear Instruments and Methods in Physics Research Section A: Accelerators, Spectrometers, Detectors and Associated Equipment, 615 (3): 277 – 284. doi:http://dx.doi.org/10.1016/j.nima.2010.01.072.

Sokolsky, P. (2011). *Final results from the high resolution fly's eye (HiRes) experiment*. Nuclear Physics B - Proceedings Supplements, 212-213 (0): 74 – 78. doi:http://dx.doi.org/10.1016/j.nuclphysbps.2011.03.010. Proceedings of the Cosmic Ray International Seminars (CRIS 2010) 100 years of Cosmic Ray Physics: from pioneering experiments to physics in space, URL http://www.sciencedirect.com/science/article/pii/S0920563211000430.

Stanev, T. (2004). High Energy Cosmic Rays. Springer Verlag, 2. edition.

Takeda, M. et al. (1998). *Extension of the cosmic-ray energy spectrum beyond the predicted greisen-zatsepin-kuz'min cutoff*. Phys. Rev. Lett., 81: 1163–1166. doi:10.1103/PhysRevLett.81.1163.

Tanaka, H. et al. (2012). *Studies of the energy spectrum and composition of the primary cosmic rays at 100-1000 tev from the grapes-3 experiment*. Journal of Physics G: Nuclear and Particle Physics, 39 (2): 025201. URL http://stacks.iop.org/0954-3899/39/i=2/a=025201.

Thomas, R.J., Krehbiel, P.R., Rison, W., Hunyady, S.J., Winn, W.P., Hamli, T., Harlin, J. (2004). *Accuracy of the lightning mapping array*. J. Geophys. Res., 109. doi:doi:10.1029/2004/JD004549.

Thoudam, S. et al. (2011). *An air shower array for LOFAR: LORA*. Astrophysics and Space Sciences Transactions, 7 (2): 195–199. doi:10.5194/astra-7-195-2011.

Voors, A. (2005). Handbuch zu 4NEC2, URL http://home.ict.nl/~arivoors/.

Werner, F. (2013). Detection of Microwave Emission of Extensive Air Showers with the CROME Experiment. Ph.D. thesis.

Werner, K. and Scholten, O. (2008). *Macroscopic Treatment of Radio Emission from Cosmic Ray Air Showers based on Shower Simulations*. Astroparticle Physics, 29: 393–411. doi:10.1016/j.astropartphys.2008.04.004.

Acknowledgements
Danksagung

Eine Arbeit wie die hier vorliegende kann natürlich nicht ohne Unterstützung von Dritten angefertigt werden. Es gebührt Vielen mein Dank! Unter anderen möchte ich mich bedanken bei:

- Herrn Prof. Dr. Johannes Blümer für die Übernahme des Referats und die Ermöglichung dieser Arbeit.

- Herrn Prof. Dr. Ulrich Husemann für die Übernahme des Koreferates, die konstante Unterstützung und die sehr hilfreichen regelmässigen Treffen.

- Herrn Dr. Tim Huege für die exzellente Betreuung und Beratung sowie sein Fördern und auch Fordern.

- Herrn Dr. Andreas Haungs für seine einfach immer ständige Bereitschaft mir mit Rat und vor allem Tat zur Seite zu stehen und dafür dass er mir immer Mut machte.

- Der gesamtem Cosmic Ray Gruppe des IK für die Unterstützung die vielen Diskussionen und eine echt geniale und schöne Zeit, die ich nicht missen möchte. Namentlich erwähnen möchte ich Michael K., Michael R., Olga, Qader, Ewa, Roman, Dima, Hauke, Igor, Colin, Julia, Ralph, Ralf, Martin, Max, Joe, Jürgen, Nunzia, Gina, Heike, Kai, Hermann-Josef, Felix, Harald und Andreas in keiner besonderen Reihenfolge. Insbesondere möchte ich Katrin Link für die beinharten (und dadurch sehr hilfreichen) Diskussionen danken. Horia Bozdog für die Hilfe bei allen Kalibrationen und der Kooperation bei der Entwicklung eines neuen Zeitkalibrationsverfahrens. Benjamin "Dr. Ben" Fuchs für die unendlich vielen Kekse und Süßkram jeglicher Art und den meist vergebenen Versuch früh morgens schon meine Laune zu heben. Felix Werner für die ständige Bereitschaft meine Analysen mit mir zu diskutieren sowie seine Expertise nicht nur in Kosmischer Strahlungsphysik, Elektronik und EDV... die er bereitwillig zur Verfügung gestellt hat.

- Der gesamten LOPES Kollaboration, die mir erlaubt hat LOPES neu zu konfigurieren und so meine Arbeit erst möglich gemacht hat. Hierbei möchte ich Frank G. Schröder besonders hervorheben, der mir gezeigt hat, wie man die Verantwortung für ein Experiment übernimmt, der mit seinem immensen Fachwissen stehts zur Verfügung stand und nie müde wurde mir hilfreich zur Seite zu stehen.

- Herrn Dr. Markus Roth für seine Ratschläge auch abseits der Physik und dafür dass er mir die Bellheimer "Witze" (so hoffe ich) nicht krumm genommen hat.

- Herrn (mitlerweile sogar Dipl. Phys. und nichtmer Dipl. Ing. ;-)) Johannes Benedikt Eser aka Skunkinator, für eine echt geniale Zeit in Argentinien, sein lockeres aber dennoch zielstrebiges Wesen, was die Betreuung zumindest meinerseits sehr angenehm machte.

- Sabine Bucher für die exzellente Organisation sowie die unendliche Geduld mit Leuten, die vergessen ihre Dienstreiseanträge zu unterschreiben.

- Der ehemaligen (Anton, Colin, Heizi, Jan, Micheal, Moritz) sowie aktuellen Besatzung (Anne, Kaddl, Goldkehlchen) des "Chuck Norris approved - Parental Advisory" Büros 135. Danke Leute es war eine geile Zeit.

- Sven Schoo dafür, dass er beim Kickern meistens den Kasten sauber gehalten hat und für die angenehme Atmosphähre nicht nur als Zimmergenosse bei Dienstreisen.

- Klaus Bekk Dieter Manger und Doris Wochele für die Unterstützung in IT und vor allem Cluster Fragen.

- Oliver Krömer für die Hilfestellung in Antennen Theorie.

- Nicht zuletzt möchte ich meiner Familie danken, die mich immer unterstützt hat und meine nicht immer leicht zu ertragenden Launen, die die Höhen und Tiefen eines Studiums und einer Promotion mit sich bringen, ertragen hat! Vielen Dank dass ihr mich immer wieder, unphysikalisch gesprochen, "geerdet habt".

- Meinen Jungs und Mädels, die mir privat immer Rückhalt gaben und mir beim Fussball (ob in echt oder auf der Playstation) so manchen blauen Fleck verpasst haben. Von diversen Entspannungswochenenden in der Schwarzwaldresidenz Mühlenloch ganz zu schweigen.

- Meiner Freundin Marianne möchte ich für vieles danken. Im Kontext dieser Arbeit jedoch hauptsächlich für die fortwährende (Fern-)Unterstützung, dass sie nie aufgab mir Mut zu machen und für die physikalischen Diskussionen zu unchristlichen Zeiten.

Abschließend möchte ich mich auch bei allen entschuldigen, die ich in dieser Aufzählung vergessen habe und natürlich möchte ich mich auch bei allen, die diese Arbeit Korrektur gelesen haben, bedanken.

Eidesstattliche Erklärung

Hiermit erkläre ich an Eides statt, dass die vorliegende Dissertation - abgesehen von der Beratung durch meine wissenschaftlichen Betreuer - nach Inhalt und Form meine eigene Arbeit ist. Sie wurde weder ganz noch in Teilen an anderer Stelle im Rahmen eines Prüfungsverfahrens vorgelegt.

Karlsruhe, April 2014

.....
(Daniel Huber)